AD_____

Award Number: W81XWH-06-1-0397

TITLE: Metabolic Mapping of Breast Cancer with Multiphoton Spectral and Lifetime Imaging

PRINCIPAL INVESTIGATOR: Long Yan

CONTRACTING ORGANIZATION: University of Wisconsin-Madison
                                             Madison, WI 53706

REPORT DATE: March 2008

TYPE OF REPORT: Annual Summary

PREPARED FOR: U.S. Army Medical Research and Materiel Command
        Fort Detrick, Maryland 21702-5012

DISTRIBUTION STATEMENT: Approved for Public Release;
                                         Distribution Unlimited

The views, opinions and/or findings contained in this report are those of the author(s) and should not be construed as an official Department of the Army position, policy or decision unless so designated by other documentation.

REPORT DOCUMENTATION PAGE

1. REPORT DATE *(DD-MM-YYYY)* 01-03-2008	2. REPORT TYPE Annual Summary	3. DATES COVERED *(From - To)* 1 MAR 2007 - 28 FEB 2008
4. TITLE AND SUBTITLE Metabolic Mapping of Breast Cancer with Multiphoton Spectral and Lifetime Imaging		**5a. CONTRACT NUMBER**
		5b. GRANT NUMBER W81XWH-06-1-0397
		5c. PROGRAM ELEMENT NUMBER
6. AUTHOR(S) Long Yan E-Mail: longyan@wisc.edu		**5d. PROJECT NUMBER**
		5e. TASK NUMBER
		5f. WORK UNIT NUMBER
7. PERFORMING ORGANIZATION NAME(S) AND ADDRESS(ES) University of Wisconsin-Madison Madison, WI 53706		**8. PERFORMING ORGANIZATION REPORT NUMBER**
9. SPONSORING / MONITORING AGENCY NAME(S) AND ADDRESS(ES) U.S. Army Medical Research and Materiel Command Fort Detrick, Maryland 21702-5012		**10. SPONSOR/MONITOR'S ACRONYM(S)**
		11. SPONSOR/MONITOR'S REPORT NUMBER(S)

12. DISTRIBUTION / AVAILABILITY STATEMENT
Approved for Public Release; Distribution Unlimited

13. SUPPLEMENTARY NOTES

14. ABSTRACT

Tumor cells have altered metabolic states compared to their normal cellular counterparts. We found that fluorescence lifetime imaging of breast carcinoma and breast epithelial cells demonstrated changes in the fluorescent lifetime of bound NADH. Interestingly, there were significant metabolic plasticity differences between carcinoma cells and breast cell lines. In breast epithelial cells (MCF10A) there was a significant decrease in the fluorescence lifetime and percent contribution of protein bound NADH as the cell plating density increased. However, in carcinoma cells (T47D and MDA-MB-231) the lifetime and contribution of protein bound NADH was not responsive to cell plating density. Our findings demonstrate that fluorescence lifetime imaging can be used to differentiate normal and malignant cells and may be useful to help characterize tumor onset and progression on the basis of metabolic state. In order to investigate and verify changes in binding proteins, a polarization anisotropy decay measurements system is under development.

15. SUBJECT TERMS
NADH, Breast Cancer, Metabolism, Lifetime, Spectra, Multiphoton

16. SECURITY CLASSIFICATION OF:			17. LIMITATION OF ABSTRACT	18. NUMBER OF PAGES	19a. NAME OF RESPONSIBLE PERSON USAMRMC
a. REPORT U	**b. ABSTRACT** U	**c. THIS PAGE** U	UU	67	**19b. TELEPHONE NUMBER** *(include area code)*

Table of Contents   Page

INTRODUCTION:

Otto Warburg demonstrated in the first half of the 20th Century that tumor cells have a higher rate of glycolysis than normal cells and this 'Warburg Effect' is the basis for Positron Emission Tomography (PET) analysis of tumors used today in the clinic(1-4). The mechanisms that link tumor progression and metabolic state are still not fully understood, in part because it has been difficult to visualize the dynamics of metabolism *in vivo*. The goal of this project is to investigate the non-invasive imaging techniques of fluorescence lifetime imaging microscopy (FLIM) that has promise of allowing for the monitoring of changes in metabolism between normal and carcinoma cell lines.

We have reported a novel non-invasive method for deriving functional maps of oxidative cellular metabolism *in vivo* via measurement of the fluorescence lifetimes and the ratio of free to protein-bound NADH using two-photon based FLIM (5). We made the interesting observation that there is a progressive decrease in the fluorescence lifetime of both the free and protein-bound components of NADH and an increase in the short lifetime to long lifetime ratio of NADH with increasing confluence.
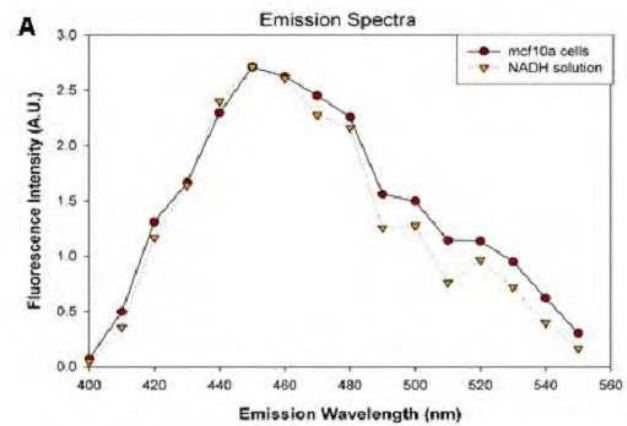
The goal of this study is to extend our previous study of normal cells to breast carcinoma cells to gain insight into metabolic changes in normal and malignant breast cells. We confirmed the endogenous fluorophore identified as NADH via three independent methods. Furthermore, fluorescence lifetime imaging of breast carcinoma and breast epithelial cells at different culture conditions were studied under the same imaging conditions. Fluorescence lifetime analysis results demonstrated changes in the fluorescent lifetime of bound NADH and contribution are different between normal and carcinoma breast cells. Our findings suggest that normal cells maintain metabolic plasticity as growth conditions change, but that carcinoma cells are not

metabolically plastic. Furthermore, our findings demonstrate that fluorescence lifetime imaging microscopy (FLIM) can be used to differentiate normal and malignant cells and may be useful to help characterize tumor onset and progression on the basis of metabolic state. However, additional information is essential to verify and understand the different NADH binding proteins. A system with fluorescence polarization anisotropy decay measurement capability is under development to help achieve this. We expect useful additional information can be obtained by fluorescence polarization anisotropy decay measurement.

BODY:

Endogenous fluorophores provide a potentially powerful resource for obtaining *in situ* information about the metabolic state of cells. However, one critical challenge in using this fluorescence information is to accurately identify the endogenous components that contribute to the signal. In breast cells (MCF10A, T47D and MDA-MB-231) there are three principle fluorophores present – NADH, flavin adenine dinucleotide (FAD) and tryptophan. We concluded that the detected autofluorescence signal under our imaging conditions (excitation at 780 nm) is mainly from NADH based on three lines of evidence (see figure 1): 1) The fluorescence spectrum measured from MCF10A cells matches the spectrum of a pure NADH solution as well as the reported spectral properties of NADH in other reports (6, 7). 2) Further support for the endogenous signal originating from NADH is its co-localization to the mitochondria, an organelle that has high endogenous levels of this dinucleotide. 3) The measured short lifetime decay value ($\tau 1$) we observe in cells is the same as the lifetime decay of free NADH in solution, and is also consistent with other reports, which further supports the finding that the autofluorescence signal is from NADH.

5

figure 1: Emission spectra of NADH dissolved in water (40mM, doted line) or a plate of MCF10A cells at 100,000 cells per plate (solid line). Spectra were collected using the multiphoton FLIM workstation at λ_{EX} = 780 nm with a 16 channel spectral/ lifetime detector and calibrated. Spatial resolution is 10nm per channel. Both the NADH solution and the MCF10A cells had the same emission peak at 450nm, supporting the identity of the endogenous fluorophore in MCF10A cells as NADH under these conditions. (B) NADH localizes in part to mitochondria. Cells were labeled with MitoTracker-Green FM and imaged at λ_{EX} = 780 nm. Endogenous NADH fluorescence (ii) was spectrally resolved from MitoTracker-Green FM (i) by a Low Band-Pass filter (490LP). Overlay image (iii) of NADH (pseudo colored red) and MitoTracker-Green FM (pseudo colored green) demonstrates co-localization of NADH to mitochondria. Scale bar = 10 μm. (C) Table of lifetime results from a solution of pure NADH and a mixed solution of LDH (lactose dehydrogenase) and NADH, which is bound to LDH.

Last year (2007) we worked together with Dr. Roopra, a metabolism expert at the UW-Madison, to design and implement several additional experiments to further validate and characterize the metabolic mapping of NADH results in this study. These included new experiments comparing the fluorescence lifetime of NADH buffer solution with lifetime of NADH in cells, lifetime of NADH solution with addition of LDH (protein which binds NADH), measuring and comparing

the Oxygen consumption among different cell lines under different grows environments, disturbing Glycolysis pathways by adding 2-Deoxy-D-glucose (2DG) into different cell lines under different grows environments and different data analysis methods such as 3 or more components exponential fitting to find the most accurate method for NADH and FAD discrimination. We found that imaging and quantitation of the fluorescence lifetime has the capability of revealing metabolic differences between normal and carcinoma cells, based on the states of bound NADH *in vivo*. (See figure 2) Specifically, normal breast epithelial MCF10A cells showed a significant decrease in the fluorescence lifetime and percent contribution of bound NADH as the cell plating density increased. However, in the carcinoma breast cells T47D and MDA-MB-231, the lifetime and contribution of bound NADH was not responsive to cell plating density. These findings suggest that unlike transformed cells, normal cells are able to affect metabolic adaptation as growth conditions change. Our findings demonstrate that fluorescence lifetime imaging microscopy (FLIM) can be used to distinguish between normal and malignant cells and open up the possibility of using non-invasive multiphoton FLIM monitoring of NADH as a diagnostic tool in cancer detection. Our results were submitted to Journal of Biomedical Optics and the manuscript is under revision (see publication 1).

We summarized the fluorescence lifetime technique into a review paper about non-linear optical imaging in collagen and tumor studies (see publication 2). In addition, with the knowledge of metabolic mapping and fluorescence lifetime we collaborated with other scientists in different research fields. Dr. Provenzano is interested in the relationship between collagen density and breast tumor metabolsim. We collaborated with him last year to look at the role of NADH and collagen density in breast tumor. (see publication 3)
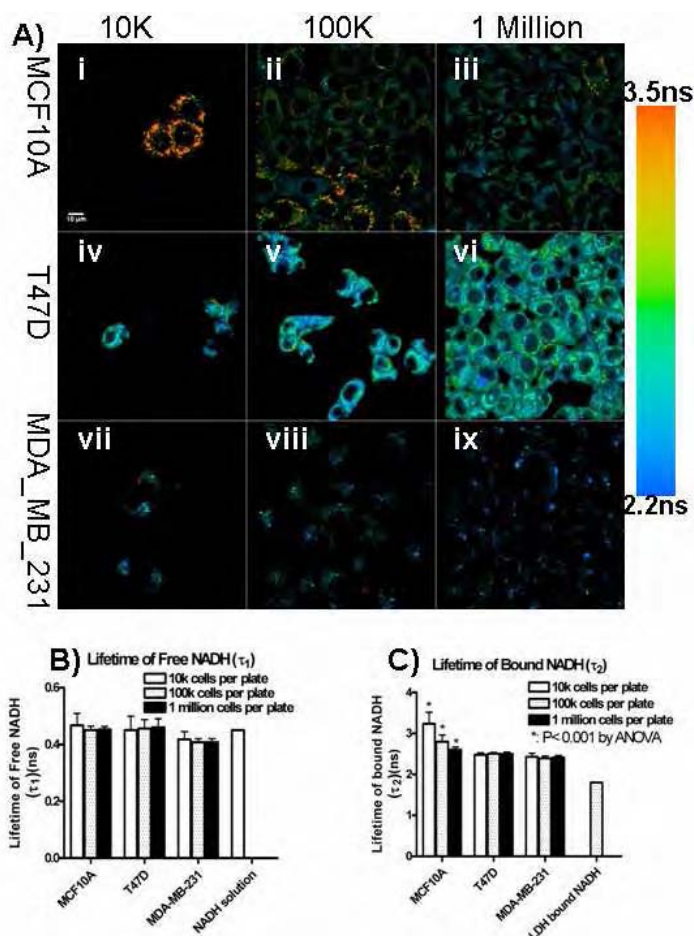
Figure 2: Analysis of the fluorescence lifetime of bound NADH indicates changes in normal, but not in carcinoma cells across increasing cell-plating densities. (A) Color map of the lifetime of bound NADH from representative images for three cell lines: MCF10A (i, ii and iii), T47D(iv, v and vi) and MDA-MB-231(vii, viii and ix) at three plating cell densities: 10K (i, iv and vii), 100K (ii, v and viii) and 1million (iii, vi and ix) cells/ 35mm plate. The color scale is from 2.2ns (blue) to 3.5ns (red). Scale bar is 10 μm.
(B) Chart of the lifetime of free NADH (τ_1) for all the data collected across three cell densities as well as free NADH solution. There is no significant change in the lifetime of free NADH across all three cell lines at the three cell densities. The mean lifetime from cells is 0.45ns, which is same as the lifetime of free NADH in solution.

(C) Chart of the lifetime of bound NADH (τ_2) for all the data collected across three cell densities as well as LDH-bound NADH solution. There is a significant decrease in the lifetime of bound NADH when breast epithelial cells (MCF10A) were plated at densities that increased from 10K cells per plate to 1 million cells per plate (P<0.001 by ANOVA. The number of total samples is 214). However, there is not a significant change in carcinoma cells (T47D and MDA-MB-231) as cell plating density is increased. The lifetime of LDH bound NADH is 1.8ns. (picture is from publication 1).

.KEY RESEARCH ACCOMPLISHMENTS:

- Verified the autofluorescence signal is mainly from NADH by a) comparison of emission spectra with NADH solution under our imaging conditions (Fig 2), b)

- Completed fluorescence lifetime measurement of 3 different cell lines under 3 different cells densities (total 599 samples)

- Completed fluorescence lifetime data analysis, which are best fitted with two exponential components

- Extracted NADH fluorescence lifetime results for free NADH and protein bind NADH components

- Characterized NADH fluorescence lifetime results with different cell types.

REPORTABLE OUTCOMES

Publications:

1) Long Yan, Kevin W. Eliceiri, John G. White, Nirmala Ramanujam, Avtar S. Roopra and Patricia J. Keely, "FLIM reveals different states of bound NADH in human breast epithelial cells and breast carcinoma cells", Journal of Biomedical Optics, in revision

2) Provenzano PP, Inman DR, Eliceiri KW, Knittel JG, Yan L, Rueden CT, White JG, Keely PJ. Collagen density promotes mammary tumor initiation and progression, BMC Medicine. 2008. Apr 28;6(1):11.

3) P.P. Provenzano, C.T. Rueden, S.M. Trier, L.Yan, S.M. Ponik, D.R. Inman, P.J. Keely, and K.W. Eliceiri**.** Nonlinear Optical Imaging and Spectral-Lifetime Computational Analysis of Endogenous and Exogenous Fluorophores in Breast Cancer. Journal of Biomedical Optics. 2008 May-Jun;13(3):031220.

CONCLUSION:

Fluorescence lifetime characterization of NADH may be used to reveal metabolic changes in vivo and has potential to be used as an early diagnostic tool for breast cancer. In this study, based on well controlled cell culture model, we investigated possible metabolic differences between human breast malignant cells (T47D and MDA-MB-231) and human breast epithelial cells (MCF10A). We found that the fluorescence lifetime of bound NADH is different between breast carcinoma and breast epithelial cells. Specifically, non-transformed breast epithelial MCF10A cells showed a significant decrease in the fluorescence lifetime and percent contribution of bound NADH as the cell plating density increased. However, in the transformed T47D and MDA-MB-231 cells, the lifetime and contribution of bound NADH was not responsive to cell plating density. These findings suggest that unlike transformed cells, normal cells are able to affect metabolic adaptation as growth conditions change. Our findings demonstrate that fluorescence lifetime imaging (FLIM) can be used to distinguish between normal and malignant cells and open up the possibility of using non-invasive multiphoton FLIM monitoring of NADH as a diagnostic tool in cancer detection.

REFERENCES:
1.   O. Warburg, K. Posener and E. Negelein, "Metabolism of carcinoma cells," Biochemische Zeitschrift 152(309-344 (1924)

2.   O. Warburg, "On the origin of cancer cells," Science 123(3191), 309-314 (1956)

3.   O. Warburg, F. Wind and E. Negelein, "THE METABOLISM OF TUMORS IN THE BODY," The Journal of General Physiology 8(6), 519-530 (1927)

4.   E. I. Chen, J. Hewel, J. S. Krueger, C. Tiraby, M. R. Weber, A. Kralli, K. Becker, J. R. Yates, 3rd and B. Felding-Habermann, "Adaptation of energy metabolism in breast cancer brain metastases," Cancer Res 67(4), 1472-1486 (2007)

5.   D. K. Bird, L. Yan, K. M. Vrotsos, K. W. Eliceiri, E. M. Vaughan, P. J. Keely, J. G. White and N. Ramanujam, "Metabolic Mapping of MCF10A Human Breast Cells via Multiphoton Fluorescence Lifetime Imaging of the Coenzyme NADH," Cancer Research 65(19), 8766-8773 (2005)

6   G. M. Palmer, P. J. Keely, T. M. Breslin and N. Ramanujam, "Autofluorescence spectroscopy of normal and malignant human breast cell lines," Photochem Photobiol 78(5), 462-469 (2003)

7.   H. D. Vishwasrao, A. A. Heikal, K. A. Kasischke and W. W. Webb, "Conformational dependence of intracellular NADH on metabolic state revealed by associated fluorescence anisotropy," J Biol Chem 280(26), 25119-25126 (2005)

 APPENDICES:
1) Long Yan, Kevin W. Eliceiri, John G. White, Nirmala Ramanujam, Avtar S. Roopra and Patricia J. Keely, "FLIM reveals different states of bound NADH in human breast epithelial cells and breast carcinoma cells", Journal of Biomedical Optics, in revision

2) Provenzano PP, Inman DR, Eliceiri KW, Knittel JG, Yan L, Rueden CT, White JG, Keely PJ. Collagen density promotes mammary tumor initiation and progression, BMC Medicine. 2008. Apr 28;6(1):11.

3) P.P. Provenzano, C.T. Rueden, S.M. Trier, L.Yan, S.M. Ponik, D.R. Inman, P.J. Keely, and K.W. Eliceiri. Nonlinear Optical Imaging and Spectral-Lifetime Computational Analysis of Endogenous and Exogenous Fluorophores in Breast Cancer. Journal of Biomedical Optics. 2008 May-Jun;13(3):031220.

FLIM reveals different states of bound NADH in human breast epithelial cells and breast carcinoma cells

Long Yan[1,2], Kevin W. Eliceiri[1,2,3], John G. White[1,2,3], Nirmala Ramanujam[1,6], Avtar S. Roopra[§1,5] and Patricia J. Keely[§1,3,4]

[1]Laboratory for Optical and Computational Instrumentation (LOCI)
1675 Observatory Drive
University of Wisconsin-Madison
Madison, WI 53706

[2]Department of Biomedical Engineering
1550 Engineering Drive
University of Wisconsin-Madison
Madison, WI 53706

[3]Laboratory of Molecular Biology
1525 Linden Drive
University of Wisconsin-Madison
Madison, WI 53706

[4]Department of Pharmacology
1300 University Avenue
University of Wisconsin-Madison
Madison, WI 53706

[5]Department of Neurology
1300 University Avenue
University of Wisconsin-Madison
Madison, WI 53706

[6]Department of Biomedical Engineering
Duke University
Durham, NC 27708-0281

[§]Co-Corresponding Authors:
Patricia J. Keely: 3630 MSC, 1300 University Ave, Madison, 53706, Tel 608-265-2398
Fax 608-262-1257, pjkeely@wisc.edu
 Avtar Roopra, 1765 MSC, 1300 University Ave, Madison, 53706 Tel 608-265-9072,
roopra@neurology.wisc.edu

Running Title: Detection of Metabolic Plasticity in Breast Cancer

1

Abstract:

One of the earliest discovered and most consistent differences between cancer cells and normal cells is the heightened rate of glycolysis, which was described by Otto Warburg nearly three quarters of a century ago. Although the nature of this metabolic difference is not fully understood, changes in the levels of the bound and free forms of the metabolite NADH is a manifestation of this difference. In order to gain insight into the metabolic differences between normal and malignant cells, we exploited the fact that NADH is intrinsically fluorescent and that the bound and free states of NADH have distinct fluorescence lifetimes. We found that the fluorescence lifetime of bound NADH is different between breast carcinoma and untransformed breast epithelial cells. Specifically, non-transformed breast epithelial MCF10A cells showed a significant decrease in the fluorescence lifetime and percent contribution of bound NADH as the cell plating density increased. However, in the transformed T47D and MDA-MB-231 cells, the lifetime and contribution of bound NADH was not responsive to cell plating density. These findings suggest that unlike transformed cells, normal cells are able to affect metabolic adaptation as growth conditions change. Our findings demonstrate that fluorescence lifetime imaging (FLIM) can be used to distinguish between normal and malignant cells and open up the possibility of using non-invasive multiphoton FLIM monitoring of NADH as a diagnostic tool in cancer detection.

2

1. Introduction

Otto Warburg demonstrated in the first half of the 20th Century that tumor cells have a higher rate of glycolysis than normal cells and this 'Warburg Effect' is the basis for Positron Emission Tomography (PET) analysis of tumors used today in the clinic(1-4). The mechanisms that link tumor progression and metabolic state are still not fully understood, in part because in has been difficult to visualize the dynamics of metabolism *in vivo*. Thus, there is great interest in non-invasive imaging techniques that would allow one to monitor changes in metabolism between normal and carcinoma cell lines. One potentially powerful method to study metabolism *in vivo* is to monitor the intrinsic fluorescence of metabolic intermediates, such as reduced Nicotinamide Adenine Dinucleotide (NADH).

NADH plays a key role as a carrier of electrons and is involved in many important metabolic pathways, including glycolysis (5). NADH has two forms in cells: free and protein bound. Most bound NADH is found in the mitochondria while free NADH exists in both the cytoplasm and the mitochondria (6, 7). The utilization of NADH in various pathways is associated with NADH binding to different proteins. For example, NADH binds to Lactate dehydrogenases (LDH) in the cytoplasm to maintain ongoing glycolysis whereas in the mitochondria, NADH binds to other cofactors to facilitate the electron transport chain. Therefore, discerning the various species of bound NADH can help to reveal which metabolic pathways are active in normal and cancerous cells.

NADH fluorescence intensity changes have been used to study cell metabolic activity *in vivo* for many years (8-15). In addition to fluorescence intensity, all fluorophores have two additional properties of fluorescence that are relevant for these studies: the fluorescent lifetime and the fluorescent spectra. The fluorescence lifetime is a measure of how long a

fluorescent molecule stays in its excited state, and is directly influenced by changes in the immediate molecular environment of the molecule, such as pH or association with hydrophobic structures such as membranes (16-18). The bound and free states of NADH have been shown to have different distinct lifetimes *in vitro* and can be visualized by Fluorescence Lifetime Imaging Microscopy (FLIM)(19). Bound NADH has longer fluorescence lifetime (approximately 1.0ns) while free NADH has been shown to have a short fluorescent lifetime of 0.4ns due to quenching of the fluorescent nicotinamide group by the adenine moiety (16). A fluorescence spectrum is the emission intensity as a function of wavelength of a fluorophore and can be used to differentiate one fluorophore from another: for example FAD and NADH can be distinguished based on their different fluorescence spectra (20).

The ability of FLIM to probe cellular environment changes using endogenous NADH has been applied to a variety of studies in tissues such as fundus, retina, breast, and the brain, where altered metabolic rates are known to be involved in normal and disease processes(21-31). A previous study from our laboratory showed that the fluorescence lifetime and contribution of protein-bound NADH significantly decreased when the density of nontransformed breast epithelial cells was increased (32). In the present study, we have compared nontransformed human breast epithelial cells with two breast carcinoma cell lines and determined the fluorescence lifetime of free and bound NADH. Our results demonstrate that changes in lifetime of bound NADH as a function of growth condition can be used to differentiate malignant from normal cells.

2.   **Materials and Methods**

2.1 *Sample Preparation, Experiments and Viability Assessment*

Three human breast cell lines, MCF10A, T47D and MDA-MB-231; were all obtained from the American Type Culture Collection (http://www.atcc.org). The cells remained free of mycoplasma and other contaminants and were propagated by adherent culture according to established protocols (33). For the fluorescence intensity study, cell culture media was swapped into a common media: DMEM supplemented with 5% horse serum, 20 ng/mL epidermal growth factor, 10 ug/mL insulin and 0.5 ug/mL hydrocortisone. Plated cells were stored in a 10% CO_2 incubator at 37°C and cultured every 3-4 days. The cell preparation procedure was the same as used in previous NADH lifetime studies (32) with three cell densities investigated: 10,000, 100,000 and 1 million cells per 35 mm plate.

2.2 NADH emission spectra study:

NADH powder (Sigma, product number N 6660) was dissolved in distilled water and the solution placed in a glass bottom Petri dish (from MatTek Corporation, Ashland, MA) for imaging. The emission spectra data was collected by our custom built combined spectral and lifetime system (34, 35). Emission spectra of MCF10 cells at 3 different densities were imaged at the same instrument settings. The spectral response of the instrument was calibrated with a standard spectral lamp (Optronic Laboratories Inc., Orlando, FL, Model: OL 220M).

2.3 Fluorescence lifetime of NADH and LDH bound NADH solution study:

Free NADH solution was made and imaged as above.   LDH bound NADH was made by adding LDH (from Sigma Co., St. Louis MO, product number L3916) into free NADH solution. Fluorescence lifetime data were collected over 60 seconds using the same instrument settings. Fluorescence lifetime data analysis was done using SPCImage (Becker & Hickl GmbH, Berlin, Germany).

5

2.4 Cell density study:

A total of 14 independent imaging sessions were conducted over the course of approximately two months. For any given session and each cell line, three (3) independent dishes at the three (3) different cell density (10,000; 100,000; and 1 million cells per plate) were plated the day before and permitted to grow overnight in the incubator. At least 5 different regions were imaged for each plate with multiphoton FLIM under exactly the same instrument settings and collection time of 60 seconds.

2.5 Fluorescence intensity study:

Three (3) independent imaging sessions were conducted over the course of approximately two weeks. For any given session and each cell line, three independent dishes at the three different cell density (10,000; 100,000; and 1million cells per plate) were plated the day before and permitted to grow overnight in the incubator with same culture media. At least six different regions were imaged for each plate with multiphoton FLIM using exactly the same hardware settings.

2.6 Mitochondria localization study:

To localize the NADH signal to the mitochondria, cells were incubated for 45 minutes in 10 nM MitoTracker Green FM dye, which has a emission peak at 516nm (Catalog number: M7514, Molecular Probes, Eugene, Oregon). Intensity images were collected either with no filter (for total intensity measurement) or one of two filters: 480nm to 550nm band pass (for MitoTracker Green signal, 480:550bp TFI Technologies, Greenfield MA) and 490nm Short Pass filter (for NADH signals, 490SP, TFI Technologies, Greenfield MA).

2.7 Viability assessment:

6

At the completion of each imaging session, cell viability was confirmed under brightfield microscopy (using the same microscope) by Trypan Blue exclusion, which was performed without moving the sample and observing the same field as that imaged with multiphoton FLIM. All three confluences were imaged under identical experimental conditions and remained viable throughout any given imaging session.

2.8 Instrument setup and fluorescence lifetime analysis

2.8.1 Instrument:

A detailed description of the multiphoton FLIM has been described previously (32), Briefly, the system consists of a Ti:Sapphire mode-locked laser cavity (Coherent, Mira) pumped by an 8 W solid-state laser (Coherent, Verdi), an inverted microscope (Nikon, TE2000), a homemade scanning unit and a fast photon-counting detector (H7422, Becker & Hickl). More detailed information of this system has been described (32, 34). Multiphoton FLIM images were acquired with an electronic system for recording the time of arrival of fluorescence photons relative to the excitation laser pulses by time-correlated single photon counting (SPC-830, Becker & Hickl). Synchronized fluorescence lifetime data collection on a pixel-by-pixel basis was achieved using the *x* and *y* laser scanning signals controlled by WiscScan (http://www.loci.wisc.edu/WiscScan/).

2.8.2 Imaging Parameters

NADH has an absorption peak at a wavelength of 350 nm and emission peak wavelength of approximately 450 nm (19). As in our previous study (32), the laser was tuned to the 780 nm, which is close to the ideal two-photon absorption peak of NADH. All images were obtained on the same multiphoton microscope with same settings at maximum resolution of the Becker and

Hickl SPC-830 lifetime board (256x256 pixels). Six or more separate images of grouped cells were collected per dish, with the *minimum* spacing between observed groups being approximately 200 µm. The total number of images acquired in three cell lines at three densities experiments was 599. Photon counting was performed at a rate of approximately 5×10^5 photons/sec for 60 seconds. The pixel dwell time was approximately 6.5 µs.

2.8.3 Imaging Standards

The instrument response function (IRF) of the optical system was measured using the second harmonic generated signal from a beta-BaB_2O_4 (BBO) crystal (35). The measured full width at half maximum (FWHM) of the IRF was determined to be approximately 300 ± 10 ps. Fluorescein coated polystyrene beads (Molecular Probes, Eugene, Oregon) were used as a lifetime standard using previously published values (32, 36).

2.8.4 Fluorescence lifetime Analytical Methods

Fluorescence lifetime decay curves were fitted by the commercial software package, SPCImage (Becker & Hickl GmbH, Berlin, Germany). The measured lifetime decay curves were summed over the pixel of interest and surrounding 80 pixels (Bin of 4 in SPCImage Software). As the result, the peak value of the produced lifetime decay is about 1000 counts, which yielded the best lifetime fit. The two exponential fluorescence decay model is applied to globally fit the whole image:

$$I(t) = \alpha 1 \exp(-t/\tau 1) + \alpha 2 \exp(-t/\tau 2) + C,$$

Where I(t) is the fluorescence counts that were collected at time t after excitation. $\tau 1$ and $\tau 2$ are the fluorescence lifetime values from the short and long components respectively, and a1

and a2 are the percent contributions from the two components (i.e. a1 + a2 = 100%). C is from background noise. The quality of the nonlinear curve fit was determined and statistically measured by the minimum reduced (weighted) χ^2 (37). A perfect fit would have the value of 1.0.

The short and the long fluorescence lifetime components along with their relative contributions were extracted from the histogram of global fitting. The average values and standard deviation of each of these parameters per cell per density was determined from the total number of images analyzed.

3.   Results

Tumor cells exhibit increased rates of glycolysis compared to normal cells. As a first step in visualizing this difference using the natural fluorescent properties of NADH we obtained fluorescence intensity images of the non-transformed MCF10A breast epithelial cell line and the transformed lines T47D and MDA-MB-231. Figure 1 shows fluorescence intensity images of all three cell lines at three different densities. All cells were cultured under same medium and all images were obtained under identical experimental conditions with 780 nm laser excitation. The intensities were collected by the same photomultiplier (PMT) with same gain settings. It can be seen that the two malignant cell lines (T47D and MDA-MB-231) have an intensity distribution that stays constant over 3 different cell densities. However, the intensity distribution of the NADH signal from breast epithelial cell line (MCF10A) varies from point distribution at low density to uniform distribution over cytoplasm at high density.   These results show that whereas in the malignant lines NADH fluorescence remains constant as a function of increasing cell density, it re-distributes spatially and decreases in intensity in the normal epithelial cell line.

9

3.1 The endogenous signal originating from mitochondria matches the emission spectra and the lifetime analysis of NADH

To gain insight into the species of NADH contributing to the observed fluorescence, the emission spectrum acquired from MCF10A cells was compared to that of an aqueous solution of NADH *in vitro*. The emission spectra of free aqueous NADH and MCF10A cells (at 100k cells per plate) have peaks at 450nm and similar emission spectra (from 400nm to 550nm) (see Figure 2a). The fact that these spectra match closely suggests that both signals are from the same fluorophore (NADH) and are consistent with other studies (20, 38-40). One of the main cellular compartments to which NADH localizes is the mitochondria. We compared the location of endogenous NADH signal with respect to mitochondria. Mitotracker Green FM (Molecular Probes, Eugene, Oregon) is a commercial probe that stains mitochondria *in vivo*. The overlayed color map (Figure 2b) shows that the Mitotracker signal (green) and the autofluorescence (red) were from the same location and that the autofluorescence signals therefore predominantly originate from mitochondria.

Furthermore, the lifetime of aqueous NADH has a mean lifetime of 440ps (single exponential fitting by SPCImage software), which is consistent with other reports (7, 21, 25, 41, 42). To validate that our imaging analysis protocols could resolve NADH fluorescence into a 2-comonent fit corresponding to bound and free NADH, lifetime data of aqueous NADH with addition of purified LDH was acquired. The data fits a two components model of a short lifetime component (free NADH) at 440ps and a long lifetime component (LDH bound NADH) at 1.8ns (see table in figure 2c). This result suggests that our imaging analysis protocol can discern free NADH and protein bound NADH.

3.2Cell density affects the fluorescence lifetime of bound NADH in normal breast epithelial cells

We found that the lifetime of the short lifetime component is constant in breast epithelial cells and carcinoma cells despite changes in cell density. The lifetime analysis yielded the same short lifetime decay (free NADH) at three densities for three cell lines. The lifetime data were best fitted with two exponential decays: a short lifetime component (free NADH) and a long lifetime component (bound NADH). The short lifetime decay τ_1 (free NADH) had a mean lifetime of 450ps (see chart B in Figure 3.), which is the same as the lifetime we observed for free NADH in solution. Thereby, from here on, we will refer to the short lifetime component as free NADH. Likewise, we will refer to the long lifetime component as bound NADH. The lifetime of free NADH (τ_1) remained constant in all three cell lines at all three cell plating densities. There was not a statistically significant difference in a total of 599 samples.

The lifetime of bound NADH (τ_2) shows density dependent changes in breast epithelial cells but not in carcinoma cells. When cell density was increased from 10,000 cells per plate to 1 million cells per plate in the untransformed human breast epithelial cell line (MCF10A), the lifetime of bound NADH (τ_2) showed a significant decrease from 3.2ns to 2.6ns (Figure 3). When the lifetime is spatially displayed as a color map (Figure 3a), the bound NADH lifetime (τ_2) color changed from the red range in low density cultures (approximately 3.2ns. at 10K/plate) to the blue range at high density (approximately 2.5ns at 1 million/plate). At the intermediate density, i.e. 100,000 cells per plate, the color mapped is mixed (panel ii).

In contrast to the lifetime changes in nontransformed breast epithelial cells, the lifetime of bound NADH (τ_2) in transformed breast carcinoma cells remained constant when cell density increased. The representative pseudo color maps of T47D cells (figure 3, panel iv, v and vi) and

11

MDA_MB_231 cells (figure 3, panel xii, xiii and ix) are all in the blue range, demonstrating that there were no significant lifetime changes among them. This can also be noted in the chart quantitatively representing the lifetime of bound NADH ($\tau2$) (figure 3c), which demonstrates that there were no significant differences for bound NADH lifetime (τ_2) when cell density varied in breast carcinoma cells. The mean lifetime of bound NADH (τ_2) was 2.5ns in T47D cells and 2.4ns in MDA-MB-231cells.

The contribution of bound NADH (a2) shows density dependent changes in breast epithelial cells, but not in carcinoma cells. In addition to determining the value of the fluorescence lifetime for bound NADH ($\tau2$), we also determined the contribution of bound NADH, which is the percentage of the total of bound (a2) and free (a1) NADH, where a1 + a2 = 100%. Consistent with our observations of the lifetime of bound NADH ($\tau2$), in the human breast epithelial cell line (MCF10A), the contribution of bound NADH (a2) significantly decreased from 43% at low density to 33% at high density (P< 0.001, ANOVA total 214 samples) (Figure 4b) In the represented color maps(figure 4A), the contribution of bound NADH (a2) changes from the red range in low density cultures (43%. panel a) to the blue range in high density cultures (approximately 33%, panel c).

In contrast to nontransformed MCF10A cells, the contribution of bound NADH (a2) was not altered by cell plating density in breast carcinoma cells (T47D and MDA_MB_231). The representative color maps of T47D cells (figure 4, panel d, e and f) and MDA_MB_231 cells (figure 4, panel g, h and l) remained in the blue range (~30%), with no significant color change. When represented graphically (Figure 4B), the contribution of bound NADH (a2) was not

12

significantly different when cell density varied in T47D or MDA-MB-231 cells. The mean

contribution of bound NADH (a2) was 32% for T47D cells and 29% for MDA-MB-231cells.

The lifetime (τ_2) and contribution (a2) of bound NADH show a strong linear correlation.

MCF10A cells displayed a range of both lifetime and contribution values for bound NADH as a

function of cell density. We used this observation to ask whether there was any correlation

between lifetime and contribution of bound NADH. Figure 5 shows a scatter plot of all

MCF10A lifetime measurements versus the corresponding contribution values. There was a

strong linear correlation between the lifetime and contribution of bound NADH (linear

coefficient=0.84, total samples = 214). This analysis suggests that the changes in contribution in

MCF10A may, in part be due to the changes in lifetime of bound NADH i.e. a change in

contribution may occur in the absence of a change in concentration but instead be due to a

change in NADH-bound species and therefore lifetime.

4.   Discussion

Endogenous fluorophores provide a potentially powerful resource for obtaining *in situ*

information about the metabolic state of cells. However, one critical challenge in using this

fluorescence information is to accurately identify the endogenous components that contribute to

the signal. In breast cells (MCF10A, T47D and MDA-MB-231) there are three principle

fluorophores present – NADH, flavin adenine dinucleotide (FAD) and tryptophan, the spectral

characteristics of which have been characterized previously (20). We concluded that the detected

autofluorescence signal under these conditions (excitation at 780 nm) is mainly from NADH

based on three lines of evidence: 1) The fluorescence spectrum measured from MCF10A cells

matches the spectrum of a pure NADH solution (see fig 2a) as well as the reported spectral

13

properties of NADH in other reports (20, 25), suggesting that the autofluorescence signal we detect is indeed predominantly from NADH. 2) Further support for the endogenous signal originating from NADH is its co-localization to the mitochondria, an organelle that has high endogenous levels of this dinucleotide. 3) The measured short lifetime decay value ($\tau1$) we observe in cells is the same as the lifetime decay of free NADH in solution, and is also consistent with other reports (7, 19, 21, 25, 42-46), which further supports the notion that the autofluorescence signal is from NADH.

Fluorescence lifetime measurements are sensitive to local conditions of the molecular environment such as pH, ion concentration, and bound protein (16-19). Compared to tissue studies, a cell culture environment is relatively simple and easier to control. From our study, the lifetime of the shorter NADH component remains constant across three different cell lines at three different cell culture conditions and is indistinguishable from that measured from free NADH in solution. These observations indicate that the shorter NADH component observed in cells derives from free NADH. In contrast to free NADH lifetime values, our data show cell density-dependent changes in the long lifetime value (bound NADH) in breast epithelial cells: the lifetime of bound NADH significantly decreases from 3.2 ns to 2.5 ns as cell density increases. This change in the lifetime of bound NADH may reflect a shift to different metabolic pathways and the binding of NADH to different proteins within cells as they become more confluent. However, such responsiveness to the changes in cell densities did not occur in two breast carcinoma cell lines (T47D and MDA-MB-231), in which both the lifetime ($\tau2$) and contribution (a2) of bound NADH are constant even as cell density increases. The question arises as to why changes in NADH fluorescence properties occur in the 'normal' non-transformed MCF10A cells but not in the malignant T47D and MDA-MB-231 cells. The

14

cytoplasmic/nuclear concentration of NADH is predominantly set by the rates of 2 reactions (those catalysed by the glycolytic enzymes GAPDH and LDH) and the mitochondrial NADH concentration is set by flux through the TCA cycle and electron transport chain. Thus the alterations in NADH that are observed in normal but not malignant cells likely reflects alterations in pathways of energy metabolism that occur in normal cells but not in malignant cells as a function of growth conditions – in this case, cell density. This notion is consistent with the observation that transformed cells generally have high rates of glycolysis, poor mitochondrial function and are prodigious consumers of glucose due to their poor ability to metabolize alternative energy sources(1-3, 47-51).. This characteristic 'metabolic rigidity' of cancer cells should be compared to the 'metabolic plasticity' manifest in non-transformed epithelial cells and indeed is the basis for FDG imaging of tumors whereby the glucose analogue 2-Fluoro-Deoxy-D-Glucose (FDG) is preferentially taken up by tumors over normal tissue(52).

In support of the idea that 1) the malignant cells in this study are more 'glycolytic' and that 2) the decrease in bound lifetime of NADH fluorescence is due to a density dependent – perhaps oxygen diffusion limited - increase in the rates of glycolysis in MCF10A, the lifetime of NADH under hypoxia or tumor in tissue is shorter than that of their normal counterpart(25, 30, 53).   The significance of these findings is that the non-invasive technique of FLIM was able to detect the well-characterized metabolic rigidity of transformed cells that is the basis of radio-active PET imaging of tumors. The ability to distinguish between metabolically plastic normal cells and metabolically rigid cancer cells in a non-invasive, non-radioactive manner presents exciting possibilities for the future of cancer detection in patients.

In addition to the lifetime of bound NADH, the contribution of bound NADH is also decreased in nontransformed breast epithelial cells as they are grown under more dense

15

conditions and we find a strong linear correlation between the lifetime ($\tau2$) and the contribution (a2) of bound NADH. Indeed the linear correlation coefficient of 0.84 between $\tau2$ and a2 suggests that one does not need to invoke a change in concentration of bound NADH to explain the change in contribution – the change in contribution can be almost entirely explained by the change in lifetime. Because contribution (intensity) is a function of quantum efficiency as well as concentration and since the quantum efficiency of a fluorophore is proportional to the lifetime of the fluorophore(16), this strong correlation between lifetime and contribution of bound NADH suggest that the change in contribution of bound NADH (a2) is mainly due to the change in the quantum efficiency of bound NADH. Furthermore, this suggests that the concentrations of free and bound NADH are constant in different conditions and that it is the nature of the bound species that is altered, such as the binding partner. A cautionary note therefore, is that interpreting changes in contribution of fluorescence as a change in concentration is only possible if lifetime changes are negligible under the conditions used.

In summary, we find that imaging and quantitation of the fluorescence lifetime has the capability of revealing metabolic differences between normal and carcinoma cells, based on the states of bound NADH *in vivo*. A key advantage of using the lifetime component measurements rather than the intensity of NADH for cancer characterization is that lifetime measurements are independent of NADH concentration and do not need to be calibrated for cell or instrumentation variations. Our findings demonstrate that fluorescence lifetime imaging can be used to distinguish between normal and malignant cells and opens up the possibility of using non-invasive, non-radioactive multiphoton FLIM of NADH as a diagnostic tool in cancer detection.

ACKNOWLEDGMENTS

References

1.   O. Warburg, K. Posener and E. Negelein, "Metabolism of carcinoma cells," Biochemische Zeitschrift 152(309-344 (1924)

2.   O. Warburg, "On the origin of cancer cells," Science 123(3191), 309-314 (1956)

3.   O. Warburg, F. Wind and E. Negelein, "THE METABOLISM OF TUMORS IN THE BODY," The Journal of General Physiology 8(6), 519-530 (1927)

4.   E. I. Chen, J. Hewel, J. S. Krueger, C. Tiraby, M. R. Weber, A. Kralli, K. Becker, J. R. Yates, 3rd and B. Felding-Habermann, "Adaptation of energy metabolism in breast cancer brain metastases," Cancer Res 67(4), 1472-1486 (2007)

5.   J. M. Berg, J. L. Tymoczko and L. Stryer, Biochemistry 2001, W.H. Freeman and Company, New York (2002).

6.   M. Wakita, G. Nishimura and M. Tamura, "Some characteristics of the fluorescence lifetime of reduced pyridine nucleotides in isolated mitochondria, isolated hepatocytes, and perfused rat liver in situ," J Biochem (Tokyo) 118(6), 1151-1160 (1995)

7.   K. Blinova, S. Carroll, S. Bose, A. V. Smirnov, J. J. Harvey, J. R. Knutson and R. S. Balaban, "Distribution of mitochondrial NADH fluorescence lifetimes: steady-state kinetics of matrix NADH interactions," Biochemistry 44(7), 2585-2594 (2005)

8.   B. Chance, P. Cohen, F. Jobsis and B. Schoener, "Intracellular oxidation-reduction states in vivo," Science 137(499-508 (1962)

9.   B. Chance, J. R. Williamson, D. Famieson and B. Schoener, "Properties and kinetics of reduced pyridine nucleotide fluorescence of the isolated and in vivo rat heart.," Biochem Z. 341(357-377 (1965)

10.   D. J. Pappajohn, R. Penneys and B. Chance, "NADH spectrofluorometry of rat skin," J Appl Physiol 33(5), 684-687 (1972)

11.   Q. Zhang, S. Y. Wang, A. C. Nottke, J. V. Rocheleau, D. W. Piston and R. H. Goodman, "Redox sensor CtBP mediates hypoxia-induced tumor cell migration," Proc Natl Acad Sci U S A 103(24), 9029-9033 (2006)

12.   Q. Zhang, D. W. Piston and R. H. Goodman, "Regulation of corepressor function by nuclear NADH," Science 295(5561), 1895-1897 (2002)

13.   N. Ramanujam, M. F. Mitchell, A. Mahadevan, S. Thomsen, A. Malpica, T. Wright, A. Atkinson and R. R. Richards-Kortum, "Development of a multivariate statistical algorithm to analyze human cervical tissue fluorescence spectra acquired in vivo," Lasers Surg Med 19(1), 46-62 (1996)

14.   P. K. Gupta, S. K. Majumder and A. Uppal, "Breast cancer diagnosis using N2 laser excited autofluorescence spectroscopy," Lasers Surg Med 21(5), 417-422 (1997)

15.   S. K. Majumder, P. K. Gupta, B. Jain and A. Uppal, "UV excited autofluorescence spectroscopy of human breast tissues for discriminating cancerous tissue from benign tumor and normal tissue.," Lasers Life Sci 8(249-264 (1999)

16.   J. R. Lakowicz, Principles of Fluorescence Spectroscopy, Kluwer Academic, New York (1999).

17.   H. J. Lin, P. Herman and J. R. Lakowicz, "Fluorescence lifetime-resolved pH imaging of living cells," Cytometry Part A 52(2), 77-89 (2003)

18.   K. Suhling, P. M. French and D. Phillips, "Time-resolved fluorescence microscopy," Photochem Photobiol Sci 4(1), 13-22 (2005)

19. J. R. Lakowicz, H. Szmacinski, K. Nowaczyk and M. L. Johnson, "Fluorescence lifetime imaging of free and protein-bound NADH," Proc Natl Acad Sci U S A 89(4), 1271-1275 (1992)

20. G. M. Palmer, P. J. Keely, T. M. Breslin and N. Ramanujam, "Autofluorescence spectroscopy of normal and malignant human breast cell lines," Photochem Photobiol 78(5), 462-469 (2003)

21. K. Konig, M. W. Berns and B. J. Tromberg, "Time-resolved and steady-state fluorescence measurements of beta-nicotinamide adenine dinucleotide-alcohol dehydrogenase complex during UVA exposure," J Photochem Photobiol B 37(1-2), 91-95 (1997)

22. D. Schweitzer, A. Kolb, M. Hammer and R. Anders, "[Time-correlated measurement of autofluorescence. A method to detect metabolic changes in the fundus]," Ophthalmologe 99(10), 774-779 (2002)

23. P. J. Tadrous, J. Siegel, P. M. French, S. Shousha, N. Lalani el and G. W. Stamp, "Fluorescence lifetime imaging of unstained tissues: early results in human breast cancer," J Pathol 199(3), 309-317 (2003)

24. D. Grosenick, K. T. Moesta, H. Wabnitz, J. Mucke, C. Stroszczynski, R. Macdonald, P. M. Schlag and H. Rinneberg, "Time-domain optical mammography: initial clinical results on detection and characterization of breast tumors," Appl Opt 42(16), 3170-3186 (2003)

25. H. D. Vishwasrao, A. A. Heikal, K. A. Kasischke and W. W. Webb, "Conformational dependence of intracellular NADH on metabolic state revealed by associated fluorescence anisotropy," J Biol Chem 280(26), 25119-25126 (2005)

26. J. M. Levitt, A. Baldwin, A. Papadakis, S. Puri, J. Xylas, K. Munger and I. Georgakoudi, "Intrinsic fluorescence and redox changes associated with apoptosis of primary human epithelial cells," Journal of Biomedical Optics 11(6), 064012 (2006)

27. D. Sud, w. Zhong, D. G. Beer and M.-A. Mycek, "Time-resolved optical imaging provides a molecular snapshot of altered metabolic function in living human cancer cell models," Optics Express 14(10), 4412-4426 (2006)

28. D. Schweitzer, S. Schenke, M. Hammer, F. Schweitzer, S. Jentsch, E. Birckner, W. Becker and A. Bergmann, "Towards metabolic mapping of the human retina," Microscopy Research and Technique 70(5), 410-419 (2007)

29. L. M. Tiede, S. M. Rocha-Sanchez, R. Hallworth, M. G. Nichols and K. Beisel, "Determination of hair cell metabolic state in isolated cochlear preparations by two-photon microscopy," Journal of Biomedical Optics 12(2), 021004 (2007)

30. M. C. Skala, K. M. Riching, A. Gendron-Fitzpatrick, J. Eickhoff, K. W. Eliceiri, J. G. White and N. Ramanujam, "In vivo multiphoton microscopy of NADH and FAD redox states, fluorescence lifetimes, and cellular morphology in precancerous epithelia," Proc Natl Acad Sci U S A (2007)

31. A. Ehlers, I. Riemann, M. Stark and K. Konig, "Multiphoton fluorescence lifetime imaging of human hair," Microsc Res Tech 70(2), 154-161 (2007)

32. D. K. Bird, L. Yan, K. M. Vrotsos, K. W. Eliceiri, E. M. Vaughan, P. J. Keely, J. G. White and N. Ramanujam, "Metabolic Mapping of MCF10A Human Breast Cells via Multiphoton Fluorescence Lifetime Imaging of the Coenzyme NADH," Cancer Research 65(19), 8766-8773 (2005)

33. P. J. Keely, A. M. Fong, M. M. Zutter and S. A. Santoro, "Alteration of collagen-dependent adhesion, motility, and morphogenesis by the expression of antisense alpha 2 integrin mRNA in mammary cells," J Cell Sci 108 (Pt 2)(595-607 (1995)

34.   L. Yan, C. T. Rueden, J. G. White and K. W. Eliceiri, "Applications of combined spectral lifetime microscopy for biology," Biotechniques 41(3), 249, 251, 253 passim (2006)

35.   D. K. Bird, K. W. Eliceiri, C. H. Fan and J. G. White, "Simultaneous two-photon spectral and lifetime fluorescence microscopy," Appl Opt 43(27), 5173-5182 (2004)

36.   A. Schönle, M. Glatz and S. W. Hell, "Four-dimensional multiphoton microscopy with time-correlated single-photon counting," Appl Opt 39(6306-6311 (2000)

37.   A. Bergmann, "SPCImage: Data analysis software for fluorescence lifetime imaging microscopy," (2003).

38.   C. K. Brookner, M. Follen, I. Boiko, J. Galvan, S. Thomsen, A. Malpica, S. Suzuki, R. Lotan and R. Richards-Kortum, "Autofluorescence patterns in short-term cultures of normal cervical tissue," Photochem Photobiol 71(6), 730-736 (2000)

39.   N. Ramanujam, "Fluorescence Spectroscopy In Vivo," in Encyclopedia of Analytical Chemistry R. Meyers, Ed., pp. 20-56, John Wiley and Sons, Ltd (2000).

40.   B. R. Masters, P. T. So and E. Gratton, "Multiphoton excitation fluorescence microscopy and spectroscopy of in vivo human skin," Biophys J 72(6), 2405-2412 (1997)

41.   M. R. Kasimova, J. Grigiene, K. Krab, P. H. Hagedorn, H. Flyvbjerg, P. E. Andersen and I. M. Moller, "The free NADH concentration is kept constant in plant mitochondria under different metabolic conditions," Plant Cell 18(3), 688-698 (2006)

42.   Y. Wu, W. Zheng and J. Y. Qu, "Sensing cell metabolism by time-resolved autofluorescence," Optics Letters 31(21), 3122-3124 (2006)

43.   T. G. Scott, R. D. Spencer, N. J. Leonard and G. Weber, "Emission properties of NADH. Studies of fluorescence lifetimes and quantum efficiencies of NADH, AcPyADH, and simplified synthetic models.," J. Am. Chem. Soc. 92(687-695 (1970)

44.   A. Gafni and L. Brand, "Fluorescence decay studies of reduced nicotinamide adenine dinucleotide in solution and bound to liver alcohol dehydrogenase," Biochemistry 15(15), 3165-3171 (1976)

45.   D. M. Jameson, V. Thomas and D. M. Zhou, "Time-resolved fluorescence studies on NADH bound to mitochondrial malate dehydrogenase," Biochim Biophys Acta 994(2), 187-190 (1989)

46.   M. C. Skala, K. M. Riching, D. K. Bird, A. Gendron-Fitzpatrick, J. Eickhoff, K. W. Eliceiri, P. J. Keely and N. Ramanujam, "In vivo multiphoton fluorescence lifetime imaging of protein-bound and free nicotinamide adenine dinucleotide in normal and precancerous epithelia," J Biomed Opt 12(2), 024014 (2007)

47.   R. J. Gillies and R. A. Gatenby, "Hypoxia and adaptive landscapes in the evolution of carcinogenesis," Cancer Metastasis Rev 26(2), 311-317 (2007)

48.   K. Smallbone, R. A. Gatenby, R. J. Gillies, P. K. Maini and D. J. Gavaghan, "Metabolic changes during carcinogenesis: potential impact on invasiveness," J Theor Biol 244(4), 703-713 (2007)

49.   R. A. Gatenby, K. Smallbone, P. K. Maini, F. Rose, J. Averill, R. B. Nagle, L. Worrall and R. J. Gillies, "Cellular adaptations to hypoxia and acidosis during somatic evolution of breast cancer," Br J Cancer 97(5), 646-653 (2007)

50.   R. J. Gillies and R. A. Gatenby, "Adaptive landscapes and emergent phenotypes: why do cancers have high glycolysis?" J Bioenerg Biomembr 39(3), 251-257 (2007)

51.   M. C. Brahimi-Horn and J. Pouyssegur, "Oxygen, a source of life and stress," FEBS Letters 581(19), 3582-3591 (2007)

52. W. A. Weber, M. Schwaiger and N. Avril, "Quantitative assessment of tumor metabolism using FDG-PET imaging," Nuclear Medicine and Biology 27(7), 683-687 (2000)

53. H. Schneckenburger, M. Wagner, P. Weber, W. S. L. Strauss and R. Sailer, "Autofluorescence lifetime imaging of cultivated cells using a UV picosecond laser diode," J. Fluorescence 14(649-654 (2004)

Figure legends:

Figure 1: Multiphoton intensity images of endogenous fluorescence in three human breast cell lines: MCF10A (i, ii and iii), T47D (iv, v and vi) and MDA-MB-231(vii, viii and ix). Cells were cultured at three different plating cell densities (from top to bottom): 10K (i, iv and vii), 100 K(ii, v and viii) and 1 million cells per 35 mm plate (iii, vi and ix). Cells were imaged on a multiphoton FLIM workstation with λ_{EX} = 780 nm, which is close to the ideal two photon peak of NADH. Scale bar = 10μM. Images are representative of three independent experiments, with several images collected per experiment as described in the Methods.

Figure 2: Emission spectra of NADH dissolved in water (40mM, doted line) or a plate of MCF10A cells at 100,000 cells per plate (solid line). Spectra were collected using the multiphoton FLIM workstation at λ_{EX} = 780 nm with a 16 channel spectral/ lifetime detector and calibrated. Spatial resolution is 10nm per channel. Both the NADH solution and the MCF10A cells had the same emission peak at 450nm, supporting the identity of the endogenous fluorophore in MCF10A cells as NADH under these conditions. (B) NADH localizes in part to mitochondria. Cells were labeled with MitoTracker-Green FM and imaged at λ_{EX} = 780 nm. Endogenous NADH fluorescence (ii) was spectrally resolved from MitoTracker-Green FM (i) by a Low Band-Pass filter (490LP). Overlay image (iii) of NADH (pseudo colored red) and MitoTracker-Green FM (pseudo colored green) demonstrates co-localization of NADH to mitochondria. Scale bar = 10 μm. (C) Table of lifetime results from a solution of pure NADH and a mixed solution of LDH (lactose dehydrogenase) and NADH, which is bound to LDH.

22

Figure 3: Analysis of the fluorescence lifetime of bound NADH indicates changes in normal, but not in carcinoma cells across increasing cell-plating densities. (A) Color map of the lifetime of bound NADH from representative images for three cell lines: MCF10A (i, ii and iii), T47D(iv, v and vi) and MDA-MB-231(vii, viii and ix) at three plating cell densities: 10K (i, iv and vii), 100K (ii, v and viii) and 1million (iii, vi and ix) cells/ 35mm plate. The color scale is from 2.2ns (blue) to 3.5ns (red). Scale bar is 10 μm.

(B) Chart of the lifetime of free NADH (τ_1) for all the data collected across three cell densities as well as free NADH solution. There is no significant change in the lifetime of free NADH across all three cell lines at the three cell densities. The mean lifetime from cells is 0.45ns, which is same as the lifetime of free NADH in solution.

(C) Chart of the lifetime of bound NADH (τ_2) for all the data collected across three cell densities as well as LDH-bound NADH solution. There is a significant decrease in the lifetime of bound NADH when breast epithelial cells (MCF10A) were plated at densities that increased from 10K cells per plate to 1 million cells per plate (P<0.001 by ANOVA. The number of total samples is 214). However, there is not a significant change in carcinoma cells (T47D and MDA-MB-231) as cell plating density is increased. The lifetime of LDH bound NADH is 1.8ns.

Figure 4: Analysis of the contribution of bound NADH (a2) indicates changes in normal, but not carcinoma cells across increasing cell densities. Contribution of bound NADH is defined as percentage of bound NADH relative to the total NADH, i.e. Contribution = a2/ (a1 + a2). (A) Color maps of the percent contribution of bound NADH for representative images of the three cell lines: MCF10A (i, ii and iii), T47D(iv, v and vi) and MDA-MB-231(vii, viii and ix) at three

plating cell densities: 10K (i, iv and vii), 100K (ii, v and viii) and 1million (iii, vi and ix). The color scale is from 30% (blue) to 50% (red). Scale bar is 10 μm.

(B) Chart of the contribution of bound NADH (a_2) for all the data collected in the cell density study. There is a significant decrease in the contribution of bound NADH when the cell density of nontransformed breast epithelial cells (MCF10A) was increased from 10K cells per plate to 1 million cells per plate (P<0.001 by ANOVA. The number of total samples is 214). However, there is not a significant change in the a2 value for carcinoma cells (T47D and MDA-MB-231) across increasing cell densities.

Figure 5: Scatter plot of the lifetime of bound NADH (x axis) vs. the contribution of bound NADH (y axis) for nontransformed breast epithelial cells (MCF10A). Statistic analysis showed that there is a strong linear correlation between the lifetime of bound NADH (τ_2) and the contribution of bound NADH (a2) (linear coefficient is 0.84, total samples is 214)
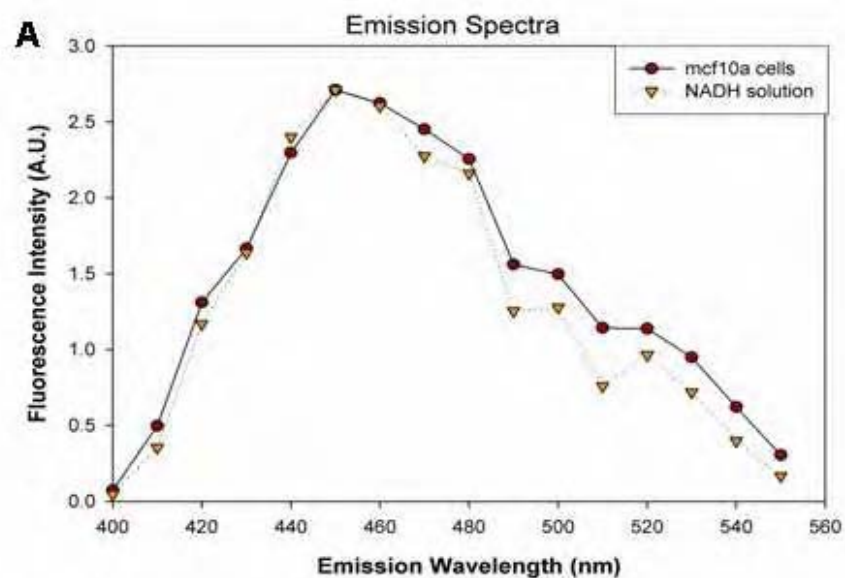
Figure 1

25

Figure 2

A. Emission Spectra
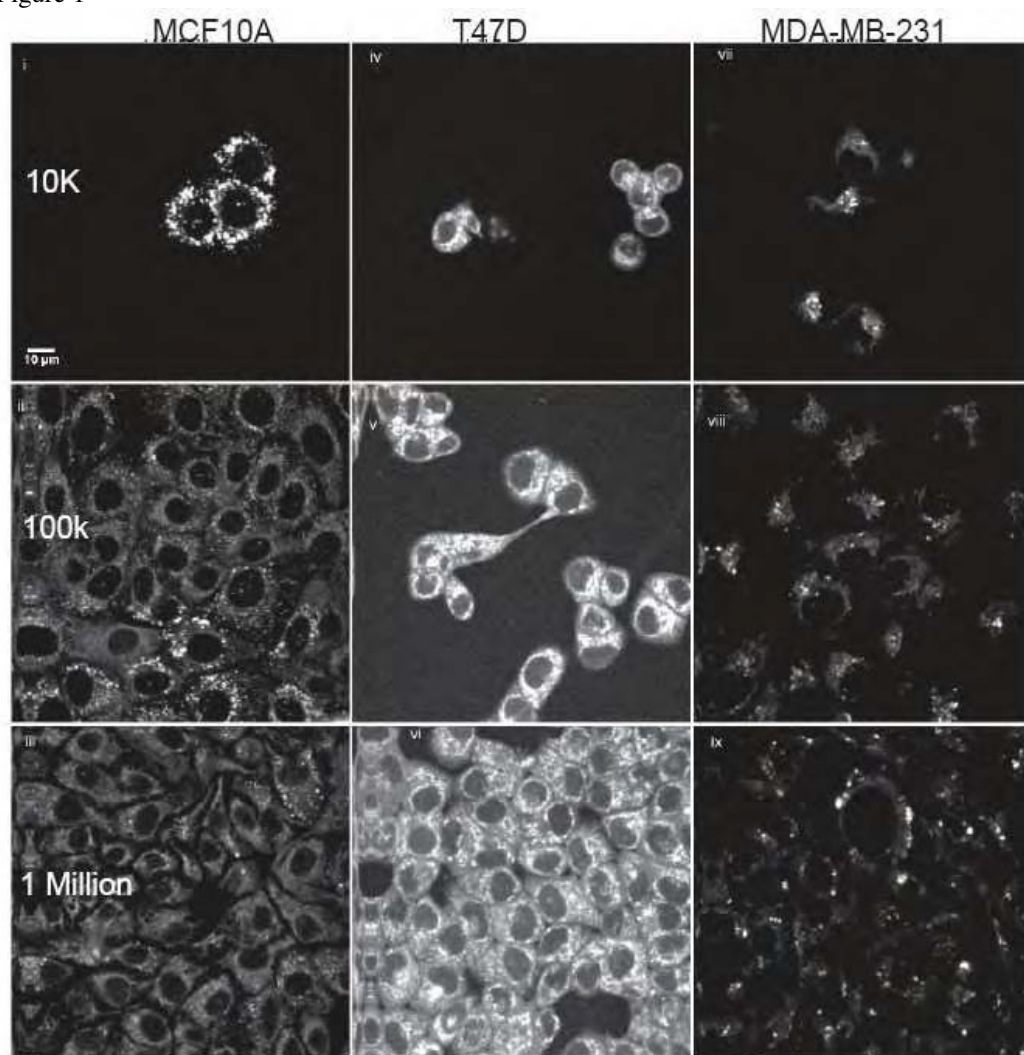
B. MitoTracker and NADH colocalization

C. Lifetime of free NADH and bound NADH

	Lifetime (ps)
Free NADH	400
NADH + LDH	1800
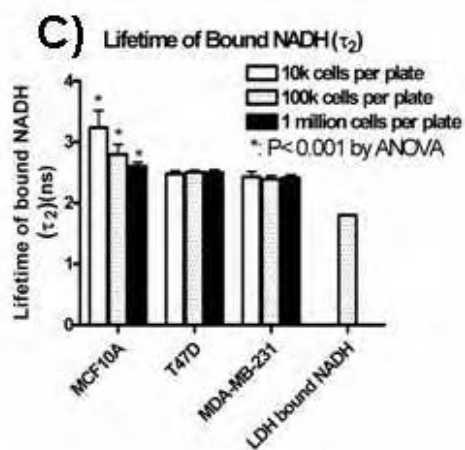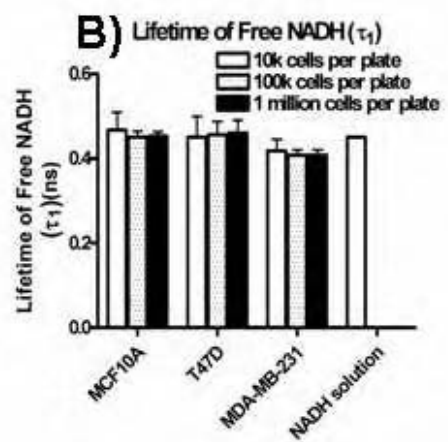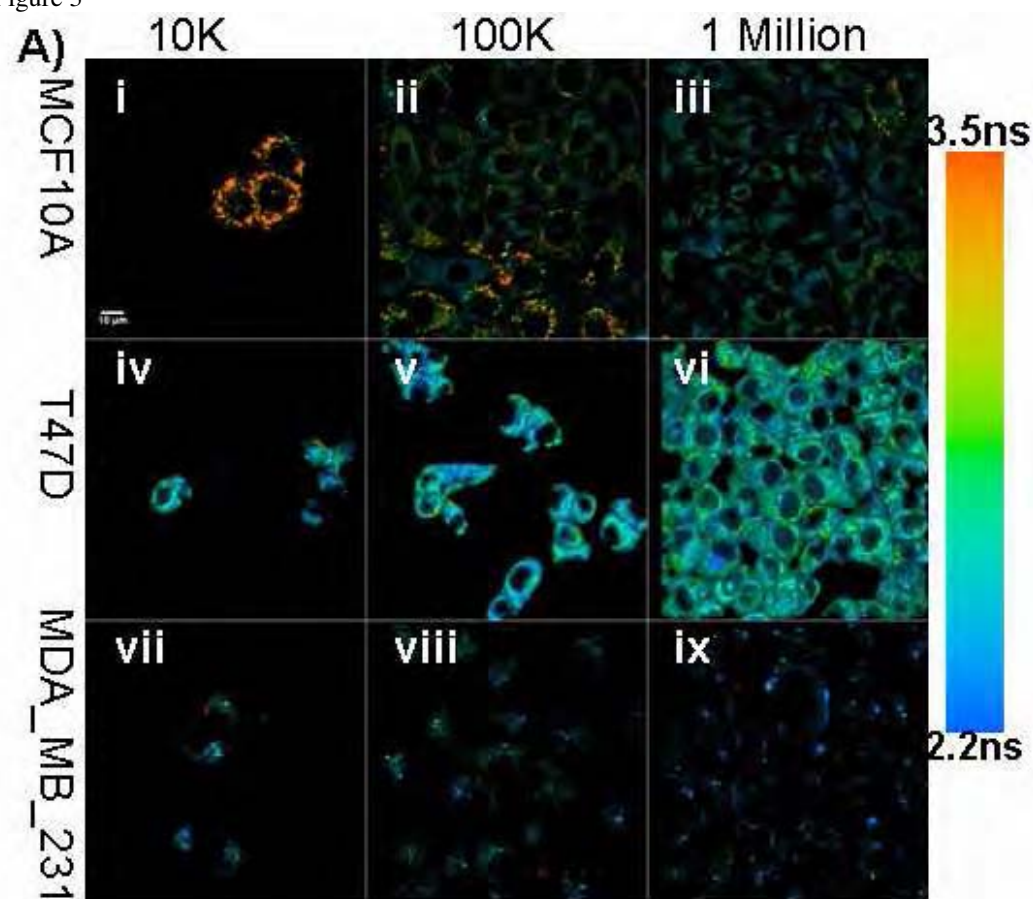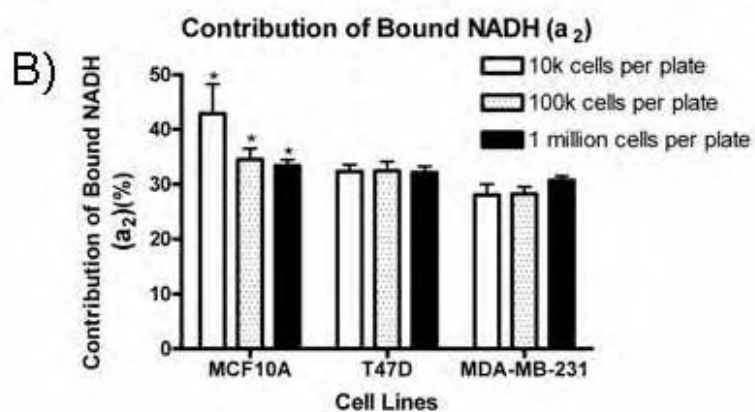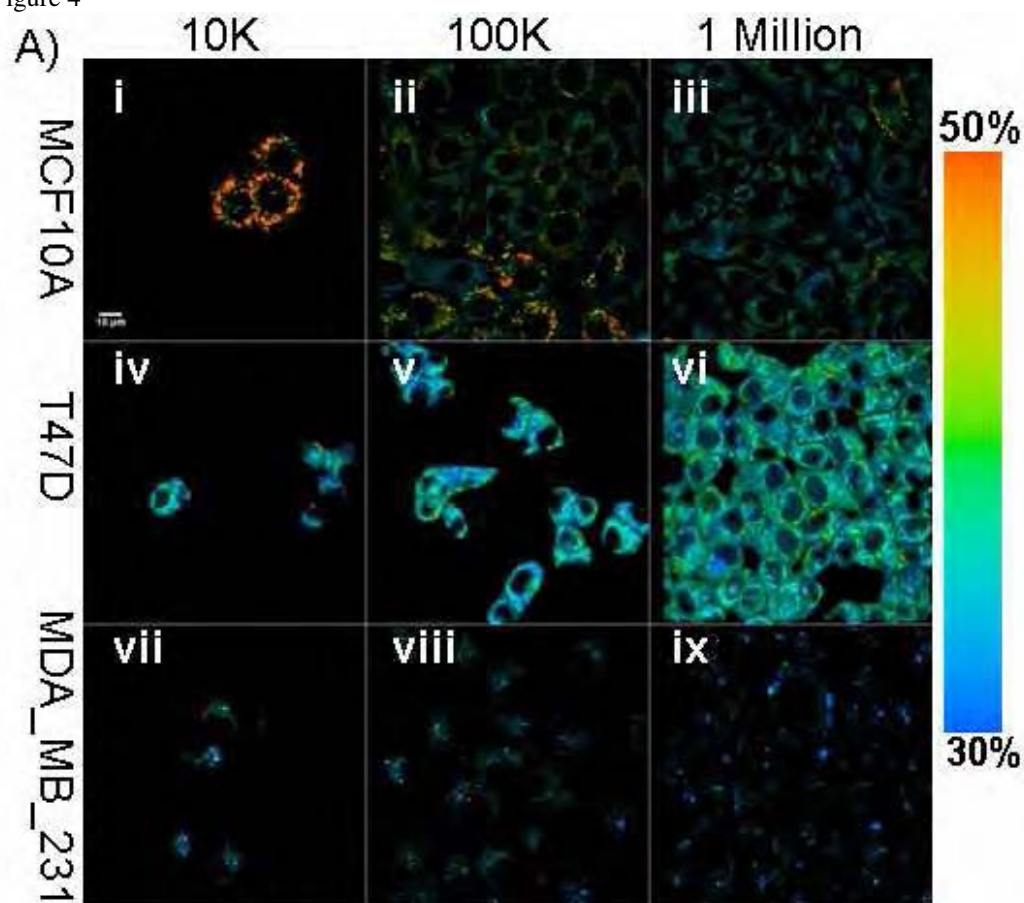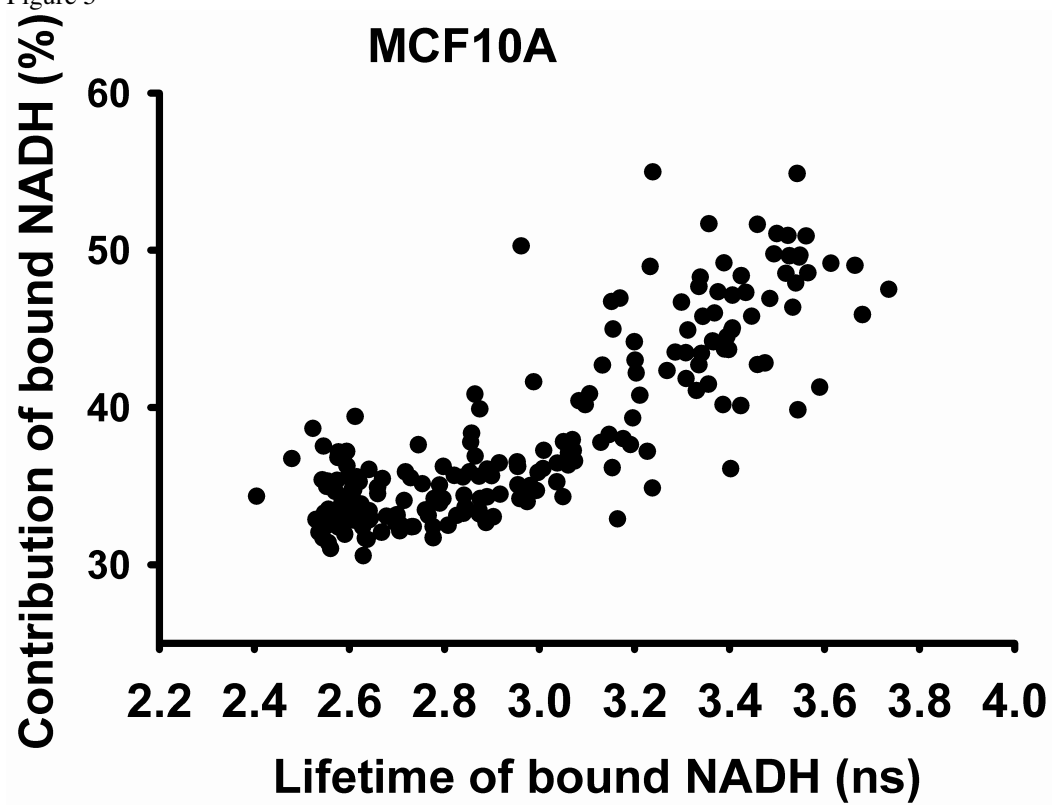
26

Figure 3

Figure 4

28

Figure 5

MCF10A

Research article

Collagen density promotes mammary tumor initiation and progression

Paolo P Provenzano*[1,2,3], David R Inman[1,3], Kevin W Eliceiri[2], Justin G Knittel[1], Long Yan[2], Curtis T Rueden[2], John G White[2] and Patricia J Keely*[1,2,3]

Address: [1]Department of Pharmacology, University of Wisconsin, Madison, WI 53706, USA, [2]Molecular Biology Program, Laboratory for Optical and Computational Instrumentation, University of Wisconsin, Madison, WI 53706, USA and [3]University of Wisconsin Paul P. Carbone Comprehensive Cancer Center, University of Wisconsin, Madison, WI 53706, USA

Email: Paolo P Provenzano* - ppproven@wisc.edu; David R Inman - drinman@wisc.edu; Kevin W Eliceiri - eliceiri@wisc.edu; Justin G Knittel - justin.knittel@case.edu; Long Yan - longyan@wisc.edu; Curtis T Rueden - ctrueden@wisc.edu; John G White - jwhite1@wisc.edu; Patricia J Keely* - pjkeely@wisc.edu

* Corresponding authors

Abstract

Background: Mammographically dense breast tissue is one of the greatest risk factors for developing breast carcinoma. Despite the strong clinical correlation, breast density has not been causally linked to tumorigenesis, largely because no animal model has existed for studying breast tissue density. Importantly, regions of high breast density are associated with increased stromal collagen. Thus, the influence of the extracellular matrix on breast carcinoma development and the underlying molecular mechanisms are not understood.

Methods: To study the effects of collagen density on mammary tumor formation and progression, we utilized a bi-transgenic tumor model with increased stromal collagen in mouse mammary tissue. Imaging of the tumors and tumor-stromal interface in live tumor tissue was performed with multiphoton laser-scanning microscopy to generate multiphoton excitation and spectrally resolved fluorescent lifetimes of endogenous fluorophores. Second harmonic generation was utilized to image stromal collagen.

Results: Herein we demonstrate that increased stromal collagen in mouse mammary tissue significantly increases tumor formation approximately three-fold ($p < 0.00001$) and results in a significantly more invasive phenotype with approximately three times more lung metastasis ($p < 0.05$). Furthermore, the increased invasive phenotype of tumor cells that arose within collagen-dense mammary tissues remains after tumor explants are cultured within reconstituted three-dimensional collagen gels. To better understand this behavior we imaged live tumors using nonlinear optical imaging approaches to demonstrate that local invasion is facilitated by stromal collagen re-organization and that this behavior is significantly increased in collagen-dense tissues. In addition, using multiphoton fluorescence and spectral lifetime imaging we identify a metabolic signature for flavin adenine dinucleotide, with increased fluorescent intensity and lifetime, in invading metastatic cells.

Conclusion: This study provides the first data causally linking increased stromal collagen to mammary tumor formation and metastasis, and demonstrates that fundamental differences arise and persist in epithelial tumor cells that progressed within collagen-dense microenvironments. Furthermore, the imaging techniques and signature identified in this work may provide useful diagnostic tools to rapidly assess fresh tissue biopsies.

Background

Mammographically dense breast tissue is linked to a greater than four-fold increased risk of breast carcinoma [1-3], and is one of the greatest independent risk factors for breast cancer [1,2,4]. For instance, breast density in more than 50% of the tissue may account for up to 30% of breast cancers, while BRCA1 and BRCA2 mutations, although conferring a greater relative risk, account for only 5% of breast cancers (see Boyd et al [5] and references therein). Breast tissue density is additionally increased with hormone replacement therapy [6], suggesting increased density may be part of the underlying mechanism by which hormone replacement therapy increases cancer risk. Furthermore, ductal carcinoma *in situ* (DCIS), a local precursor to some invasive breast cancers, arises overwhelmingly in dense regions of the breast [7]; and high breast tissue density is associated with a shift to more malignant tumors [8], an increased likelihood of DCIS [8,9], invasive breast carcinoma [9,10], lymphatic and vascular invasion [11], and an approximately three-fold greater risk of developing a second breast carcinoma [10]. However, although there is considerable correlative data identifying breast density as a risk factor for developing carcinoma, a causal link between breast density and carcinoma has not been established. Moreover, the molecular mechanisms driving breast density-related tumor formation and progression remain largely unknown.

Importantly, areas of increased breast density are not only associated with increased epithelial and stromal cellularity [12-14], but also significantly increased fibrillar collagen deposition [8,13,14]. In addition, it has been reported that levels of total collagen increase as radiographic breast tissue density increases [8,13]. This is significant since tissue microenvironments play an important role in maintaining normal cellular behavior [15,16], and stroma surrounding breast epithelial cells is believed to be critically involved in epithelial transformation, carcinoma growth, and metastasis [17-21]. Consistent with this concept, adipose-derived type VI collagen promotes tumor growth [22], while disturbing the epithelial-stromal interaction by disrupting the β1-integrin in mammary epithelial cells inhibits tumorigenesis [23]. A less considered aspect of the complexity of the epithelial-stromal interaction is the fact that the stroma is a dynamic mechanical microenvironment, with dense collagenous stroma transmitting multi-axial deformations to breast cells during tissue deformation and increasing resistance to cellular contractility. Such mechanical signals arising from increased density or rigidity of the microenvironment play a role in the transformed phenotype of breast epithelial cells [24,25]. Hence, although tumor formation is a multistep process involving genetic alterations of the epithelial cell, it has become clear that the epithelial-stromal interaction plays a crucial role in tumor formation and

progression. Therefore, due to the increased stroma associated with breast tissue density we hypothesized that increasing collagen density in the mammary gland would promote tumorigenesis. Although there is a strong correlative link between breast density and carcinoma, to date collagen density has not been causally linked to tumorigenesis, largely because studies utilizing animal models with different stromal density have not been performed previously. Here we demonstrate that mammary tumor formation, invasion, and metastasis are enhanced in collagen-dense stroma in a transgenic mouse model.

Methods

Mice

The University of Wisconsin animal use and care committee approved this study. Breeding pairs of Col1a1[tmJae] mice [26] in the B6/129 background were obtained from Jackson Laboratory. Male FVB Polyomavirus middle-T mice under the control of the mammary specific MMTV promoter were originally obtained from Dr Amy Moser (University of Wisconsin) and are abbreviated PyVT following the Jackson Laboratory (from which they originated) nomenclature, but are also commonly abbreviated as PyMT or PyV MT. Col1a1[tmJae] homozygote males were crossed to C57BL/6 females to generate heterozygous females that were crossed to PyVT males to generate mice with normal and collagen-dense mammary tissues carrying the polyoma transgene. Mice were palpated every 2 to 3 days starting at 8 weeks of age to identify tumors. Genotyping by polymerase chain reaction (PCR) was performed on DNA extracted from tail biopsies (Wizard SV Genomic DNA Purification System, Promega, Madison, WI) using primers indicated in the strain information provided by The Jackson Laboratory. Mice were examined for palpable tumors starting at eight weeks of age and humanely killed at 15 weeks or when the tumor burden became excessive.

Histology and mammary gland whole mounts

Selected mammary tissues and tumors were fixed in 4% paraformaldehyde in phosphate buffered saline (PBS) and then embedded in paraffin. In addition, all tissues imaged with multiphoton microscopy were subsequently fixed and processed for histology. Tissue sections were stained with hematoxylin and eosin (H&E) with adjacent sections stained with the selective collagen stain, picrosirius red. Mammary whole mounts were prepared by fixing tissues in Carnoy's solution (10% glacial acetic acid, 30% chloroform, and 60% absolute ethanol), followed by rehydration and staining with carmine alum. Tissues were then dehydrated, cleared with xylene, and mounted.

Immunofluorescence

Immunofluorescent staining of mammary epithelial cells was performed in a manner similar to the methodology

described by Wozniak and co-workers [25]. Briefly, collagen gels were fixed in 4% paraformaldehyde for 20 minutes at room temperature. Following three washes in PBS, paraformaldehyde fluorescence was quenched with 0.15 M glycine in PBS then the gels were washed with PBS. Triton-X (0.2%) was added to permeabalize the cells, and gels blocked overnight with 2.5% fatty acid-free bovine serum albumin (BSA) + 1% donkey serum. Cell proliferation was then examined by staining with the anti-Ki-67 (mouse clone 7B11; Zymed) primary antibody in PBS containing 1% donkey serum for 30 minutes at room temperature. Following five 10-minute washes in PBS, gels were incubated with anti-mouse tetramethylrhodamine isothiocyanate (TRITC; Jackson ImmunoResearch Laboratories) secondary antibody, phalloidin-fluorescein isothiocyanate (FITC; Jackson ImmunoResearch Laboratories), and bisbenzimide (Sigma-Aldrich) in PBS containing 1% donkey serum for 30 minutes at room temperature. Gels were again washed with PBS and mounted with Prolong Antifade mounting media (Molecular Probes). Imaging was performed on a TE300 Nikon epifluorescence inverted microscope with acquired z-stacks deconvolved using Slidebook imaging software (Olympus).

Lung metastasis

Lungs from PyVT/wt (*n* = 4) and PyVT/Col1a1 (*n* = 4) mice (as well as wt/wt and wt/Col1a1 as negative controls) were harvested at 15 weeks, fixed in formalin, and processed for histology. Sections were cut every 50 μm through the entire tissue and sections stained with H&E. Total lung metastases over all sections were then counted.

Three-dimensional invasion assay

Uniform sized tumor explants were harvested from intact tumors using a tissue biopsy punch (3 mm diameter), rinsed with PBS (containing 100 units penicillin, 100 μg streptomycin, and 0.25 μg/ml amphotericin B), and placed into 2.0 mg/ml collagen gels (BD Biosciences, San Diego, CA) that were neutralized with 2× HEPES buffer. Tumors were maintained in collagen gels floated in Dulbecco's Modified Eagle's Medium (DMEM) containing 5% fetal bovine serum (FBS), penicillin (100 units), streptomycin (100 μg), and amphotericin B (0.25 μg/ml) for 10 days over which time the number of distant multicellular colonies were counted.

Isolation of tumor cells and migration assay

Tumors from PyVT/wt and PyVT/Col1a1 backgrounds were minced and digested with 2 mg/ml collagenase and 10 μg/ml hyaluronidase in DMEM containing penicillin (100 units), streptomycin (100 μg), and amphotericin B (0.25 μg/ml). Following gentle shaking at 37°C for 3 hours, cells were pelleted, washed, and plated in DMEM containing 5% FBS. Thirty-six hours post-harvest the

tumor cells were transferred to Transwell plates (Corning Inc, Corning, NY) using serum and soluble collagen containing media as the chemoattractant.

Multiphoton laser-scanning microscopy

For live tissue imaging by multiphoton excitation (MPE) and second harmonic generation (SHG), mammary tumors were harvested and live tissue maintained in buffered media at 37°C. All tissues were imaged immediately following tissue harvest using an Optical Workstation [27] that was constructed around a Nikon Eclipse TE300. A Tsunami Ti:sapphire laser driven by a Millenia 5 W pump laser (Spectra Physics, Mountain View, CA) excitation source producing around 100 fs pulse widths and tuned to 890 nm was utilized to generate both MPE and SHG. The beam was focused onto the sample with a Nikon 60X Plan Apo water-immersion lens (numerical aperture (NA) = 1.2). All SHG imaging was detected from the back-scattered SHG signal [28], and the presence of collagen confirmed in our tissues using fluorescence lifetime imaging microscopy (FLIM) on the same optical workstation, since the SHG from collagen has no lifetime. Furthermore, owing to the fundamentally different physical behavior of MPE and SHG, signals could be discriminated by filtering the emission signal. We used a 464 nm (cut-on) long pass filter to isolate the emission from autofluorescence from the conserved 445 nm SHG emission. A 445 nm (narrow-band pass) filter was therefore used to isolate the SHG emission. Acquisition was performed with WiscScan [29] a software acquisition package developed at LOCI (Laboratory for Optical and Computational Instrumentation, University of Wisconsin, Madison, WI) and image analysis for MPE/SHG was performed with ImageJ and VisBio [30] software. For TACS-1 image analysis, additional surface rendering plug-ins for ImageJ were utilized [31]. For TACS-2 and -3, ImageJ was used to quantify the collagen fiber angle relative to the tumor. The tumor boundary was defined and the angle relative to the tangent of tumor boundary was measured every 10 μm as reported previously [27].

Fluorescence and spectral lifetime imaging microscopy

FLIM was performed on live tissue with the optical workstation described above and as described previously [27]. Briefly, the Ti:sapphire laser (Millennium/Tsunami, Spectra-Physics, Mountain View, CA) was tuned to 890 nm with the beam focused onto the sample with a Nikon 60X Plan Apo water-immersion lens (NA = 1.2). Intensity and FLIM data were collected by a H7422 GaAsP photon-counting photomultiplier tube (PMT; Hamamatsu, Bridgewater, NJ) connected to a time-correlated single photon counting (TCSPC) system (SPC-730, Becker & Hickl, Berlin, Germany). Multiphoton spectral lifetime imaging microscopy (SLIM) was performed using a second-generation system that evolved from a previously

described instrument [32] built around an inverted micro-scope (Eclipse TE2000, Nikon, Melville, NY). Briefly, a Mira Ti:sapphire mode-locking laser driven by a Verdi 8 W laser (Coherent Mira, Coherent, Santa Clara, CA) was used to generate pulse widths of approximately 120 fs at a repetition rate of 76 MHz. Intensity and fluorescence life-time data were collected over 16 individual 10 nm spec-tral-width channels using a 16-anode photon counting linear PMT array (PML-16, Becker & Hickl) connected to a TCSPC system (SPC-830, Becker&Hickl). Fluorescent life-time analysis from FLIM and SLIM was carried out with SPCImage (Becker & Hickl) as well as with a LOCI created computational tool, SlimPlotter [33], which allows visu-alization and analysis of the lifetimes by spectral channel.

Statistical analysis
For multi-group comparisons, one-way analysis of vari-ance (ANOVA) with a *post-hoc* Tukey-Kramer test was used. We performed *t*-testing for two-group comparisons.

Results
Increased collagen density promotes mammary epithelial cell proliferation in reconstituted three-dimensional matrices
To test the hypothesis that increased collagen density can directly promote growth of mammary epithelial cells in the absence of stromal cells, human MCF10A cells were cultured within three-dimensional collagen gels and pro-liferation was measured (Figure 1). Cells cultured within low-density matrices form well-differentiated acini struc-tures, while colonies that formed within high-density matrices are larger, less-organized structures (Figure 1a). In agreement with the formation of larger colonies, prolif-eration of human mammary epithelial cells is increased in high-density matrices (Figure 1b), indicating that increas-

ing collagen matrix density can directly promote epithe-lial cell proliferation.

Increased tumor incidence in collagen-dense mammary tissues
In order to develop a murine tumor model possessing col-lagen-dense mammary tissue, we examined the mammary tissues from Col1a1[tmJae] transgenic mice (Figure 2a). These mice carry mutations near the highly conserved matrix metalloproteinase (MMP) cleavage site for type I collagen (between Gly_{775} and Ile_{776} of the $\alpha1(I)$ chain) that make the collagen resistant to human collagenase digestion [26]. Although an additional cleavage site on type I collagen is vulnerable to rodent collagenase (often termed rat collagenase) and the collagen is susceptible to other proteases [26], these are not sufficient to achieve the proper balance of collagen synthesis and degradation, resulting in excessive collagen accumulation in the skin, uterus, and bone [26]. These phenotypes raised the possi-bility that the mammary gland, which undergoes dynamic changes in collagen deposition and degradation during development, puberty, and estrous, would rapidly accu-mulate excess stromal collagen. To explore this possibil-ity, we previously analyzed mammary glands from wild-type, heterozygous, and homozygous Col1a1[tmJae] mice. Using techniques specific for collagen detection, we reported a greater than 2.5-fold increase in stromal colla-gen associated with heterozygous or homozygous mice when compared with wild-type mice [27] (Figure 2a).

With a defined model for breast tissue density in place, we set out to test the hypothesis that increased mammary col-lagen density increases tumor formation. Mammary tumors were initiated with the PyVT transgene. This breast tumor model correlates well with many features of human
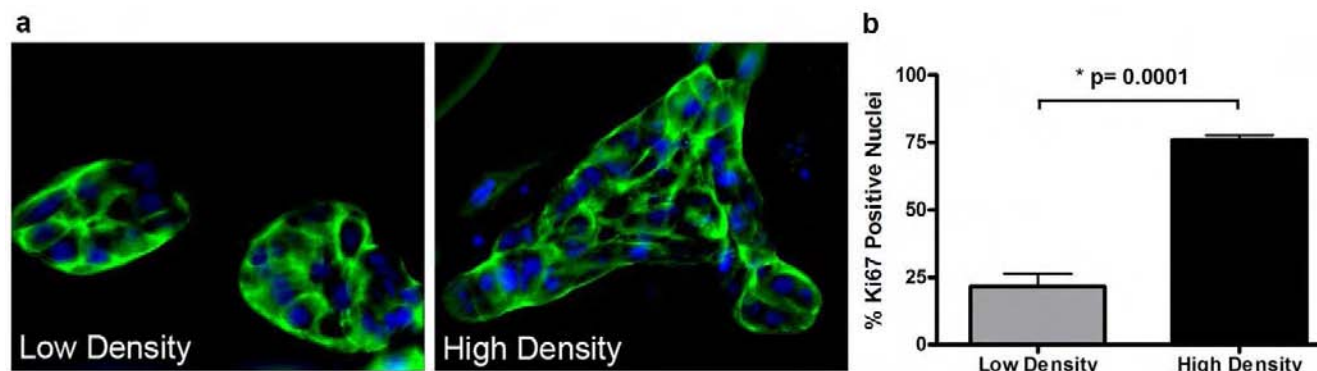
Figure 1
Increased collagen matrix density directly promotes epithelial cell proliferation. **(a)** Actin staining to visualize MCF10A human mammary epithelial cells cultured within low (1.3 mg/ml) and high-density (3.0 mg/ml) collagen gels for 21 days (actin, green; nuclei, blue). Left: Two well-differentiated acini structures formed in low-density matrices. Right: A single, less-organized colony. **(b)** Increased proliferation of mammary epithelial cells cultured within high-density matrices, measured by increased detection of the Ki67 antigen, a marker of proliferation.
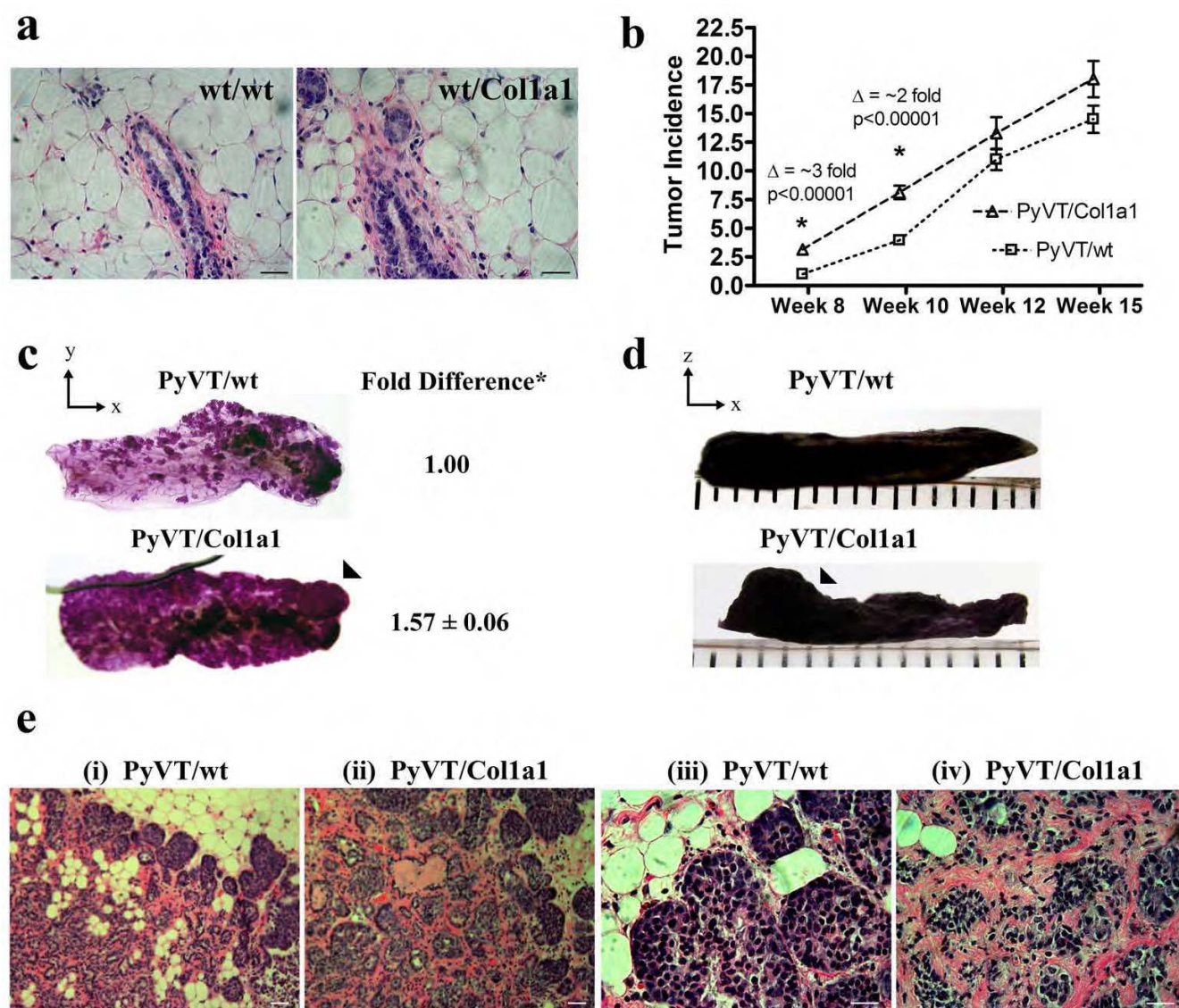
Figure 2

High mammary collagen density promotes tumor formation. **(a)** Histology of mammary glands from 10-week-old wild-type and heterozygous Col1a1tmJae mice showing increased stromal collagen and hypercellularity associated with the Col1a1tmJae mouse model. Scale bar 25 μm. **(b)** Significantly increased tumor numbers per mouse in collagen-dense (Col1a1) mammary glands. **(c)** Whole mount preparations of the fourth inguinal mammary glands from PyVT/wt and PyVT/Col1a1 mice at 10 weeks of age. Quantitative analysis of the area of hyperplasia from three pairs of glands calculated from a common threshold value set with density slicing in ImageJ software revealed a greater than 1.5-fold increase in hyperplasia associated with increased stromal collagen (*t*-test: *p* = 0.03). In addition, at age-matched time points, tumors in mice with dense stroma not only displayed more hyperplastic area but also tumor regions that grew out away from the gland (arrows in (c) and (d)). **(e)** Low (*i*), (*ii*) and high (*iii*), (*iv*) magnification images of H&E stained histology sections from 10-week-old mice showing increased collagen in PyVT/Col1a1 tumors ((*ii*) and (*iv*)) and a more invasive phenotype when compared with PyVT/wt (*i*) and (*iii*) tumors. Scale bars 50 μm in (*i*) and (*ii*) and 25 μm in (*iii*) and (*iv*).

cancer, progresses from hyperplasia to adenoma to early and late carcinoma [34], and is reliably invasive and metastatic [34]. When mice carrying the PyVT transgene under the control of the mammary epithelial-specific MMTV promoter were crossed with heterozygous Col1a1tmJae

mice, we observed an approximately three-fold increase in early tumor formation in collagen-dense tissues (that is, a three-fold greater number of tumors per mouse; see Figure 2b). This trend of increased tumor incidence in collagen-dense glands continued through week 15 (Figure 2b), and

two additional PyVT/Col1a1 mice needed to be euthanized by week 13 due to excessive tumor burden (not shown). Consistent with these observations, quantitative analysis of whole mounts of the fourth mammary gland (*n* = 3 pairs) show significantly increased areas of hyperplasia (Figure 2c) with collagen-dense tissues showing increased cell growth out from the gland (Figure 2c *arrowhead* and Figure 2d). Furthermore, tumors progressing in collagen-dense tissues at 10 weeks had a more invasive morphology (Figure 2e). Of note is the fact that tumors arising in collagen-dense mammary tissue retain increased collagen density (Figure 2e and confirmed with collagen selective picrosirius red staining (not shown)). In fact, collagen levels in PyVT/Col1a1 tumor-bearing glands appear to be increased relative to non-tumor bearing collagen-dense glands (Figure 2e). This observation possibly indicates an amplified shift in the imbalance between collagen synthesis and degradation in the Col1a1 mice following tumor initiation, and may represent an increased desmoplastic response.

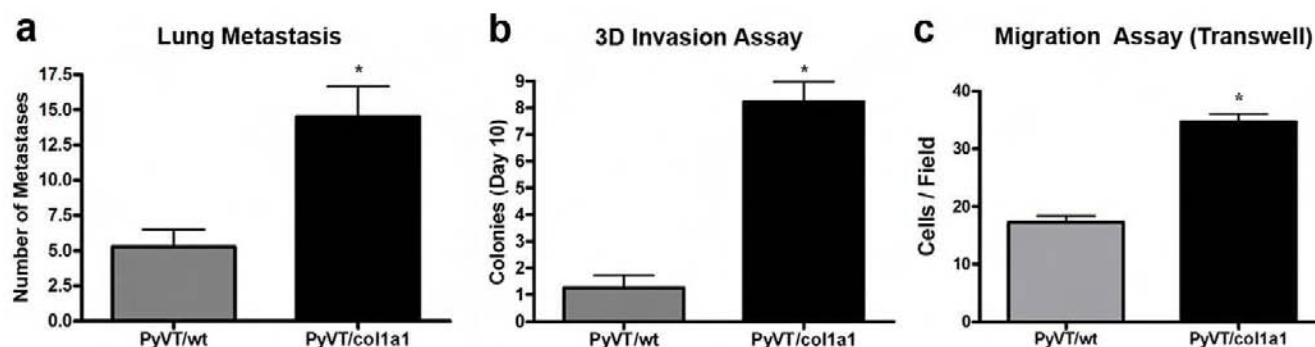### Increased invasion and metastasis associated with dense stromal collagen

Examination of later-stage tumors (week 15) demonstrated that both PyVT/wt and PyVT/Col1a1 tumors were invasive (data not shown), confirming an earlier report that late-stage wild-type PyVT tumors have invasiveness associated with collagen reorganization [27]. Moreover, since the MMTV-PyVT tumor model reliably results in lung metastases, we examined lung tissue in late-stage mice (week 15). In animals in which tumors were initiated and progressed in a collagen-dense microenviron-

ment, a significant increase in the number of lung metastases was observed (Figure 3a). This raised the possibility that increased lung metastasis may be the result of a more-invasive and migratory cell population, or may result from the earlier onset of invasiveness. To address this question, we isolated tumor plugs and tumor cells and performed invasion and migration assays, respectively.

Data showing increased invasion in tumors that arose in collagen-dense tissue was obtained by quantifying invasion from tumor explants into three-dimensional collagen gels. To determine whether local invasion was a simple reflection of increased local collagen that facilitates invasion or also due to an intrinsic property of tumor cells arising in a collagen-dense stroma, tumor explants of defined size were placed into three-dimensional collagen gels and the number of distant colonies was counted. After 10 days in culture, explants from collagen-dense tissues resulted in significantly more colonies (Figure 3b). Furthermore, tumor cells isolated from collagen-dense tissues were in fact more migratory (Figure 3c), indicating that the earlier onset of invasiveness is likely not the sole cause for increased metastasis but that the tumor cells themselves are more invasive (Figure 3b) and migratory (Figure 3c).

Changes in the tumor-stromal interaction associated with increased stromal collagen

Collagen content, fiber structure, and organization are potentially key determinants of tumor cell behavior [27,35]. Therefore, to better understand the reported
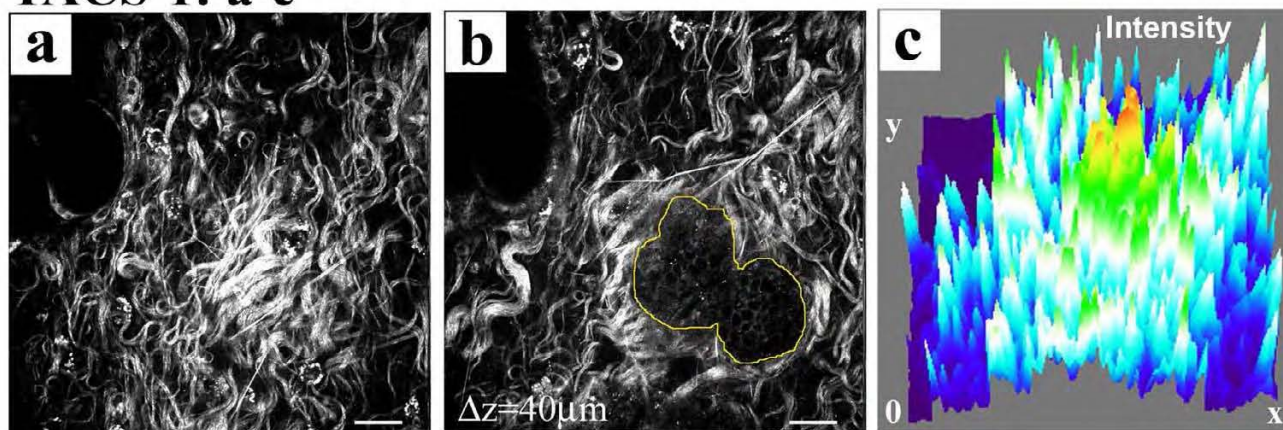

Figure 3
Increased metastasis associated with dense stromal collagen. **(a)** Increased number of lung metastases per lung at 15 weeks in mice that formed tumors in collagen-dense mammary glands (PyVT/Col1a1) when compared with mice that formed tumors in control glands (PyVT/wt; mean ± standard error of the mean (SEM), *n* = 4 of each genotype). **(b)** Three-dimensional tumor cell invasion assay showing that tumor explants from collagen-dense tumors (PyVT/Col1a1) resulted in more invasion into three-dimensional collagen gels and colony formation after 10 days than explants from PyVT/wt tumors (mean ± SEM; *n* = 4 PyVT/wt and *n* = 14 PyVT/Col1a1 tumor explants from four sibling mice). **(c)** Tumor cells extracted from collagen-dense tumors (PyVT/Col1a1) showed increased migration when compared to tumor cells from control tumors (PyVT/wt) as measured by transwell migration assays with serum as the chemoattractant (mean ± SEM; *n* ≥ 3 independent experiments). *Indicates a statistically significant difference (*p* < 0.05) following analysis with *t*-tests.

increase in invasion and metastasis associated with increased collagen density, we employed nonlinear optical imaging of tumor-stromal interactions in intact live tumors. Multiphoton laser-scanning microscopy (MPLSM) was used to simultaneously generate intrinsic signals from cellular autofluorescence by MPE and fibrillar collagen by SHG [27,36-38]. Using this approach we previously defined [27] three Tumor-Associated Collagen Signatures (TACS; Figure 4) in mammary tumors from both Wnt-1 and PyVT transgenic mice. Specifically: TACS-1, the presence of locally dense collagen (Figure 4a)

within the globally increased collagen concentration surrounding tumors, indicated by increased signal intensity (Figure 4c) at a region near the tumor, which serves as a reliable hallmark for locating small tumor regions (Figure 4b); TACS-2, straightened (taut) collagen fibers stretched around the tumor, constraining the tumor volume (Figure 4d and 4e); and TACS-3, identification of radially aligned collagen fibers that facilitate local invasion (Figure 4f). With TACS-3, a distribution of collagen fiber angles around 90° relative to the tumor boundary was indicative of high levels of local invasion while a distribution
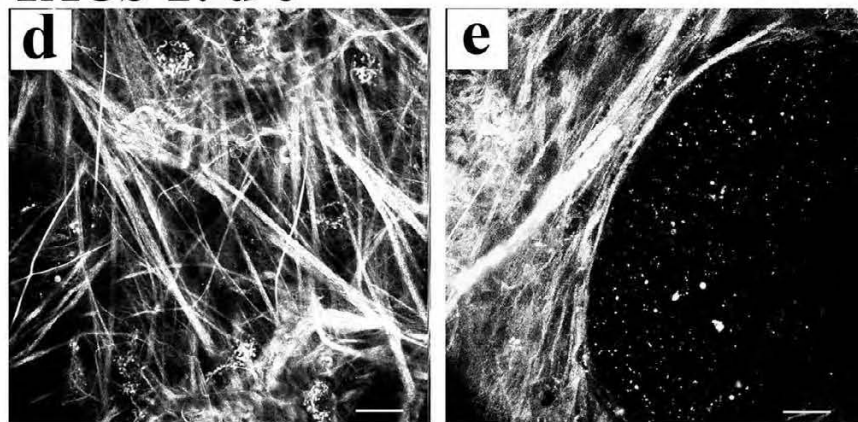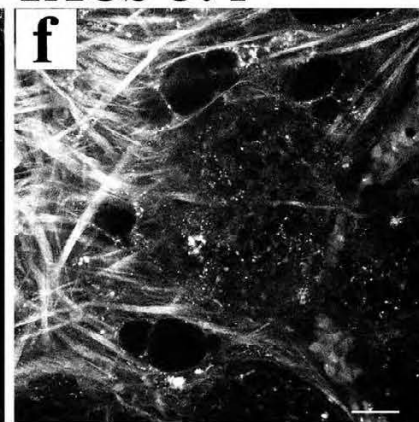

Figure 4
Tumor-associated collagen signatures. **(a)-(c)** Example of TACS-1. A region of locally dense collagen **(a)** near (40 μm 'above') a small tumor region **(b)** that is within the globally increased collagen region surrounding tumors, resulting from increased SHG (collagen) signal intensity; **(c)** three-dimensional surface plot of intensity showing an approximately three-fold signal increase at TACS-1. **(d)**, **(e)** Example of TACS-2, showing straightened (taut) collagen fibers stretched around and constraining an expanded epithelial tumor volume. At regions of TACS-2, quantitative analysis [27] of fiber angles relative to the tumor boundary shows a distribution of fibers around 0° that correlates to non-invading regions of tumor cells. **(f)** Example of TACS-3, showing radially aligned collagen fibers, reorganized by tumor cells, at regions of tumor cell invasion. At regions of TACS-3, quantitative analysis [27] of fiber angles relative to the tumor boundary shows a distribution of fibers around 90° that correlates with local invasion of tumor cells.

around 0° was associated with non-invading regions of the tumor [27].

In comparing tumors in the wild-type and heterozygous Col1a1[tmJae] backgrounds carrying the MMTV-PyVT transgene, we identified critical differences in the temporal progression in density-associated tumors (Figure 5). At 8 weeks of age, TACS-1 formation in wild-type tumors (Figure 5a) was not yet well developed, and tumors were primarily non-invasive with collagen fibers distributed around 0° (Figure 5b and 5c). In contrast, collagen-dense tumors (PyVT/Col1a1) displayed more developed TACS-1 with increased collagen signal and more straightened fibers, indicating early progression to TACS-2 (Figure 5a) and some regions of TACS-3 (Figures 5b and 5c). Dense tissues (PyVT/Col1a1) began to show regions of local invasion at 8 weeks (Figure 5b-ii; highlighted with and arrowhead) corresponding to an increased frequency of reorganized collagen fibers with a peak realignment near 90° (Figure 5c). By 10 weeks of age this difference was enhanced. While tumors from PyVT/wt animals were still largely non-invasive, tumors that arose in collagen-dense tissues continued to have more collagen signal, enhanced realignment to TACS-3, and increased local invasion (Figures 5b and 5c), supporting histological findings shown in Figure 2e. Moreover, this shift in the temporal onset of TACS-3 to an earlier occurrence in collagen-dense tumors indicates the more advanced and invasive state of these tumors.

Spectral-lifetime imaging of the tumor-stromal interaction suggests a metabolic signature associated with invasion

In concert with changes in the alignment of stromal collagen and increased local invasion, higher cellular autofluorescence intensity was observed in stromal cells and invading tumor cells when compared with cells in the primary tumor mass (Figures 5 and 6). To examine these progression-associated changes in more detail, we imaged the tumors with multiphoton FLIM and SLIM [32,33,39]. Using SLIM, the peak cellular emission was detected at 530 nm. Hence, the spectral properties, or 'fingerprint', of the endogenous cellular fluorophore identified it as flavin adenine dinucleotide (FAD), and not nicotinamide adenine dinucleotide (NADH) or tryptophan [40], and confirmed the presence of collagen (Figure 6a and Additional file 1), which has a theoretical zero fluorescence lifetime that is experimentally equal to the system signal response due to background noise (that is, 100 ns (blue) in Figure 6b).

Exploiting cellular FAD as an endogenous biomarker to visualize cells, we further explored the difference in FAD signal between stromal and tumor cells, using FLIM. Differences in the fluorescence lifetime of FAD between primary tumor cells and stromal cells were color mapped (Figure 6b) and quantified (Figure 6c). Stromal cells possessed a higher second component (τ_2) and weighted mean (τ_m) of the fluorescent lifetime, allowing stromal cells to be easily differentiated from epithelial tumor cells (Figure 6b and 6c).

Interestingly, invading cells displayed a fluorescent intensity more closely resembling stromal cells than cells from the primary tumor mass (Figure 7a and 7b). Consistent with this finding, changes in fluorescent intensity and fluorescent lifetimes of NADH and tryptophan have also been associated with cells of differing metastatic potential [41]. Because invading tumor cells commonly de-differentiate, it is possible that shifts in the fluorescent lifetime may be indicative of fundamental changes in cells associated with invasion and metastasis. In fact, a metabolic signature of higher FAD fluorescent intensity was observed in cells near invading regions when compared with non-invading regions (Figure 7a) while invading tumor cells showed a longer FAD fluorescent lifetime (the right panel in Figure 7b), having higher first (τ_1), second (τ_2), and weighted mean (τ_m) lifetime components (Figure 7c), and could be differentiated from stromal cells and cells in the primary tumor mass. Furthermore, examination of τ_2 values indicates a progressive increase in lifetimes from cells within the tumor mass to invading cells to stromal cells (Figure 7d) supporting the idea of a fundamental change to invading cancer cells.

In addition to identifying key differences in measurable fluorescent intensity and lifetime associated with invading cells, FLIM analysis confirmed results shown in Figure 4 demonstrating a shift towards TACS-3 and increased local invasion with higher collagen density (see Figure 7b). Invading cells associated with TACS-3 could be clearly differentiated in collagen-dense tissues (the right panel in Figure 7b) while PyVT/wt tumors (the left panel in Figure 7b) were not highly invasive at this stage (week 10).

Discussion
Collagen density and tumor formation and progression

Although the increased risk for breast carcinoma associated with collagen-dense breast tissue has been described [1-3], a causal link between increased stromal collagen and increased breast carcinoma has not been previously established. Moreover, little is known about the molecular mechanisms underlying increased collagen deposition and its influence on the interactions between stromal collagen, fibroblasts, and epithelial cells, or how increased collagen affects tumorigenesis and tumor cell phenotype. This is due in large part to the fact that no animal model system had previously existed to study these phenomena *in vivo*. Herein we demonstrate that mice with increased stromal collagen have increased mammary tumors that
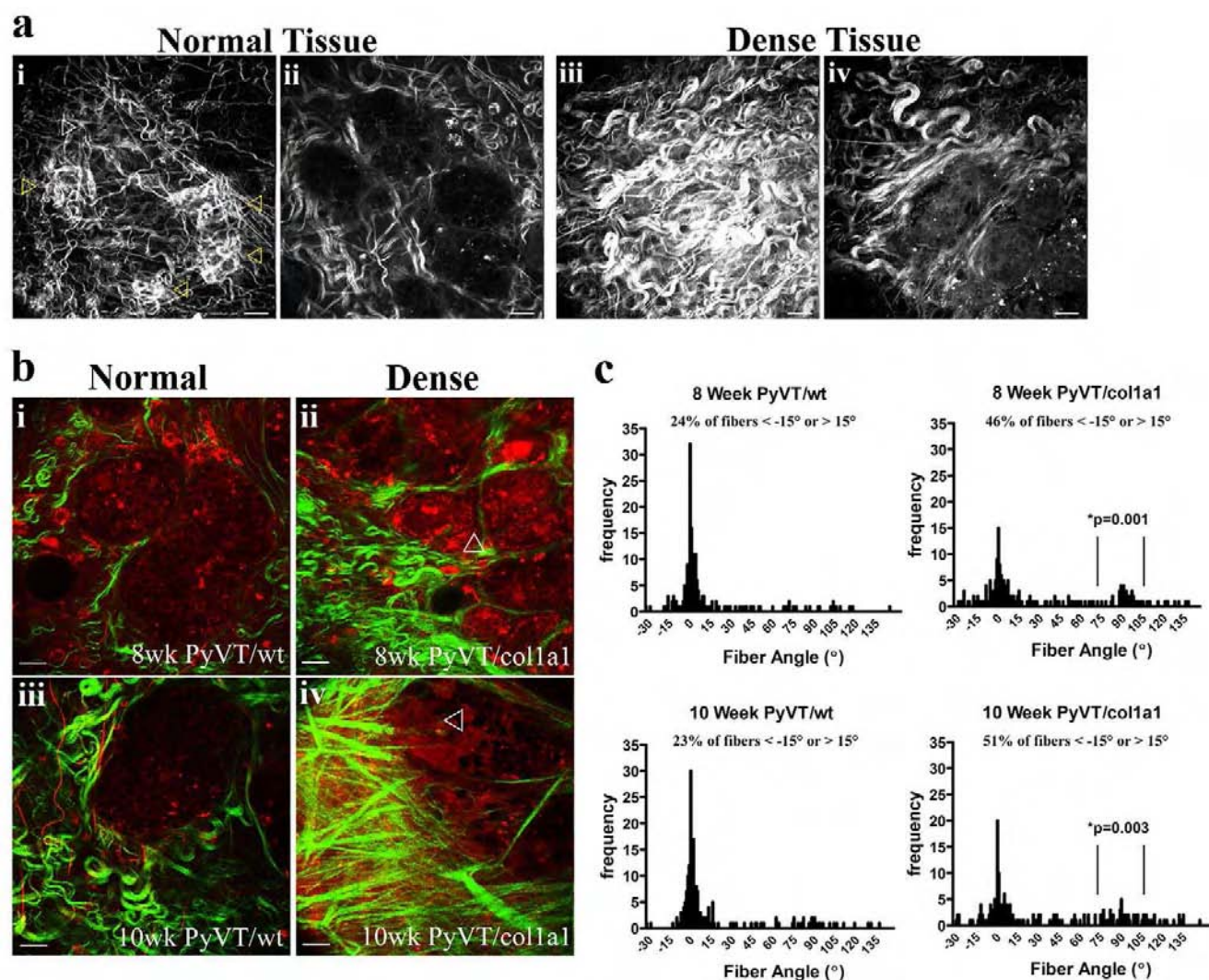
Figure 5
Increased progression of tumor-associated collagen signatures and increased local invasion with high collagen density. **(a)** TACS-1 in 8-week-old normal (wild-type; (*i*), (*ii*)) and collagen-dense (col1a1; (*iii*), (*iv*)) tumors showing more developed TACS-1 associated with density (early transition between TACS-1 and -2) while showing very early TACS-1 formation in wild-type tumors (shown with yellow arrowheads; white arrowhead indicates a TACS-1 region that is not shown since it is out of the focal plane). The displayed tumor regions ((*ii*) and (*iv*)) are at a $\Delta z = 40$ μm from collagen signatures ((*i*) and (*iii*)). Note the increased endogenous cellular autofluorescence associated with tumor cells in collagen-dense tissues when PyVT/wt (*ii*) and PyVT/Col1a1 (*iv*) tumors were imaged sequentially at the same power settings ((*ii*) versus (*iv*)). Representative of *n* = 4 pairs of tumors. **(b)** Tumors were imaged and MPE (pseudo-colored red) and SHG (pseudo-colored green) signals were separated. At 8 weeks tumors showed early TACS-3 regions and some local invasion in collagen-dense tumors (*ii*) while PyVT/wt tumors (*i*) were still primarily bound by collagen (TACS-2) and non-invasive. At 10 weeks, tumors from dense tissues (*iv*) displayed further regions of TACS-3 progression and an invasive phenotype, compared to control tissues (*iii*) that were largely non-invasive and had little collagen reorganization. Representative of *n* ≥ 6 tumors from each background. **(c)** Quantitative analysis of collagen fiber angles relative to the tumor boundary for 8-week (*top*) and 10-week (*bottom*) old animals. PyVT/wt animals displayed little TACS-3 and are primarily non-invasive with only 23% (8 weeks) and 24% (10 weeks) of their fibrils having angles outside of the TACS-2 distribution around 0° (that is less than -15° or more than 15°). In contrast PyVT/Col1a1 tumors were more invasive, possessing a broader fiber distribution and some regions of TACS-3 (distribution around 90°), with 46% and 51% of the fibrils distributed outside of the TACS-2 distribution (0°) at 8 weeks and 10 weeks, respectively (*indicates that the number of events associated with TACS-3/invasion (75° to 105°) was significantly greater). Calculated from at least 185 of tumor regions from at least 6 separate tumors. All scale bars are 25 μm.
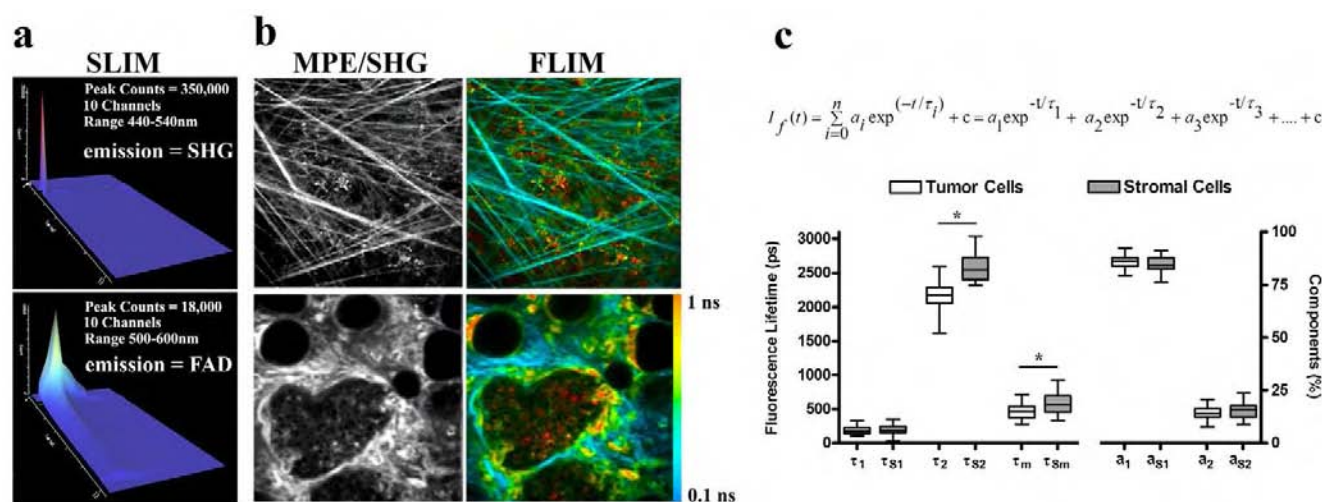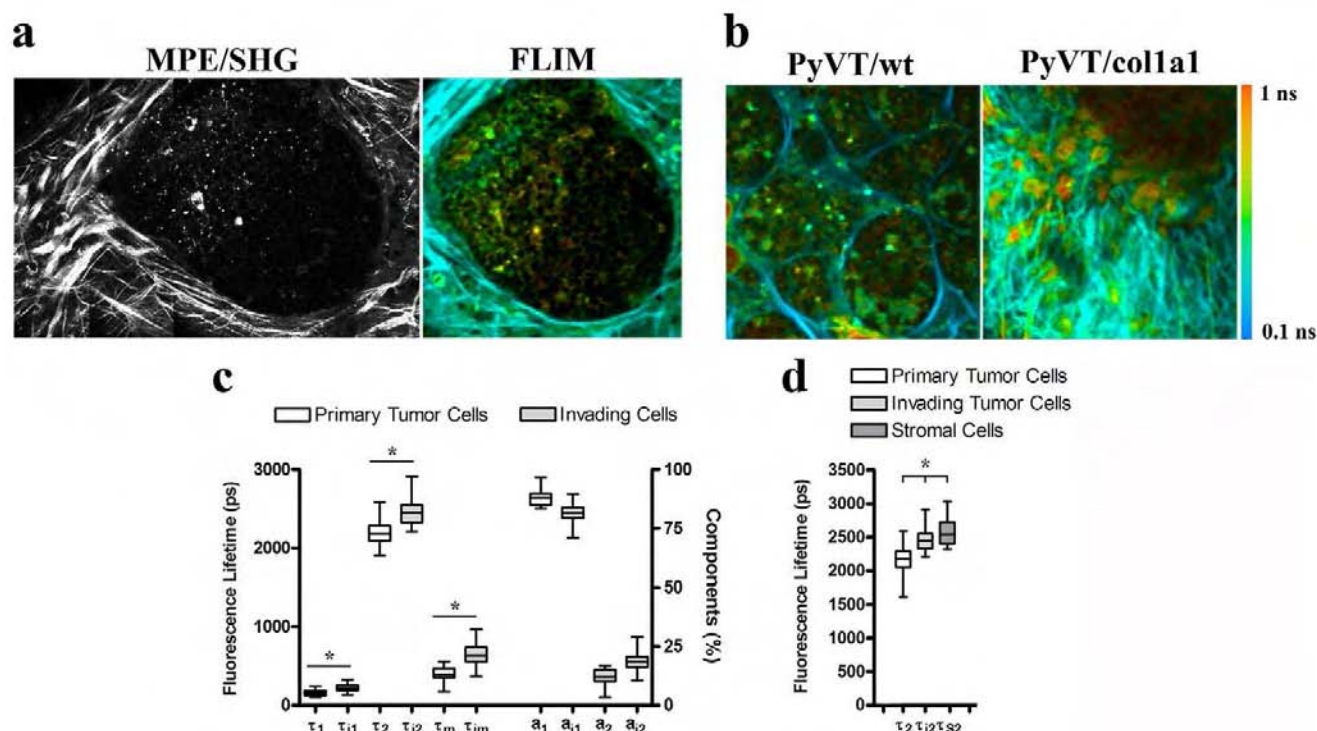
Figure 6
FLIM an SLIM analysis of mammary tumors. **(a)** Multiphoton spectral lifetime imaging microscopy (SLIM) analysis of the emission spectrum from endogenous fluorescence resulting from excitation at 890 nm. The emission signals were separated by 10 nm spectral steps over 16 channels (10 channels are displayed) and the photons collected in each channel used to generate fluorescence lifetime images and signals for each channel plotted with SLIM-Plotter (shown). Emission from collagen (at half of the input wavelength) showed a very strong and sharp signal with a no appreciable decay (lifetime) confirming the SHG nature of the collagen signal (top). Emission spectra of endogenous fluorescence from tumor and stromal cells showed that the only substantial emission signal is at 530 nm, indicating that the source of the autofluorescence signal is FAD, with lifetime values from the 530 channel matching values obtained with fluorescence lifetime imaging microscopy (FLIM). **(b)** Multiphoton intensity and FLIM images of the stroma near a tumor (top) and the tumor and stromal components (bottom) from wild-type tumors showing the utility of FLIM to image tumor cells, stromal cells, and extracellular matrix components. Note the increased intensity and fluorescent lifetimes of stromal cells (quantified in (c)) and the low lifetime of collagen (matching system response, that is, no actual lifetime/color mapping toward blue). The color map in (b) represents the weighted average of the two-term model components ($\tau_m = (a_1\tau_1 + a_2\tau_2)/(a_1 + a_2)$) using the equation shown in (c). **(c)** Quantitative analysis of fluorescent lifetime components from tumor and stromal (subscript s) cells using the equation shown. Note the increase in the second (long) component and weighted mean component (see the equation above) for stromal cells when compared with cells from the primary tumor mass. Note that at least 30 measurements per tumor image from 4 independent tumors were used to calculate lifetime values for tumor cells in the primary tumor mass while at least 6 measurements per tumor image from 4 independent tumors were used for stromal cells. *Indicates a statistically significant ($p < 0.05$) difference following analysis with one-way analysis of variance (ANOVA) with a *post-hoc* Tukey-Kramer test.

are more invasive and metastatic, and thus provide a causal link between stromal density and carcinoma progression, consistent with reports of human breast carcinoma risk.

In this system, increased collagen density is the initial event, promoting tumor initiation and metastasis. This may be the result of two likely mechanisms (Figure 8), both of which follow the increase in collagen density (that is, increasing collagen is the initial event in our system). The first mechanism is that increased breast density is associated with a stiffer extracellular matrix resulting in high local mechanical loads and higher resistance to cellular contractility for breast epithelial cells. Such changes in the physical microenvironment has been shown to alter focal adhesion and Rho GTPase signaling, resulting in increased proliferation and a more transformed pheno-

type [24,25]. A second, and more indirect mechanism, may be the influence of increased stromal collagen on mammary fibroblasts that in turn influence epithelial cells. Stromal fibroblasts can regulate epithelial cells in part through secretion of specific soluble growth factors and chemokines [20,42-44]. For instance, TGF-β has been associated with reactive stroma, fibrosis, and epithelial cell invasion [45], while numerous studies indicate that the epidermal growth factor (for example, EGFR, HER-2/neu/ErbB2, ErbB3, and so on), insulin-like growth factor (for example, IGF-I, IGFBP3, and so on), and hepatocyte growth/scatter factor (HGF/SF, c-Met) systems are important not only in the normal mammary gland but also during tumorigenesis and metastasis [44,46-49]. Furthermore, the IGF family has been implicated in association with dense breast tissue [14,50,51] with both local [14] and circulating [50,51] levels of IGF-I positively cor-

Figure 7
Fluorescence lifetime imaging microscopy analysis of invading tumor cells. **(a)** Intensity and fluorescence lifetime imaging microscopy (FLIM) images of cells away from and near invasive TACS-3 regions showing increased fluorescent intensity and lifetime near invasive regions (left side of images). **(b)** FLIM images of tumors from 10-week-old PyVT/wt and PyVT/Col1a1 animals confirming the increased TACS-3 for collagen-dense tumors shown in Figure 5. **(c)** Increased fluorescent lifetimes for invading cells. Like stromal cells the second (long) and mean components are increased in invading cells. However, the short component is also increased in invading cells when compared to cells in the primary tumor mass. Note, 45 measurements for cells within the primary tumor mass and 45 measurements for invading cells adjacent to the tumor primary tumor mass were used to calculate lifetime values. **(d)** The second (long) component from cells within the primary tumor mass, invading tumor cells, and stromal cells showing a progressive increase as cells move from a primary epithelial tumor phenotype to a more migratory phenotype. *Indicates a statistically significant ($p < 0.05$) difference following analysis with one-way analysis of variance (ANOVA) with a *post-hoc* Tukey-Kramer test.

related with breast tissue density. In fact, both of these mechanisms are plausible and are likely to be acting in concert with one another to produce fundamental changes in both the breast epithelial and stromal cells. Since both adhesion-mediated and growth factor-mediated signaling pathways are often interrelated [52-57], understanding each of these possible mechanisms and their convergence is likely to be of great importance to understanding breast tissue density-related carcinoma.

However, the possibility that altered matrix remodeling associated with the Col1a1 model is playing a role also warrants consideration. However, in theory, a significant defect in matrix remodeling should inhibit tumor progression, and the fraction of collagen that is collagenase-resistant can be degraded/remodeled at a second site by the rodent collagenase and other proteases that are expressed by tumor and tumor-associated cells. Hence, while limitations of the model must be taken into account when considering the presented data, it appears unlikely that a defect in matrix remodeling associated with the use of the Col1a1 model is causal for the increases in tumor formation and progression observed in this study.

Collagen signatures and local invasion
In a previous study we described the use of collagen alignment to quantify local invasion with the level of TACS-2 (alignment tangential to the tumor boundary at a 0° angle) and TACS-3 (alignment radial to the tumor boundary at an angle of 90°) providing a novel quantitative assessment of tumor progression [27]. In this study, the analysis of collagen radial alignment in samples from 8- and 10-week tumors demonstrates a transition from TACS-2 to TACS-3. We observe a broad distribution of
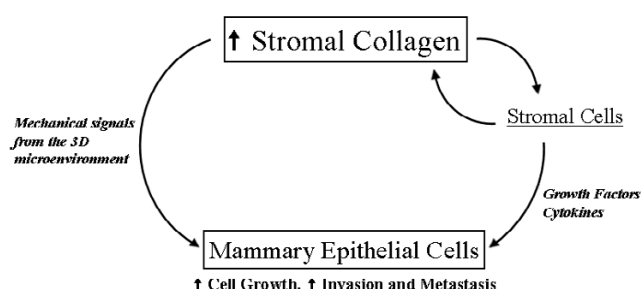
Figure 8
Model for advancement of mammary epithelial tumors by increased stromal collagen. Increased fibrillar collagen in the mammary stroma directly regulates the three-dimensional mechanical microenvironment of mammary epithelial cells, influencing proliferation and phenotype. In addition, increased collagen advances a feed-forward loop with fibroblasts to promote additional collagen deposition and an increased stromal/fibroblast population resulting in increased paracrine signaling to mammary epithelial cells. The net result is increased epithelial proliferation/tumor formation and a more invasive and metastatic phenotype.

fiber angles away from zero but not yet tightly grouped as late-stage tumor at the radial alignment (90°) associated with the high degree of local invasion previously reported for 15-week tumors [27]. This result suggests that the move toward invasive behavior is a transitional process increasing with time. We find that tumor cells in collagen-dense tumors are not only more invasive and metastatic *in vivo*, but were also more invasive and migratory *in vitro* (Figure 3b and 3c), indicating that the increased invasiveness is not only the result of earlier tumorigenesis that had more time to progress, but also due to tumor cells that are fundamentally more invasive because they arose within collagen-dense tissues. This finding suggests that cellular behavior is altered by epigenetic changes signaled from the collagen-dense stroma, consistent with findings that increased collagen density alters epithelial cell signaling and behavior *in vitro* [25].

FAD and local invasion

Interestingly, we measured an increase in the fluorescence lifetime for the metabolite FAD associated with invading cells. While this information provides a valuable biomarker for use with an optical biopsy, the biological relevance of this finding is not well understood. It is known that transformed cells often undergo increased glycolysis in the cytosol, a phenomena known as the Warburg effect [58], and that the fluorescent lifetimes of NADH and FAD, and in particular the redox ratio of these two metabolites, is altered in transformed cells [59]. Of interest, Skala and co-workers [59] recently reported an increase in the τ_1 component of the FAD lifetime in precancerous cells

when compared with normal epithelium. In the current study we compare non-invasive transformed cells with invading cells, and as such we speculate that the alteration in FAD state seen in transformation may become increasingly mis-regulated in the more metastatic population of transformed cells. Furthermore, the biological implications of the increased FAD intensity and fluorescent lifetime may be found in the possibility that increased glycolysis is increasing levels of NADH, a known regulator of transcription [60], and resulting in more lactic acid production [61] with less pyruvate entering into the citric acid cycle and, as a consequence, less FAD being reduced to $FADH_2$. Moreover, it has also been reported that the fluorescence lifetime of FAD can decrease due to quenching from NAD+, other molecular interactions, or environmental conditions [62,63], and thus the increased fluorescence lifetime of FAD could also be indicative of less available NAD+, particularly in the cytosol, and other unknown changes in FAD binding and localization. Hence, the biological implications of altered FAD intensity and fluorescence lifetime remain elusive. However, our results provide evidence that changes in FAD signals can be found within a more invasive subpopulation of carcinoma cells and as such understanding the regulatory mechanisms associated with these observations may provide great insight into tumor cell metastasis.

Conclusion

In summary, increased collagen density increases tumorigenesis, local invasion, and metastasis, causally linking increased stromal collagen to tumor formation and progression. Imaging with combined MPE and SHG in tumors allows visualization of cellular autofluorescence and defined collagen structures that identify key differences associated with high collagen density and may provide useful diagnostic tools to rapidly assess fresh tissue biopsies. Furthermore, imaging live tissues with FLIM and SLIM confirms results obtained with MPE/SHG and identifies significant differences in fluorescence lifetimes that are indicative of invasive cells. Thus, FLIM and SLIM serve as powerful tools to evaluate the invasiveness of tumor cells in mammary tissues. Given the significant findings associated with high breast tissue density and the now available utility of a mouse model for breast tissue density, fundamental questions regarding the molecular mechanisms associated with breast tissue density-related carcinoma can now be further addressed *in vivo*.

List of abbreviations

ANOVA: analysis of variance; BSA, bovine serum albumin; DCIS: ductal carcinoma *in situ*; DMEM: Dulbecco/Vogt modified Eagle's minimal essential medium; H&E: hematoxylin and eosin; FAD: flavin adenine dinucleotide; FBS: fetal bovine serum; FITC: fluorescein isothiocyanate; FLIM: fluorescence lifetime imaging microscopy; MMP:

matrix metalloproteinase; MPLSM: multiphoton laser-scanning microscopy; MPE: multiphoton excitation; NA: numerical aperture; NADH: nicotinamide adenine dinucleotide; PBS: phosphate buffered saline; PCR: polymerase chain reaction; PMT: photomultiplier tube; PyVT: polyomavirus middle-T; SHG: second harmonic generation; SLIM: spectral-lifetime imaging microscopy; TACS: tumor-associated collagen signature; TCSPC: time-correlated single photon counting; TRITC: tetramethylrhodamine isothiocyanate.

Competing interests

The authors declare that they have no competing interests. Portions of the technologies presented in the manuscript are patented or patent pending. However, the authors have no interest, arrangement, or affiliation that could be perceived as a conflict of interest in the context of this manuscript.

Authors' contributions

PPP conducted all MPLSM, SHG, FLIM, and histology experiments, managed the mouse colonies and tumor studies, performed three-dimensional cell culture experiments, analyzed the imaging data, and prepared the manuscript and figures. DRI and JGK assisted with mice and tumor studies, and performed three-dimensional culture experiments. KWE and JGW assisted with specific technical aspects of nonlinear imaging and data analysis as well as project coordination. LY conducted SLIM imaging with PPP and assisted in data analysis. CTR contributed to the analysis of imaging data and the development of computational tools for SLIM analysis. PJK participated in the design and coordination of the project and assisted with data analysis. PPP, KWE, JGW, and PJK cooperatively designed the project and discussed data interpretation and analysis. All authors participated in critical editing of the manuscript.

Additional material

> ### Additional file 1
> *The multiphoton spectral lifetime imaging microscopy (SLIM) analysis of live tumors. Multiphoton fluorescence lifetime imaging microscopy (FLIM) demonstrates the measurable fluorescence lifetimes of live tumor cells as shown in Figures 6 and 7. Using SLIM, the fluorescence lifetimes following 890 nm two-photon excitation of live three-dimensional tumors are measured within a defined spectra, allowing identification of the emitting fluorophore and noise removal from adjacent spectra. For instance, examination of the 440–450 nm emission spectra from SLIM confirms the presence of collagen bounding tumor cells. For an 890 nm two-photon excitation the second harmonic generation (SHG) signal is maximal at 445 nm and has no lifetime (dark blue). In addition, the maximal emission signal from tumor cells is 535 nm as shown in Figure 6a, indicating the emission results from excitation of the endogenous fluorophore flavin adenine dinucleotide (FAD). Color bar 0 to 1 ns.*
> Click here for file
> [http://www.biomedcentral.com/content/supplementary/1741-7015-6-11-S1.pdf]

References

1. McCormack VA, dos Santos Silva I: **Breast density and parenchymal patterns as markers of breast cancer risk: a meta-analysis.** *Cancer Epidemiol Biomarkers Prev* 2006, **15:**1159-1169.
2. Boyd NF, Lockwood GA, Byng JW, Tritchler DL, Yaffe MJ: **Mammographic densities and breast cancer risk.** *Cancer Epidemiol Biomarkers Prev* 1998, **7:**1133-1144.
3. Boyd NF, Martin LJ, Stone J, Greenberg C, Minkin S, Yaffe MJ: **Mammographic densities as a marker of human breast cancer risk and their use in chemoprevention.** *Curr Oncol Rep* 2001, **3:**314-321.
4. Boyd NF, Dite GS, Stone J, Gunasekara A, English DR, McCredie MR, Giles GG, Tritchler D, Chiarelli A, Yaffe MJ, Hopper JL: **Heritability of mammographic density, a risk factor for breast cancer.** *N Engl J Med* 2002, **347:**886-894.
5. Boyd NF, Rommens JM, Vogt K, Lee V, Hopper JL, Yaffe MJ, Paterson AD: **Mammographic breast density as an intermediate phenotype for breast cancer.** *Lancet Oncol* 2005, **6:**798-808.
6. Rutter CM, Mandelson MT, Laya MB, Seger DJ, Taplin S: **Changes in breast density associated with initiation, discontinuation, and continuing use of hormone replacement therapy.** *JAMA* 2001, **285:**171-176.
7. Ursin G, Hovanessian-Larsen L, Parisky YR, Pike MC, Wu AH: **Greatly increased occurrence of breast cancers in areas of mammographically dense tissue.** *Breast Cancer Res* 2005, **7:**R605-R608.
8. Alowami S, Troup S, Al-Haddad S, Kirkpatrick I, Watson PH: **Mammographic density is related to stroma and stromal proteoglycan expression.** *Breast Cancer Res* 2003, **5:**R129-R135.
9. Gill JK, Maskarinec G, Pagano I, Kolonel LN: **The association of mammographic density with ductal carcinoma *in situ* of the breast: the Multiethnic Cohort.** *Breast Cancer Res* 2006, **8:**R30.
10. Habel LA, Dignam JJ, Land SR, Salane M, Capra AM, Julian TB: **Mammographic density and breast cancer after ductal carcinoma in situ.** *J Natl Cancer Inst* 2004, **96:**1467-1472.

11. Aiello EJ, Buist DS, White E, Porter PL: **Association between mammographic breast density and breast cancer tumor characteristics.** *Cancer Epidemiol Biomarkers Prev* 2005, **14**:662-668.

12. Hawes D, Downey S, Pearce CL, Bartow S, Wan P, Pike MC, Wu AH: **Dense breast stromal tissue shows greatly increased concentration of breast epithelium but no increase in its proliferative activity.** *Breast Cancer Res* 2006, **8**:R24.

13. Li T, Sun L, Miller N, Nicklee T, Woo J, Hulse-Smith L, Tsao MS, Khokha R, Martin L, Boyd N: **The association of measured breast tissue characteristics with mammographic density and other risk factors for breast cancer.** *Cancer Epidemiol Biomarkers Prev* 2005, **14**:343-349.

14. Guo YP, Martin LJ, Hanna W, Banerjee D, Miller N, Fishell E, Khokha R, Boyd NF: **Growth factors and stromal matrix proteins associated with mammographic densities.** *Cancer Epidemiol Biomarkers Prev* 2001, **10**:243-248.

15. Barcellos-Hoff MH, Aggeler J, Ram TG, Bissell MJ: **Functional differentiation and alveolar morphogenesis of primary mammary cultures on reconstituted basement membrane.** *Development* 1989, **105**:223-235.

16. Keely P, Fong A, Zutter M, Santoro S: **Alteration of collagen-dependent adhesion, motility, and morphogenesis by the expression of antisense α2 integrin mRNA in mammary cells.** *J Cell Sci* 1995, **108**:595-607.

17. Tlsty TD, Hein PW: **Know thy neighbor: stromal cells can contribute oncogenic signals.** *Curr Opin Genet Dev* 2001, **11(1)**:54-59.

18. Noel A, Foidart JM: **The role of stroma in breast carcinoma growth *in vivo* .** *J Mammary Gland Biol Neoplasia* 1998, **3**:215-225.

19. Elenbaas B, Spirio L, Koerner F, Fleming MD, Zimonjic DB, Donaher JL, Popescu NC, Hahn WC, Weinberg RA: **Human breast cancer cells generated by oncogenic transformation of primary mammary epithelial cells.** *Genes Dev* 2001, **15**:50-65.

20. Orimo A, Gupta PB, Sgroi DC, Arenzana-Seisdedos F, Delaunay T, Naeem R, Carey VJ, Richardson AL, Weinberg RA: **Stromal fibroblasts present in invasive human breast carcinomas promote tumor growth and angiogenesis through elevated SDF-1/CXCL12 secretion.** *Cell* 2005, **121**:335-348.

21. Shekhar MP, Pauley R, Heppner G, Werdell J, Santner SJ, Pauley RJ, Tait L: **Host microenvironment in breast cancer development: extracellular matrix-stromal cell contribution to neoplastic phenotype of epithelial cells in the breast.** *Breast Cancer Res* 2003, **5**:130-135.

22. Iyengar P, Espina V, Williams TW, Lin Y, Berry D, Jelicks LA, Lee H, Temple K, Graves R, Pollard J, *et al.*: **Adipocyte-derived collagen VI affects early mammary tumor progression *in vivo*, demonstrating a critical interaction in the tumor/stroma microenvironment.** *J Clin Invest* 2005, **115**:1163-1176.

23. White DE, Kurpios NA, Zuo D, Hassell JA, Blaess S, Mueller U, Muller WJ: **Targeted disruption of beta1-integrin in a transgenic mouse model of human breast cancer reveals an essential role in mammary tumor induction.** *Cancer Cell* 2004, **6**:159-170.

24. Paszek MJ, Zahir N, Johnson KR, Lakins JN, Rozenberg GI, Gefen A, Reinhart-King CA, Margulies SS, Dembo M, Boettiger D, *et al.*: **Tensional homeostasis and the malignant phenotype.** *Cancer Cell* 2005, **8**:241-254.

25. Wozniak MA, Desai R, Solski PA, Der CJ, Keely PJ: **ROCK-generated contractility regulates breast epithelial cell differentiation in response to the physical properties of a three-dimensional collagen matrix.** *J Cell Biol* 2003, **163**:583-595.

26. Liu X, Wu H, Byrne M, Jeffrey J, Krane S, Jaenisch R: **A targeted mutation at the known collagenase cleavage site in mouse type I collagen impairs tissue remodeling.** *J Cell Biol* 1995, **130**:227-237.

27. Provenzano PP, Eliceiri KW, Campbell JM, Inman DR, White JG, Keely PJ: **Collagen reorganization at the tumor-stromal interface facilitates local invasion.** *BMC Medicine* 2006, **4**:38.

28. Williams RM, Zipfel WR, Webb WW: **Interpreting second-harmonic generation images of collagen I fibrils.** *Biophys J* 2005, **88**:1377-1386.

29. Nazir MZ, Eliceiri KW, Ahmed A, Hathaway E, Hashmi A, Agarwal V, Rao Y, Kumar S, Lukas T, Riching KM, Rueden C, Wang Y, White JG: **WiscScan: a software defined laser-scanning microscope.** *Biomed Eng Online* 2006 in press.

30. Rueden C, Eliceiri KW, White JG: **VisBio: a computational tool for visualization of multidimensional biological image data.** *Traffic* 2004, **5**:411-417.

31. **ImageJ** [http://rsb.info.nih.gov/ij/]

32. Bird DK, Eliceiri KW, Fan CH, White JG: **Simultaneous two-photon spectral and lifetime fluorescence microscopy.** *Appl Opt* 2004, **43**:5173-5182.

33. Provenzano PP, Rueden CT, Trier SM, Yan L, Ponik SM, Inman DR, Keely PJ, Eliceiri KW: **Nonlinear optical imaging and spectral-lifetime computational analysis of endogenous and exogenous fluorophores in breast cancer.** *J Biomed Opt* in press.

34. Lin EY, Jones JG, Li P, Zhu L, Whitney KD, Muller WJ, Pollard JW: **Progression to malignancy in the polyoma middle T onco-protein mouse breast cancer model provides a reliable model for human diseases.** *Am J Pathol* 2003, **163**:2113-2126.

35. Wang W, Wyckoff JB, Frohlich VC, Oleynikov Y, Huttelmaier S, Zavadil J, Cermak L, Bottinger EP, Singer RH, White JG, *et al.*: **Single cell behavior in metastatic primary mammary tumors correlated with gene expression patterns revealed by molecular profiling.** *Cancer Res* 2002, **62**:6278-6288.

36. Zipfel WR, Williams RM, Christie R, Nikitin AY, Hyman BT, Webb WW: **Live tissue intrinsic emission microscopy using multi-photon-excited native fluorescence and second harmonic generation.** *Proc Natl Acad Sci USA* 2003, **100**:7075-7080.

37. Zoumi A, Yeh A, Tromberg BJ: **Imaging cells and extracellular matrix *in vivo* by using second-harmonic generation and two-photon excited fluorescence.** *Proc Natl Acad Sci USA* 2002, **99**:11014-11019.

38. Brown E, McKee T, diTomaso E, Pluen A, Seed B, Boucher Y, Jain RK: **Dynamic imaging of collagen and its modulation in tumors *in vivo* using second-harmonic generation.** *Nat Med* 2003, **9**:796-800.

39. Yan L, Rueden CT, White JG, Eliceiri KW: **Applications of combined spectral lifetime microscopy for biology.** *Biotechniques* 2006, **41**:249. 251, 253

40. Huang S, Heikal AA, Webb WW: **Two-photon fluorescence spectroscopy and microscopy of NAD(P)H and flavoprotein.** *Biophys J* 2002, **82**:2811-2825.

41. Pradhan A, Pal P, Durocher G, Villeneuve L, Balassy A, Babai F, Gaboury L, Blanchard L: **Steady state and time-resolved fluorescence properties of metastatic and non-metastatic malignant cells from different species.** *J Photochem Photobiol B* 1995, **31**:101-112.

42. Bavik C, Coleman I, Dean JP, Knudsen B, Plymate S, Nelson PS: **The gene expression program of prostate fibroblast senescence modulates neoplastic epithelial cell proliferation through paracrine mechanisms.** *Cancer Res* 2006, **66**:794-802.

43. Allinen M, Beroukhim R, Cai L, Brennan C, Lahti-Domenici J, Huang H, Porter D, Hu M, Chin L, Richardson A, *et al.*: **Molecular characterization of the tumor microenvironment in breast cancer.** *Cancer Cell* 2004, **6**:17-32.

44. Chung LW, Baseman A, Assikis V, Zhau HE: **Molecular insights into prostate cancer progression: the missing link of tumor microenvironment.** *J Urol* 2005, **173**:10-20.

45. De Wever O, Mareel M: **Role of tissue stroma in cancer cell invasion.** *J Pathol* 2003, **200**:429-447.

46. Condeelis J, Singer RH, Segall JE: **The great escape: when cancer cells hijack the genes for chemotaxis and motility.** *Annu Rev Cell Dev Biol* 2005, **21**:695-718.

47. Parr C, Watkins G, Mansel RE, Jiang WG: **The hepatocyte growth factor regulatory factors in human breast cancer.** *Clin Cancer Res* 2004, **10**:202-211.

48. Sachdev D, Yee D: **The IGF system and breast cancer.** *Endocr Relat Cancer* 2001, **8**:197-209.

49. Surmacz E: **Function of the IGF-I receptor in breast cancer.** *J Mammary Gland Biol Neoplasia* 2000, **5**:95-105.

50. Byrne C, Colditz GA, Willett WC, Speizer FE, Pollak M, Hankinson SE: **Plasma insulin-like growth factor (IGF) I, IGF-binding protein 3, and mammographic density.** *Cancer Res* 2000, **60**:3744-3748.

51. Boyd NF, Stone J, Martin LJ, Jong R, Fishell E, Yaffe M, Hammond G, Minkin S: **The association of breast mitogens with mammographic densities.** *Br J Cancer* 2002, **87**:876-882.

52. Benlimame N, He Q, Jie S, Xiao D, Xu YJ, Loignon M, Schlaepfer DD, Alaoui-Jamali MA: **FAK signaling is critical for ErbB-2/ErbB-3 receptor cooperation for oncogenic transformation and invasion.** *J Cell Biol* 2005, **171**:505-516.

53. Aplin AE, Juliano RL: **Integrin and cytoskeletal regulation of growth factor signaling to the MAP kinase pathway.** *J Cell Sci* 1999, **112**:695-706.

54. Baron V, Calleja V, Ferrari P, Alengrin F, Van Obberghen E: **p125Fak focal adhesion kinase is a substrate for the insulin and insulin-like growth factor-I tyrosine kinase receptors.** *J Biol Chem* 1998, **273**:7162-7168.

55. Ishizawar R, Parsons SJ: **c-Src and cooperating partners in human cancer.** *Cancer Cell* 2004, **6**:209-214.

56. Hauck CR, Sieg DJ, Hsia DA, Loftus JC, Gaarde WA, Monia BP, Schlaepfer DD: **Inhibition of focal adhesion kinase expression or activity disrupts epidermal growth factor-stimulated signaling promoting the migration of invasive human carcinoma cells.** *Cancer Res* 2001, **61**:7079-7090.

57. Sieg DJ, Hauck CR, Ilic D, Klingbeil CK, Schaefer E, Damsky CH, Schlaepfer DD: **FAK integrates growth-factor and integrin signals to promote cell migration.** *Nat Cell Biol* 2000, **2**:249-256.

58. Warburg O: *The Metabolism of Tumors* London: Arnold Constable; 1930.

59. Skala MC, Riching KM, Gendron-Fitzpatrick A, Eickhoff J, Eliceiri KW, White JG, Ramanujam N: *In vivo* **multiphoton microscopy of NADH and FAD redox states, fluorescence lifetimes, and cellular morphology in precancerous epithelia.** *Proc Natl Acad Sci USA* 2007, **104**:19494-19499.

60. Garriga-Canut M, Schoenike B, Qazi R, Bergendahl K, Daley TJ, Pfender RM, Morrison JF, Ockuly J, Stafstrom C, Sutula T, *et al.*: **2-Deoxy-D-glucose reduces epilepsy progression by NRSF-CtBP-dependent metabolic regulation of chromatin structure.** *Nat Neurosci* 2006, **9**:1382-1387.

61. Gatenby RA, Gawlinski ET, Gmitro AF, Kaylor B, Gillies RJ: **Acid-mediated tumor invasion: a multidisciplinary study.** *Cancer Res* 2006, **66**:5216-5223.

62. Lakowicz JR: *Principles of Fluorescence Spectroscopy* 3rd edition. New York: Springer; 2006.

63. Maeda-Yorita K, Aki K: **Effect of nicotinamide adenine dinucleotide on the oxidation-reduction potentials of lipoamide dehydrogenase from pig heart.** *J Biochem* 1984, **96**:683-690.

Pre-publication history

The pre-publication history for this paper can be accessed here:

http://www.biomedcentral.com/1741-7015/6/11/prepub

Nonlinear optical imaging and spectral-lifetime computational analysis of endogenous and exogenous fluorophores in breast cancer

Paolo P. Provenzano
University of Wisconsin
Departments of Pharmacology and Biomedical Engineering
    and
Laboratory for Optical and Computational Instrumentation
    and
Paul P. Carbone Comprehensive Cancer Center
Madison, Wisconsin 53706

Curtis T. Rueden
University of Wisconsin
Laboratory for Optical and Computational Instrumentation
Madison, Wisconsin 53706

Steve M. Trier
University of Wisconsin
Department of Biomedical Engineering
    and
Laboratory for Optical and Computational Instrumentation
    and
Paul P. Carbone Comprehensive Cancer Center
Madison, Wisconsin 53706

Long Yan
University of Wisconsin
Department of Biomedical Engineering
    and
Laboratory for Optical and Computational Instrumentation
Madison, Wisconsin 53706

Suzanne M. Ponik
University of Wisconsin
Departments of Pharmacology and Biomedical Engineering
    and
Laboratory for Optical and Computational Instrumentation
    and
Paul P. Carbone Comprehensive Cancer Center
Madison, Wisconsin 53706

David R. Inman
University of Wisconsin
Department of Pharmacology
    and
Paul P. Carbone Comprehensive Cancer Center
Madison, Wisconsin 53706

Patricia J. Keely
University of Wisconsin
Departments of Pharmacology and Biomedical Engineering
    and
Laboratory for Optical and Computational Instrumentation
    and
Paul P. Carbone Comprehensive Cancer Center
Madison, Wisconsin 53706

Kevin W. Eliceiri
University of Wisconsin
Department of Biomedical Engineering
    and
Laboratory for Optical and Computational Instrumentation
Madison, Wisconsin 53706

Abstract. Multiphoton laser scanning microscopy (MPLSM) utilizing techniques such as multiphoton excitation (MPE), second harmonic generation (SHG), and multiphoton fluorescence lifetime imaging and spectral lifetime imaging (FLIM and SLIM, respectively) are greatly expanding the degree of information obtainable with optical imaging in biomedical research. The application of these nonlinear optical approaches to the study of breast cancer holds particular promise. These noninvasive, multidimensional techniques are well suited to image exogenous fluorophores that allow relevant questions regarding protein localization and signaling to be addressed both *in vivo* and *in vitro*. Furthermore, MPLSM imaging of endogenous signals from collagen and fluorophores such as nicotinamide adenine dinucleotide (NADH) or flavin adenine dinucleotide (FAD), address important questions regarding the tumor-stromal interaction and the physiologic state of the cell. We demonstrate the utility of multimodal MPE/SHG/FLIM for imaging both exogenous and/or endogenous fluorophores in mammary tumors or relevant 3-D systems. Using SLIM, we present a method for imaging and differentiating signals from multiple fluorophores that can have overlapping spectra via SLIM Plotter—a computational tool for visualizing and analyzing large spectral-lifetime data sets. © *2008 Society of Photo-Optical Instrumentation Engineers.* [DOI: 10.1117/1.2940365]

1 Introduction

Breast cancer is a devastating disease accounting for ~15% of all female cancer-related deaths in the United States and is

Address all correspondence to Kevin Eliceiri, Laboratory for Optical and Computational Instrumentation, University of Wisconsin at Madison, 271 Animal Sciences, 1675 Observatory Drive, Madison, WI 53706; Tel: 608–263–6288; Fax 608–262–4570; E-mail: eliceiri@wisc.edu

the most prevalent cancer among women.[1] Therefore, technologies to detect, classify, study, and combat breast cancer are of great significance. Among these technologies, optical imaging modalities have helped facilitate advances in cancer diagnosis as well as aid in studies aimed at understanding the mechanisms associated with cancer formation and progression (reviewed in Refs. [2] and [3]). Often, relevant questions regarding complex cell signaling events and physiological processes can only be well understood by imaging temporal molecular localization events and other subcellular processes in cells in their engineered or native environment. As such, nonlinear optical imaging techniques based on multiphoton excitation have emerged as powerful tools to noninvasively image cellular processes both *in vitro* and *in vivo*.[4–11]

Multiphoton laser scanning microscopy (MPLSM), first reported by Denk and colleagues,[8] is an optical sectioning technique that allows thick biological sections to be imaged via absorption of two or more low-energy photons (typically 700 to 1050 nm). For this reason, the effective imaging depth can greatly exceed conventional confocal microscopy,[8,12] while reducing photo damage and maintaining superior viability following prolonged exposure.[13] As a result of these characteristics, the use of multiphoton imaging technology is increasing, which has facilitated the emergence of two-photon second harmonic generation (SHG) imaging of biological structures,[5–7,10,14] multiphoton fluorescence lifetime imaging microscopy (FLIM; Refs. [15–18]), and multiphoton spectral lifetime imaging microscopy (SLIM; Refs. [19] and [20]). Hence, when utilized individually, and particularly in combination, these advances provide tools to obtain detailed multidimensional data from cells containing exogenous and/or endogenous fluorophores.

Engineering of proteins tagged with exogenous fluorophores, such as Green Fluorescent Protein (GFP) and DsRed (and their variants), has greatly expanded our knowledge of fundamental intracellular processes affording unparalleled insight into protein localization, interactions, and temporal dynamics (reviewed in Refs. [21–23]). In particular, recent advances using exogenous fluorophores to generate (fluorescence resonance energy transfer (FRET)) are providing new information about complex signaling events within cancerous cells.[24,25] However, imaging complex systems and multiple fluorophores presents certain obstacles. One such difficulty arises from overlapping spectra and background signals from endogenous fluorophores. Yet endogenous fluorophores can also provide useful structural information about the interaction of a cell with its microenvironment[14,26–28] and the condition of the cell.[29–32] For instance: (1) endogenous SHG signals from collagen have provided fundamental information regarding the tumor cell's interaction with the stroma during invasion and metastasis,[14,26] (2) the metabolic state of carcinoma cells, as detected by endogenous fluorophores that are metabolic intermediates, has been correlated to metastatic potential,[32] and (3) diagnosis of human cancer by examining endogenous fluorophores has been an active area of research for many years (see Refs. [32–35] and references therein). Therefore, imaging endogenous fluorophores in breast cancer tissue can provide biologically meaningful information, and the ability to account for endogenous fluorescence when imaging exogenous or combined exogenous/endogenous fluorophores is very practical.

In breast tissue, the most dominant endogenous fluorophores imaged with MPLSM are tryptophan, nicotinamide adenine dinucleotide (NADH) and flavin adenine dinucleotide (FAD), as well as endogenous SHG signals from collagen. Each of these fluorophores has a unique excitation/emission spectra in the UV and visible light regimes that allows imaging of cellular morphology and organelles (such as mitochondria), as well as providing information about the metabolic state of the cell. The excitation/emission maxima of these fluorophores are $\sim 280/340$ nm for tryptophan, $\sim 340/450$ nm for NADH, and $\sim 450/530$ nm for FAD[30,31]; two-photon SHG from collagen is a nonfluorescent event resulting from the laser field suffering a nonlinear, second-order polarization when passing through a noncentrosymmetric ordered structure, and as such, SHG signals are at exactly half the excitation wavelength.[5,36–38] Although the spectra of these strong endogenous signals are reasonably distinct, there is overlap and they are not distinct from the exogenous fluorophores most commonly utilized with MPLSM. Therefore, in order to distinguish emission signals or correct for background contamination, filtering techniques may be employed to isolate portions of the emission spectra. However, this requires an *a priori* knowledge of the fluorophores that may not always be practical. Another approach is to utilize multiphoton FLIM, where the excited state lifetimes of the fluorophores are analyzed to potentially identify fluorophores with significantly overlapping spectra. However, the excited state lifetime of a molecule is microenvironment dependent, with factors such as pH, oxygen concentration, temperature, binding to macromolecules, and FRET states all potentially modifying the lifetime of a particular fluorophore.[39] Therefore, it is desirable to obtain spectral information combined with fluorescence lifetime data to facilitate imaging of multiple fluorophores within a cell or tissue. To achieve this goal, our research group has developed a combined multiphoton spectral and lifetime microscope[19,40] for SLIM that simultaneously collects fluorescence lifetime data from 16 separate 10-nm-width spectral channels. Using this system, we are able to collect data from spectrally overlapping fluorophores and isolate signals of interest from contaminating signals. In this paper, we will present data demonstrating the utility of MPLSM-based technologies to image endogenous signals and the combination of exogenous and endogenous signals with particular emphasis on spectral lifetime imaging, and the computational tools we have developed to visualize and analyze complex spectral lifetime data sets.

2 Methods

2.1 Cell Culture

T47D cells were obtained from the American Type Culture Collection. NMuMG cells were a kind gift from Dr. Caroline Alexander (University of Wisconsin). EGFP-Vinculin was a kind gift from Dr. Anna Huttenlocher (University of Wisconsin). For GFP-RBD, the Rho binding domain (RBD) of Rhotetkin was excised from GFP-RBD (a generous gift of Dr. Bill Bement, University of Wisconsin), subcloned into pEGFP-C1 (Clontech), and stably expressed in T47D breast carcinoma cells. T47D human breast cells were maintained in RPMI

supplemented with 10% fetal bovine serum and insulin. NMuMG mouse mammary cells were maintained in DMEM supplemented with insulin and 10% fetal bovine serum. Both cells lines were cultured at 37°C with 5% CO_2.

Cells were cultured and imaged under standard 2-D conditions or within 3-D collagen matrices. For 3-D culture, cells were cultured within a 1.0 to 4.0 mg/mL type-I collagen gel (rat-tail collagen solution, BD Biosciences) neutralized with 100 mM HEPES in 2× PBS. Following gel polymerization, gels were soaked in cell-specific media (described earlier) or serum-free media containing BSA and maintained at 37°C with 10% CO_2 until imaged as described in the text.

2.2 Mammary Tumors

All animal experiments were approved by the institutional animal use and care committee and meet NIH guidelines for animal welfare. To generate mammary tumors, polyoma middle-T mice[41] were employed. For MPLSM imaging of live, unfixed, intact (not sectioned), nonstained PyVT tumors, tumors were harvested and live tissue maintained in buffered media at 37°C. All tissues were imaged immediately following tissue harvest.

2.3 Instrumentation

For all imaging, two different custom multiphoton systems that are part of the University of Wisconsin Laboratory for Optical and Computational Instrumentation (LOCI, www.loci.wisc.edu) were utilized.[19,40,42] The first system is an MPLSM workstation constructed around a Nikon Eclipse TE300 that facilitates multiphoton excitation (MPE), SHG, and FLIM. All SHG imaging was performed on this microscope and was detected from the backscattered SHG signal.[38] A 5-W mode-locked Ti:Sapphire laser (Spectra-Physics-Millennium/Tsunami) excitation (laser field) source producing around 100-fs pulse widths was tuned to 780 to 900 nm. The beam was focused onto the sample with a Nikon CFI Plan Fluor 20× multi-immersion objective (NA of 0.75 and WD of 0.33 with water), a Nikon CFI Plan Fluor 40× oil immersion lens (NA=1.3), or a Nikon CFI Plan Apo 60× water-immersion lens (NA=1.2). Endogenous fluorescence and SHG signals were isolated with 464-nm (cut-on) long-pass and 445-nm narrow bandpass filters, while GFP signals were isolated with a 480 to 550 nm (bandpass) filter (all filters: TFI Technologies, Greenfield, Massachusetts). Intensity and FLIM data were collected by a H7422 GaAsP photon counting photomultiplier tube (PMT) (Hamamatsu) connected to a time-correlated single photon counting (TCSPC) system (SPC-730, Becker & Hickl).

The second microscope has been recently described in detail[19,29,40] and allows generation of multiphoton excitation intensity images in conjunction with FLIM and SLIM. In short, the system is built around an inverted microscope (TE 2000, Nikon, Melville, New York) with source illumination from a Ti:Sapphire mode-locking laser (Coherent Mira, Coherent, Santa Clara, California), with a tuning range of ~700 to 1000 nm. FLIM images were acquired with an electronic system for recording fast light signals by time-correlated single photon counting (SPC-830, Becker & Hickl). The system has several detectors, including a 16-channel combined spectral lifetime detector (utilizes a Hamamatsu PML-16

PMT), detection range 350 to 720 nm, and an H7422P GaAsP photon counting PMT (Hamamatsu) for intensity and lifetime imaging. The same lenses and filters were used as on the first microscope system. Both FLIM and SLIM data were collected over 60 s, and the pixel frame size for the MPE/SHG images is 1024×1024, while the FLIM and SLIM images are 256×256.

Acquisition for both MPLSM systems was performed with WiscScan,[43] a LOCI-developed software acquisition package that can control both the MPLSM and the lifetime collection. Image analysis was performed with ImageJ[44] and VisBio[45] software. Fluorescent lifetime analysis was carried out with SPCImage (Becker & Hickl), which can fit fluorescent decay data to an exponential function [Eq. (1)], for one, two, or three terms, and sum individual photon counts for each pixel to construct a contrast image. The incomplete model approach in SPCImage was used to compensate for instances where the fluorescence decay is slow compared to the time window defined by the repetition rate of the laser system. SLIM analysis was performed with SPCImage (Becker & Hickl) and SLIM Plotter (described in detail in Sec. 3).

3 Results and Discussion

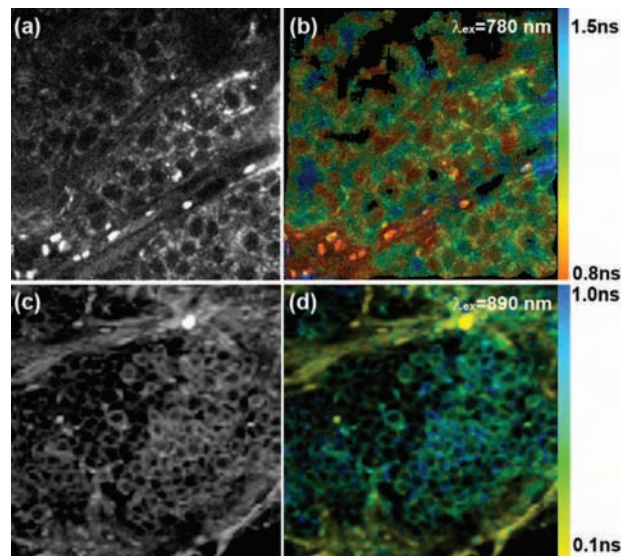### 3.1 Nonlinear Optical Imaging: MPE, SHG, FLIM, and SLIM

Increased understanding of tumor-stromal interactions is a critical aspect of the study of breast tumor formation and progression, since stromal-epithelial interactions play a critical role in both tumorigenesis and metastasis.[14,26,46–49] Since optical imaging modalities allow deep, noninvasive imaging of epithelial and stromal components of live breast tissue and tumors, they provide a valuable set of tools to better understand the tumor-stromal interaction. As seen in Fig. 1, multimodal multiphoton excitation (MPE)/SHG imaging offers a clear view of intact live mammary tumor tissue. Not only can epithelial and stromal cells be clearly seen, but their interaction with the stromal collagen matrix can also be readily imaged. By taking advantage of the fact that SHG signals are exactly half of the excitation wavelength, while fluorophores under MPE excitation obey the fundamental physical relationship of energy loss after excitation (Stokes shift), the MPE and SHG signals can be separated by filtering the emission signal. In Fig. 1, live mammary tumor tissue was excited at 890 nm to produce endogenous fluorescence from tumor and tumor-associated cells and SHG from collagen. (In our hands, with our biological systems, this wavelength has provided the strongest SHG signal for collagen.) To separate the emission signals, a 464-nm (cut-on) long-pass filter was used to isolate the cellular fluorescence (MPE signal), while SHG was isolated with a 445-nm narrow bandpass filter. By performing this filtering scheme, the tumor cell's interaction with collagen can be studied. Consequently, the use of combined MPE/SHG has the ability to identify and differentiate features that are either not obtainable or not easily obtained with more traditional fluorescence microscopy techniques. For instance, using this approach, we previously defined three tumor-associated collagen signatures (TACS; Ref. 14) in mammary tumors by imaging stromal collagen density and organization within and around tumors of varying stages. These TACS are diagnostic, allowing identification of early neoplastic regions
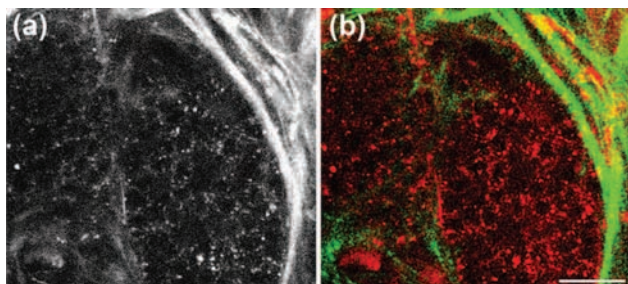
Fig. 1 MPE/SHG imaging of live tumor tissue. Combined (a) and separated (b) MPE/SHG images acquired following λ_{ex}=890 nm of live mammary tumor tissue. Combined MPE/SHG clearly demonstrates the ability to image deep into live tissue and obtain meaningful information from endogenous signals. In (b), emission signals were isolated with a 464-nm (cut-on) long-pass filter for MPE (pseudocolored red) and a 445-nm narrow bandpass filter SHG (pseudocolored green). This approach permits identification of epithelial tumor cells, tumor-associated stromal cells, and the collagen matrix. As such, combined MPE/SHG imaging of intact tumors can provide relevant information about the cell-matrix interaction and how matrix density and organization influence cell behavior. Bar = 25 μm.

Fig. 2 FLIM imaging of live mammary tumor tissue. Tumors were imaged at λ_{ex}=780 nm [(a) and (b)] and λ_{ex}=890 nm [(c) and (d)] to produce endogenous fluorescence from NADH and FAD, respectively. Intensity [(a) and (c)] and color-mapped lifetime [(b) and (d)] images are shown. Color mapping represents the weighted average of the mean lifetime (τ_m) (Eq. (2)) following fitting with a two-term exponential model [Eq. (1)]. Note that emission from collagen (d) maps to the yellow end of the spectrum, indicating SHG.

as well as signatures that identify invading metastatic cells.[14] TACS-1 characterizes the presence of increased SHG signal intensity due to increased locally dense collagen within the globally increased collagen concentration surrounding tumors, serving as a reliable hallmark for locating small neoplastic regions. TACS-2 classifies straightened collagen fibers stretched around the tumor, constraining the tumor volume and indicating that the tumor has substantially expanded and is straining the space of its microenvironment. TACS-3 is the identification and characterization of radially aligned (distributed at approximately 90 deg relative to the tumor boundary) collagen fibers that facilitate local invasion, and support evidence presented by Condeelis and colleagues that metastasizing tumor cells migrate along collagen fibers.[3,26]

Multiphoton FLIM provides an additional data dimension—allowing the measurement of the fluorescence lifetimes of endogenous fluorophores within normal and tumor cells while simultaneously identifying collagen in and

around the tumor by exploiting the fact that the collagen signal is not fluorescent and as such has a theoretical lifetime of zero. Figure 2 demonstrates the utility of multiphoton FLIM in identifying and measuring lifetimes of the relevant metabolic components NADH and FAD, as well as identifying collagen. To characterize and present lifetime information, the data was fit with a multiexponential model:

$$I_f(t) = \sum_{i=0}^{n} a_i \exp(-t/\tau_i) + c = a_1 \exp(-t/\tau_1) + a_2 \exp(-t/\tau_2)$$

$$+ a_3 \exp(-t/\tau_3) + \cdots . + c, \qquad (1)$$

where a is the fractional contribution of each of the compo-
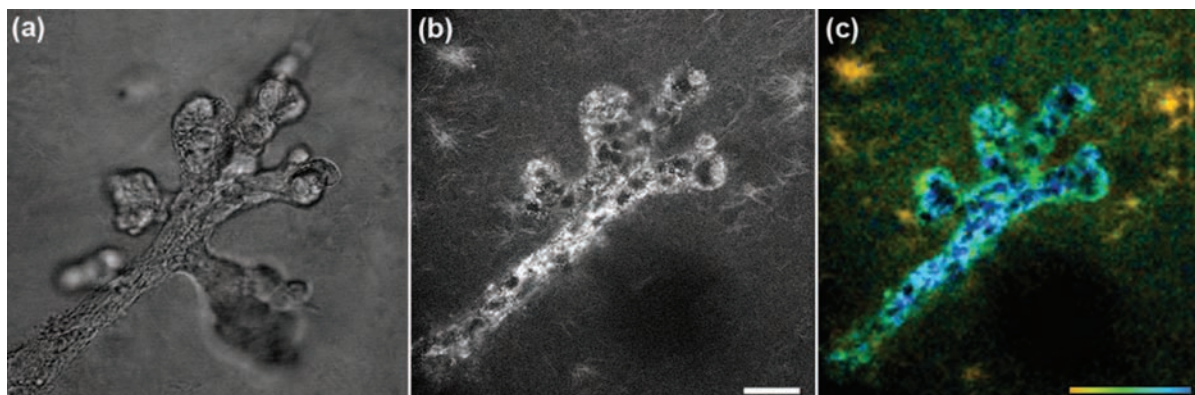
Fig. 3 Imaging mammary ductal structure in reconstituted 3-D matrices. Nontransformed NMuMG mammary cells were cultured within a 3-D collagen matrix (3.0 mg/mL) for 7 days to demonstrate the ability of combined MPE/SHG/FLIM to study cellular differentiation and the extracellular microenvironment. The recapitulated ductal structure can be seen with transmitted light (a), but use of combined MPE/SHG (b) and/or multiphoton FLIM (c) provides information regarding the collagen matrix and the physiologic state of the cells. In (c), color represents the weighted average following a two-term exponential fit as described in Fig. 2. Scale bar=25 μm; color bar 0.08 to 1.0 ns (red to blue).
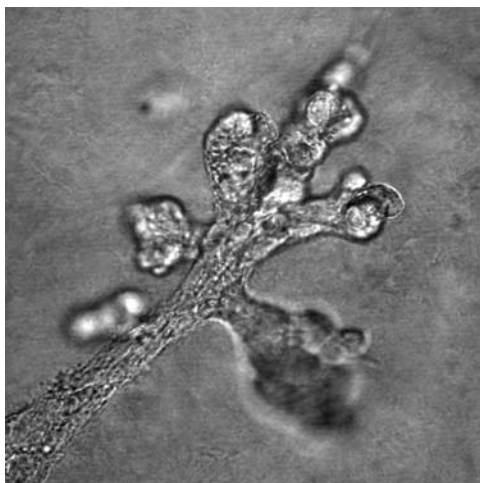
Video 1. Movie of a transmitted light *z*-stack (200 μm), showing mammary ductal structure with a reconstituted 3-D matrix (Quick-Time, 2.7 MB). [URL: http://dx.doi.org/10.1117/1.2940365.1].

Video 2. Pseudocolored movie of a combined MPE/SHG *z*-stack (200 μm), showing ductal structure and the surrounding collagen microenvironment (QuickTime, 4.49 MB). [URL: http://dx.doi.org/10.1117/1.2940365.2].

nents, τ is the fluorescence lifetime, and c is background light noise. By examining the relative contributions of the lifetime components as well as their value, it may be possible to identify a particular fluorophore or gain an understanding about biological processes that are influencing a fluorophore. In Fig. 2, the data are presented as a weighted average of a two-component lifetime fit:

$$\tau_m = (a_1\tau_1 + a_2\tau_2)/(a_1 + a_2). \qquad (2)$$

Hence, FLIM can help identify different fluorophores, with the caveat that absolute identification of the source fluorophore is not certain. However, with the addition of spectral information, much stronger conclusions regarding the emission source can be obtained (see the following).

In addition to the ability to image live tissues, studies in more reductionist *in vitro* systems that reconstruct aspects of the cell's microenvironment, such as reconstituted 3-D matrices, can provide valuable information regarding cell phenotype and signaling events. Figure 3 demonstrates the ability of mammary epithelial to recapitulate ductal structure when cultured under the appropriate conditions within a collagen matrix, supporting the concept of this system as a valuable method to study breast epithelia. Although transmitted light [Fig. 3(a); Video 1] provides information regarding the morphology of the cells and allows visualization of the ductal structure, little information can be obtained regarding the cellular interaction with the microenvironment. By exciting signals from endogenous sources, insight into this interaction can be gained. Combining MPE excitation of endogenous fluorophores with SHG imaging, a more complete view of the structure and its interactions can be obtained [Fig. 3(b); Video 2]. Furthermore, multiphoton FLIM can be utilized as described earlier to acquire lifetime data that can identify the metabolic state of the cell or isolate and characterize fluorophores present with and around the cells. This is of even greater utility when the desired goal is to image both exogenous and endogenous signals simultaneously, such as is the case for protein localization (Fig. 4) or FRET experiments within 3-D collagen environments. As seen in Fig. 4, combined MPE/
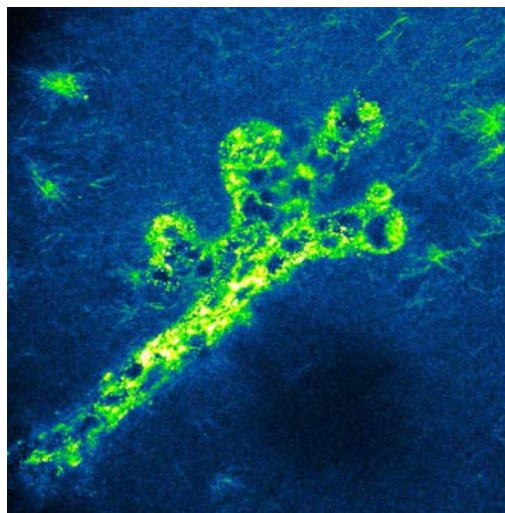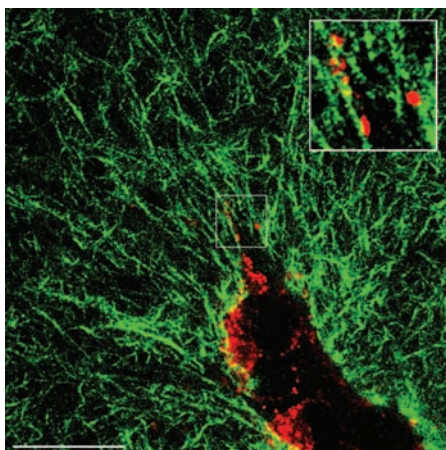
SHG imaging allows a clear view of the cell-matrix interaction in 3-D. GFP emissions from GFP-Vinculin were separated using a 480- to 550-nm (bandpass) filter, while SHG was isolated with a 445-nm narrow bandpass filter. Three-dimensional matrix adhesion to the collagen matrix can clearly be seen (see Fig. 4, inset) allowing a reconstruction of cell morphology, collagen organization, and the cell-matrix interface. However, in more complex studies, such as FLIM, the presence of a strong SHG signal (or other endogenous or exogenous signal) in close proximity to the fluorophore can be very problematic. Moreover, while FRET measured with FLIM can be superior to intensity-based FRET measurements due to the fact that FLIM is independent of fluorophore concentration, FLIM is susceptible to multiple signal contamination issues in data analysis, particularly when more than two lifetime components are potentially present. This can be overcome by employing spectral lifetime imaging, as discussed earlier. By separating the spectral signal of interest from contaminating background[28] or other fluorophores of interest, the lifetime of the fluorophore of interest, can be cleanly obtained (Fig. 5). However, in order to efficiently analyze the large multidimensional data sets from SLIM, a computational infrastructure needs to be developed. As a means to effectively visualize and exploit the information from spectral lifetime data, we have developed a novel computational package.

3.2 Combined Spectral Lifetime Visualization: SLIM Plotter

Slim Plotter is a lightweight application for the visualization of combined spectral lifetime data (Fig. 6). The main purpose of the program is to allow exploration of regions of data collected with an SLIM system, but the software also provides some features to assist hardware engineers in proper calibration of the acquisition hardware.

The program is written in Java, which enables cross-platform deployment. Launchers are provided for Microsoft Windows (EXE file), Mac OS X (application bundle), and

Fig. 4 Imaging 3-D matrix adhesions with MPE/SHG. Combined MPE/SHG imaging at λ_{ex}=890 nm of GFP-Vinculin expressing NMuMG cells within a 3-D collagen matrix (4.0 mg/mL) for 7 days allows a clear view of collagen matrix organization, vinculin localization, and the cell-matrix interaction. Emissions signals from GFP were isolated with a 480 to 550-nm (bandpass) filter (pseudocolored red) and a 445-nm narrow bandpass filter SHG (pseudocolored green). Three-dimensional matrix adhesion to the collagen matrix can clearly be seen (inset). Bar=25 μm.

*nix (shell script). It uses the VisAD Java visualization toolkit for displaying data (http://www.ssec.wisc.edu/~billh/visad.html), which in turn uses Java3D (https://java3d.dev.java.net/). Slim Plotter requires Java version 1.4 and Java3D 1.3—these versions come bundled with Mac OS X, so Slim Plotter should work out of the box on Apple computers, while Windows and Linux users must set up the Java runtime environment and Java3D if they do not already have them installed. Although memory requirements vary depending on the size of the data set, at least 512 MB of system RAM is strongly recommended. See the Slim Plotter website (http://www.loci.wisc.edu/ome/slim.html) for download and detailed installation instructions.

3.2.1 Features

Slim Plotter is designed to be a simple yet effective tool. The main interface fits into one window, with two displays—a 2-D intensity view and a 3-D surface view—plus visualization options and a log window to report numerical results and errors.

3.2.2 Reading data

Slim Plotter uses the LOCI Bio-Formats I/O library (http://www.loci.wisc.edu/ome/formats.html) to read the proprietary
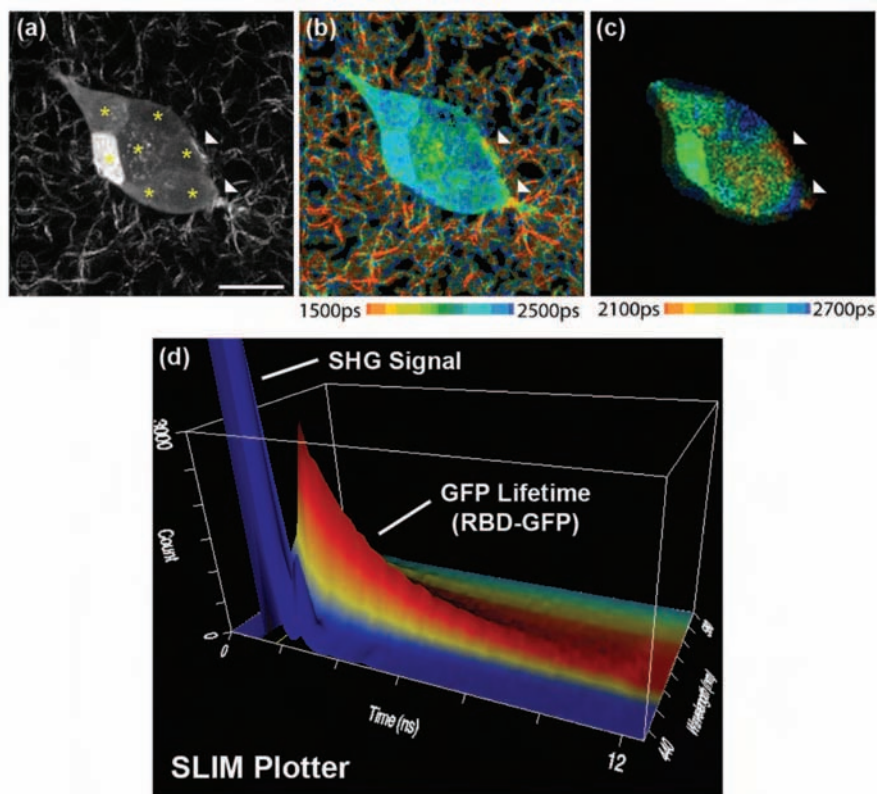
Fig. 5 SLIM to optimize exogenous and endogenous signals. (a) MPE/SHG intensity image of seven T47D breast cells (each designated by a star), composing a developing ductal tubule within a 3-D collagen matrix (1.3 mg/mL) after 5 days in culture. Each cell expresses various levels of EGFP–Rhotekin binding domain (GFP-RBD) and therefore has different intensity in the MPE image. (b) An FLIM image demonstrates collagen fibers in juxtaposition to localized GFP-RBD. Arrows demonstrate regions of localized RBD, suggesting local Rho GTPase activation. Note that Rho is activated at "stress" points where the forming tubule contacts collagen fibers, which is biologically quite interesting but can make data analysis and interpretation difficult. Therefore, the spectral channels for GFP [see the SLIM Plotter output in (d)] were selectively reimaged, producing a new SLIM image, and were color mapped with a narrower lifetime scale (c). This allows elimination of the collagen signal when desired and shows additional localization of GFP-RBD. Hence, spectral lifetime imaging has the ability to facilitate separation of signals of interest for analysis or elimination when the large data set can be efficiently managed and visualized (see Sec. 3.2). Bar=20 μm.
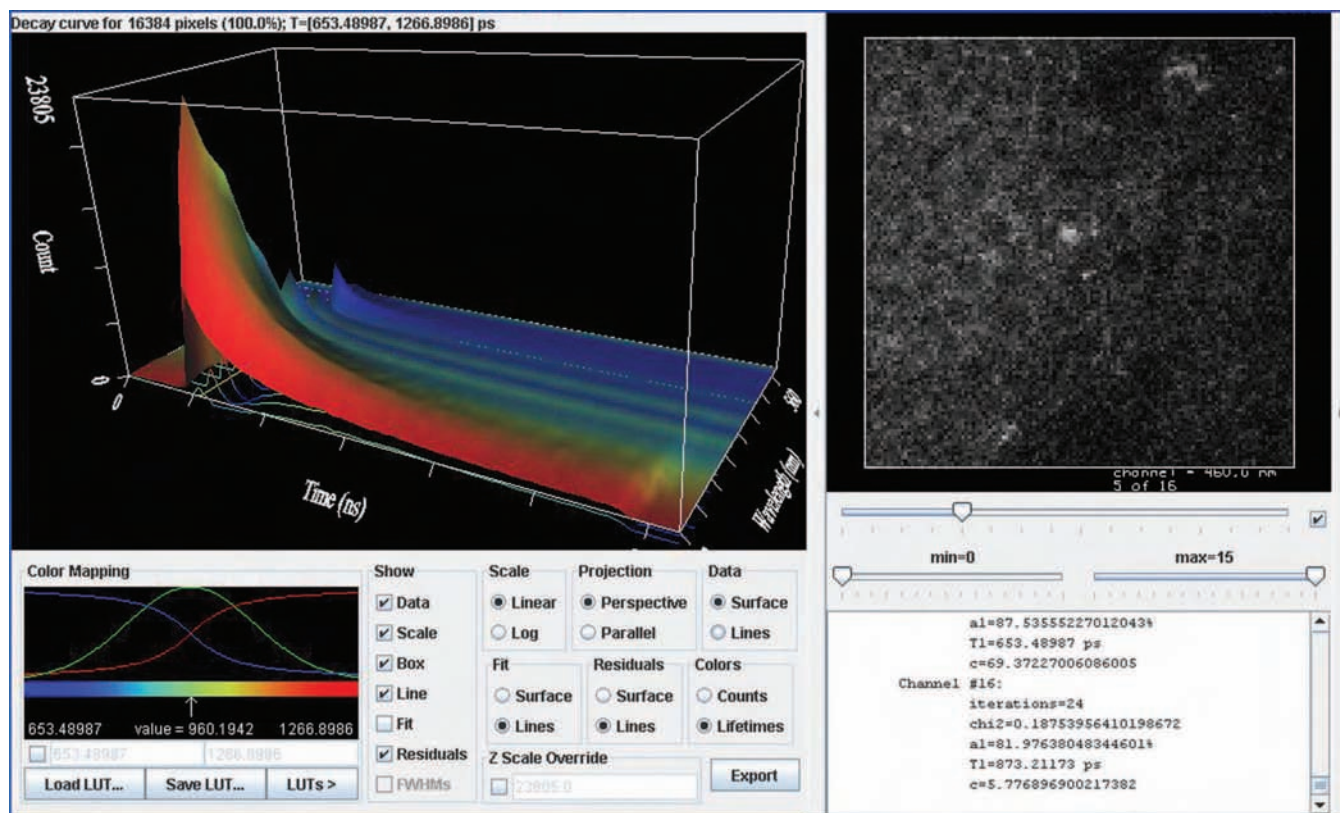
Fig. 6 SLIM Plotter Visualization window. Example of the SLIM Plotter Visualization window. Data used for this example is from a mammary tumor, and the image shown in the 2-D viewer is a single spectral channel.

SDT data files that the Becker & Hickl FLIM acquisition boards utilize. It supports data of any feasible image resolution, with any number of lifetime bins and spectral channels, including single-channel lifetime data. It automatically extracts the data set's dimensionality (image width, image height, lifetime bin granularity, and number of spectral channels) from the SDT file, but allows the user to override these values if they were stored incorrectly within the file. Some values, particularly the physical width of the lifetime histogram in nanoseconds and the physical width of the spectral range in nanometers, are not present in the SDT format, so the software provides an interface for the user to specify these values (time range, starting wavelength, and channel width). Reasonable defaults are provided—our time range is fixed at 12.5 ns, and channel width is typically 10 nm. Since the starting wavelength can vary, however, Slim Plotter looks at the file name—if the user opted to include the starting wavelength as part of the file name (e.g., 783-890-PML16-440nm-240sec-c.sdt is 440 nm), it uses the indicated value; otherwise, it defaults to 400 nm unless the user overrides the value.

3.2.3 *Visualization*

One challenge of combined spectral lifetime data is that the sheer dimensionality of the data makes it impossible to show the entire raw data set at once in a comprehensible fashion. Slim Plotter addresses this difficulty with a two-pronged approach: a 2-D image view showing an overview of the data, with the ability to target a specific region of interest (ROI), and a 3-D plot focusing on the targeted region's details (Fig. 6).

The 2-D image view on the right shows an intensity image for each spectral channel (see Fig. 6). Such intensity images are not directly recorded in the SDT files, but Slim Plotter computes them by summing each lifetime histogram to produce a corresponding aggregate intensity value for each pixel. The slider directly beneath the image controls which channel is currently visible in the display, and Slim Plotter begins with the brightest channel selected. The user can control the 2-D view's brightness and contrast using "min" and "max" sliders beneath the channel selector, which control the image's black level and white level, respectively.

The left plot shows a sum of lifetime decay curves (histograms) for each channel (see Fig. 6). The data is rendered as a surface in 3-D, with the *x* and *z* axes corresponding to the histogram's excitation time and photon count, respectively, and the *y* axis varying across wavelength. The program behaves similarly for single-channel lifetime data, but uses a 2-D line plot for the lifetime histogram, rather than a 3-D surface. The limitation of this view is that it shows only one decay curve per channel, with no facility for differentiating between spatial locations (pixels) within the image. To mitigate this issue, the user can select a ROI by dragging the mouse in the 2-D image view, the pixels are summed and the 3-D surface view displays the totals. In this fashion, the investigator can study lifetime and spectral properties within a

specific structure of the sample. The 3-D view initially displays a sum of all pixels. The user can narrow the focus by encircling a region, or even clicking on an individual pixel. The text directly above the 3-D display indicates the number and percentage of pixels currently being summed.

Initially, the height of the surface is scaled to fit the screen. As such, it can sometimes be difficult to study weaker channels when one channel dominates in intensity. Slim Plotter allows toggling of individual channels using the check box next to the slider beneath the right plot. The program smoothes over any deactivated channels in the surface. It is also possible to fix the *z*-scale range to an absolute value by checking the Z Scale Override check box and changing the value of the adjacent text field. Furthermore, the *z* axis can be configured to use a log scale rather than the default linear one by clicking the Log radio button in the Scale options.

To ease discrimination between differing intensity values, the 3-D surface is colored according to a lookup table (LUT). The default table ranges from blue at low levels through the color spectrum to red at high levels, but the table can be customized to provide an alternative color scheme. The LUTs button allows selection of a number of preset color tables, including hue, black-to-red, black-to-green, black-to-blue, black-to-magenta, black-to-cyan, black-to-yellow, grayscale (black-to-white), fire/heat, and ice/cold. The user can also opt to adjust the red, green, and blue color component lines manually by drawing with the mouse. Additionally, the current color table can be saved for later retrieval to a file in a simple binary format compatible with the popular ImageJ program (http://rsb.info.nih.gov/ij/). Last, by default, the color table is automatically scaled such that the smallest value in the surface corresponds to the leftmost color in the table, and the largest value matches the rightmost color. However, at times, it is useful to associate particular colors with absolute values; Slim Plotter enables this behavior with the check box inside the color controls and the two text fields corresponding to the minimum and maximum absolute counts.

There are a few additional visualization options, mostly regarding the 3-D surface view. First, instead of a surface, the data can be rendered as a series of line graphs, one per channel, by clicking the Lines radio button in the Data options. Second, instead of the usual perspective display projection, the program can also show a parallel projection mode, which results in structures along each axis neatly aligned for comparison. Third, the visibility of various components within the display can be toggled, including the bounding box, the scale bars, and the data itself, by using the check boxes in the Show options. Last, the layout of the displays can be rearranged using the left and right arrow buttons surrounding the 2-D view section: clicking the left arrow moves the 2-D view to the left side of the window, while clicking the right arrow causes the 2-D view to break away into its own separate window.

3.2.4 Lifetime curve fitting

In practice, it is expected that the lifetime histograms will conform to an exponential decay pattern in the form [i.e., Eq. (1)]:

$$y(t) = \sum_{i=1}^{n} a_i \exp(-t/\tau_i) + c, \qquad (3)$$

where n represents the number of lifetime components, typically between 1 and 3; a is the scaling factor for each component; c is a background correction factor or offset; and τ corresponds to the expected excited state lifetime per component for the region under analysis.

At present, Slim Plotter can fit single-exponential curves to the lifetime data, to determine an approximation of the aggregate lifetime value per channel. It uses the Levenberg-Marquardt least-squares curve fitting algorithm (LMA) with the help of Janne Holopainen's L-M fit package (http://users.utu.fi/jaolho/). To use the curve fitting feature, the Align Peaks option must be checked when the data is first read (see Sec. 3.2.5). The program log located below the 2-D view shows the exact parameter values of each channel's fitted curve as they are computed, and the text above the left plot details the minimum and maximum aggregate lifetime values across all channels.

The curves are shown superimposed as lines over the data surface in 3-D, making it easy to verify their accuracy. The program also allows visualization of the residuals (differences between expected and actual data values) as lines. Similar to the data itself, the visibility of both the fitted curves and the residuals can be toggled individually using their respective check boxes in the Show options. In addition, the fitted data or the residuals can be shown as surfaces rather than lines, using the corresponding Surface radio buttons.

The default colorization of the 3-D surface data corresponds to surface height; however, if Slim Plotter performs curve fitting, the user can click the Lifetime radio button in the Colors options to colorize the surface instead, based on each channel's aggregate lifetime (τ) value, producing a striped result illustrating lifetime differences between channels. The rules described earlier for colorizing the surface based on height apply equally when visualizing color according to lifetime values.

One last option that is occasionally useful to improve the quality of the curve fit result is the Cut 1.5 ns From Fit check box on the initial confirmation screen, enabled by default. This option disregards the last 1.5 ns of histogram data when performing curve fitting, to compensate for the fact that our system sometimes records a sudden drop in photon counts at the tail end of the lifetime histogram—and the tail values are less important to obtain an accurate fit regardless.

3.2.5 Calibration

Ideally, everything would line up perfectly during collection of spectral lifetime data, with an instant system response time, or at least an equivalent system response delay at each channel. In practice, however, system response skew across channels is one of several practical complications that is associated with a functional spectral lifetime acquisition system. Slim Plotter utilizes an algorithm to correct for slight discrepancies in the system response time between channels: at each channel, the software looks for the histogram's highest value—which should correspond to the peak of the lifetime decay curve—and "pushes forward" individual channels until they all line up. In other words, the program pads these channels

with zeroes so that the channels' decay curve peaks coincide with one another. The program log outputs the results of this alignment when the main window first appears. Unchecking the Align Peaks check box on the initial confirmation screen disables this behavior, but Slim Plotter will not perform exponential curve fitting unless it is allowed to align the peaks.

When calibrating a spectral lifetime system, it is useful for the hardware engineer to perform an acquisition with a second harmonic source (as opposed to a fluorescence sample), which has essentially zero lifetime. Any measured lifetime would therefore be the system response. This response function can be used to deconvolve the fluorescence decay curves so as to correct for the effects of the finite instrument response. Slim Plotter is also capable of analyzing these system response files by computing and visualizing the full width at half maximum (FWHM) values for each channel's lifetime histogram. Since this option is mainly useful for analyzing system response, it is off by default, but it can be enabled by checking the Compute FWHMs check box on the initial confirmation screen. If enabled, Slim Plotter shows the FWHMs as green lines in the 3-D surface view, and their visibility can be toggled using the FWHMs checkbox in the Show options.

3.2.6 Data export

The lifetime histograms currently being viewed can be exported for further processing in another program, using the Export button in the 3-D view controls. Slim Plotter writes the data to a text file in a simple comma-separated values (CSV) format, which can be easily imported into any numeric spreadsheet application.

3.2.7 Slim Plotter future directions

There are a number of improvements we are planning to Slim Plotter to provide more effective analysis of combined spectral lifetime data sets:

- **Integrated VisBio environment**. As part of a larger development effort across our Java software, we are creating a standardized infrastructure of modular components for data I/O, metadata handling, visualization, and analysis. We plan to integrate SLIM Plotter further into this infrastructure, allowing it to utilize these modularized components and to be called as a modular application itself from other applications.
- **Multiexponential curve fitting**. Slim Plotter currently fits only single-exponential lifetime curves. We would like to extend this functionality to support two- and three-component fits, since there are often multiple major lifetime components within the sample, and being able to differentiate between them is critical.
- **Channel binning and SDT export**. SPCImage complements Slim Plotter nicely for lifetime analysis, but SPCImage does not include much support for multispectral data. As such, it would be valuable for Slim Plotter to be able to produce output SDT files with multiple channels binned into one, for use with SPCImage's more sophisticated curve fitting routine.
- **Improved file format**. The SDT format has a number of shortcomings—e.g., the inability to embed time range, starting wavelength, and channel width into the file as metadata—and is somewhat proprietary in nature. We are developing an open format for storing spectral lifetime data based on Heirarchical data format (HDF) and using the OME-XML data

model,[50] which both our acquisition system itself and Slim Plotter will support via Bio-Formats.

- **Configurability**. Slim Plotter would benefit from greater configurability. For example, certain parameters such as whether to align the lifetime decay curve peaks must be set when Slim Plotter first starts, and the alignment cannot be toggled or configured afterward. Similarly, the lifetime curve fitting routine itself could benefit from a greater number of options, such as SPCImage's ability to "lock down" certain parameters or adjust the optional 1.5-ns cutoff.
- **Lifetime calibration**. The hardware engineer can collect a system response file that represents the instrument's behavior when no excitation is taking place. Slim Plotter should use this file to adjust the lifetime histograms—by subtracting out the response values—to improve the quality of the fits it generates.
- **Spectral calibration**. Similar to how the system response time differs between spectral channels, creating bias, there is an expected intensity distribution across channels that is not always confluent with reality. Slim Plotter should also calibrate for such system bias to improve spectra-related measurements.
- **Emission spectrum**. The emission spectrum consists of all lifetime bins and pixels summed for each channel, plotted in 2-D as a line graph; Slim Plotter should provide an option for this view.
- **Alternate visualization modes**. Slim Plotter would benefit from additional methods of visualizing the data. For example, a "spectral projection" view could consist of linearly mapping each channel into a position along the visible spectrum (similar to hue), colorizing accordingly, and then performing a maximum intensity projection while preserving the colorization. Slim Plotter could also include the ability to colorize the 2-D view according to each pixel's lifetime by computing the lifetime around that pixel to a particular radius; such a computation is expensive but can be very informative.

In conclusion, we find that combined spectral lifetime imaging has great utility for mitigating the traditional complications presented by endogenous fluorescence and allowing the scientist to fully exploit the power of fluorescence microscopy to record and characterize introduced and native fluorophores *in vivo*. This power of SLIM is demonstrated quite effectively in breast cancer, where many of the key players in cancer invasion and progression are intrinsically fluorescent, and tagged fluorescent constructs for many important signaling molecules have been developed. Rather than having to image the endogenous and exogenous fluorescence separately, as often is done, SLIM allows for simultaneous acquisition and effective discrimination. SLIM will be advanced greatly as photon counting techniques improve with the development of faster photon counting electronics, more sensitive multi-anode detectors, and improved analysis software for curve fitting.

References

1. American Cancer Society, "Cancer facts and figures/cancer statistics," at www.cancer.org(2005–2007).
2. V. Ntziachristos and B. Chance, "Probing physiology and molecular function using optical imaging: applications to breast cancer," *Breast Cancer Res. Treat.* **3**(1), 41–46 (2001).
3. M. Sidani, J. Wyckoff, C. Xue, J. E. Segall, and J. Condeelis, "Probing the microenvironment of mammary tumors using multiphoton microscopy," *J. Mammary Gland Biol. Neoplasia* **11**(2), 151–163 (2006).
4. W. R. Zipfel, R. M. Williams, R. Christie, A. Y. Nikitin, B. T. Hyman, and W. W. Webb, "Live tissue intrinsic emission microscopy using multiphoton-excited native fluorescence and second harmonic generation," *Proc. Natl. Acad. Sci. U.S.A.* **100**(12), 7075–7080 (2003).
5. G. Cox, E. Kable, A. Jones, I. Fraser, F. Manconi, and M. D. Gorrell, "Three-dimensional imaging of collagen using second harmonic generation," *J. Struct. Biol.* **141**(1), 53–62 (2003).
6. A. Zoumi, A. Yeh, and B. J. Tromberg, "Imaging cells and extracellular matrix *in vivo* by using second-harmonic generation and two-photon excited fluorescence," *Proc. Natl. Acad. Sci. U.S.A.* **99**(17), 11014–11019 (2002).
7. E. Brown, T. McKee, E. DiTomaso, A. Pluen, B. Seed, Y. Boucher, and R. K. Jain, "Dynamic imaging of collagen and its modulation in tumors *in vivo* using second-harmonic generation," *Nat. Med.* **9**(6), 796–800 (2003).
8. W. Denk, J. H. Strickler, and W. W. Webb, "Two-photon laser scanning fluorescence microscopy," *Science* **248**(4951), 73–76 (1990).
9. W. Wang, S. Goswami, E. Sahai, J. B. Wyckoff, J. E. Segall, and J. S. Condeelis, "Tumor cells caught in the act of invading: their strategy for enhanced cell motility," *Trends Cell Biol.* **15**(3), 138–145 (2005).
10. P. J. Campagnola, A. C. Millard, M. Terasaki, P. E. Hoppe, C. J. Malone, and W. A. Mohler, "Three-dimensional high-resolution second-harmonic generation imaging of endogenous structural proteins in biological tissues," *Biophys. J.* **82**(1, Pt. 1), 493–508 (2002).
11. E. B. Brown, R. B. Campbell, Y. Tsuzuki, L. Xu, P. Carmeliet, D. Fukumura, and R. K. Jain, "*In vivo* measurement of gene expression, angiogenesis and physiological function in tumors using multiphoton laser scanning microscopy," *Nat. Med.* **7**(7), 864–868 (2001).
12. V. E. Centonze and J. G. White, "Multiphoton excitation provides optical sections from deeper within scattering specimens than confocal imaging," *Biophys. J.* **75**(4), 2015–2024 (1998).
13. J. M. Squirrell, D. L. Wokosin, J. G. White, and B. D. Bavister, "Long-term two-photon fluorescence imaging of mammalian embryos without compromising viability," *Nat. Biotechnol.* **17**(8), 763–767 (1999).
14. P. P. Provenzano, K. W. Eliceiri, J. M. Campbell, D. R. Inman, J. G. White, and P. J. Keely, "Collagen reorganization at the tumor-stromal interface facilitates local invasion," *BMC Med.* **4**(1), 38 (2006).
15. S. Ameer-Beg, P. R. Barber, R. J. Hodgkiss, R. J. Locke, R. G. Newman, G. M. Tozer, B. Vojnovic, and J. Wilson, "Application of multiphoton steady state and lifetime imaging to mapping of tumor vascular architecture *in vivo*," *Proc. SPIE* **4620**, 85–95 (2002).
16. K. W. Eliceiri, C. H. Fan, G. E. Lyons, and J. G. White, "Analysis of histology specimens using lifetime multiphoton microscopy," *J. Biomed. Opt.* **8**(3), 376–380 (2003).
17. E. Gratton, S. Breusegem, J. Sutin, Q. Ruan, and N. Barry, "Fluorescence lifetime imaging for the two-photon microscope: time-domain and frequency-domain methods," *J. Biomed. Opt.* **8**(3), 381–390 (2003).
18. T. French, P. T. So, D. J. Weaver, Jr., T. Coelho-Sampaio, E. Gratton, E. W. Voss Jr., and J. Carrero, "Two-photon fluorescence lifetime imaging microscopy of macrophage-mediated antigen processing," *J. Microsc.* **185**(Pt 3), 339–353 (1997).
19. D. K. Bird, K. W. Eliceiri, C. H. Fan, and J. G. White, "Simultaneous two-photon spectral and lifetime fluorescence microscopy," *Appl. Opt.* **43**(27), 5173–5182 (2004).
20. A. Ruck, C. Hulshoff, I. Kinzler, W. Becker, and R. Steiner, "SLIM: a new method for molecular imaging," *Microsc. Res. Tech.* **70**(5), 485–492 (2007).
21. J. Lippincott-Schwartz, E. Snapp, and A. Kenworthy, "Studying protein dynamics in living cells," *Nat. Rev. Mol. Cell Biol.* **2**(6), 444–456 (2001).
22. J. Lippincott-Schwartz and G. H. Patterson, "Development and use of fluorescent protein markers in living cells," *Science* **300**(5616), 87–91 (2003).
23. J. Zhang, R. E. Campbell, A. Y. Ting, and R. Y. Tsien, "Creating new fluorescent probes for cell biology," *Nat. Rev. Mol. Cell Biol.* **3**(12), 906–918 (2002).
24. M. Parsons, J. Monypenny, S. M. Ameer-Beg, T. H. Millard, L. M. Machesky, M. Peter, M. D. Keppler, R. Schiavo, R. Watson, J. Chernoff, D. Zicha, B. Vojnovic, and T. Ng, "Spatially distinct binding of Cdc42 to PAK1 and N-WASP in breast carcinoma cells," *Mol. Cell. Biol.* **25**(5), 1680–1695 (2005).
25. M. Peter, S. M. Ameer-Beg, M. K. Hughes, M. D. Keppler, S. Prag, M. Marsh, B. Vojnovic, and T. Ng, "Multiphoton-FLIM quantification of the EGFP-mRFP1 FRET pair for localization of membrane receptor-kinase interactions," *Biophys. J.* **88**(2), 1224–1237 (2005).
26. W. Wang, J. B. Wyckoff, V. C. Frohlich, Y. Oleynikov, S. Huttelmaier, J. Zavadil, L. Cermak, E. P. Bottinger, R. H. Singer, J. G. White, J. E. Segall, and J. S. Condeelis, "Single cell behavior in metastatic primary mammary tumors correlated with gene expression patterns revealed by molecular profiling," *Cancer Res.* **62**(21), 6278–6288 (2002).
27. W. Wang, S. Goswami, K. Lapidus, A. L. Wells, J. B. Wyckoff, E. Sahai, R. H. Singer, J. E. Segall, and J. S. Condeelis, "Identification and testing of a gene expression signature of invasive carcinoma cells within primary mammary tumors," *Cancer Res.* **64**(23), 8585–8594 (2004).
28. P. P. Provenzano, K. W. Eliceiri, L. Yan, A. Ada-Nguema, M. W. Conklin, D. R. Inman, and P. J. Keely, "Nonlinear optical imaging of cellular processes in breast cancer," *Microsc. Microanal.* (in press).
29. D. K. Bird, L. Yan, K. M. Vrotsos, K. W. Eliceiri, E. M. Vaughan, P. J. Keely, J. G. White, and N. Ramanujam, "Metabolic mapping of MCF10A human breast cells via multiphoton fluorescence lifetime imaging of the coenzyme NADH," *Cancer Res.* **65**(19), 8766–8773 (2005).
30. G. M. Palmer, P. J. Keely, T. M. Breslin, and N. Ramanujam, "Autofluorescence spectroscopy of normal and malignant human breast cell lines," *Photochem. Photobiol.* **78**(5), 462–469 (2003).
31. N. D. Kirkpatrick, C. Zou, M. A. Brewer, W. R. Brands, R. A. Drezek, and U. Utzinger, "Endogenous fluorescence spectroscopy of cell suspensions for chemopreventive drug monitoring," *Photochem. Photobiol.* **81**(1), 125–134 (2005).
32. A. Pradhan, P. Pal, G. Durocher, L. Villeneuve, A. Balassy, F. Babai, L. Gaboury, and L. Blanchard, "Steady state and time-resolved fluorescence properties of metastatic and non-metastatic malignant cells from different species," *Photochem. Photobiol.* **31**(3), 101–112 (1995).
33. R. R. Alfano, A. Pradhan, G. C. Tang, and S. J. Wahl, "Optical spectroscopic diagnosis of cancer and normal breast tissues," *J. Opt. Soc. Am. B* **6**, 1015–1023 (1989).
34. N. Ramanujam, "Fluorescence spectroscopy of neoplastic and non-neoplastic tissues," *Neoplasia* **2**(1–2), 89–117 (2000).
35. R. R. Alfano, B. B. Das, J. Cleary, R. Prudente, and E. J. Celmer, "Light sheds light on cancer—distinguishing malignant tumors from benign tissues and tumors," *Bull. N. Y. Acad. Med.* **67**(2), 143–150 (1991).
36. P. Stoller, B. M. Kim, A. M. Rubenchik, K. M. Reiser, and L. B. Da Silva, "Polarization-dependent optical second-harmonic imaging of a rat-tail tendon," *J. Biomed. Opt.* **7**(2), 205–214 (2002).
37. R. Gauderon, P. B. Lukins, and C. J. Sheppard, "Optimization of second-harmonic generation microscopy," *Micron* **32**(7), 691–700 (2001).
38. R. M. Williams, W. R. Zipfel, and W. W. Webb, "Interpreting second-harmonic generation images of collagen I fibrils," *Biophys. J.* **88**(2), 1377–1386 (2005).
39. J. R. Lakowicz, H. Szmacinski, K. Nowaczyk, K. W. Berndt, and M. Johnson, "Fluorescence lifetime imaging," *Anal. Biochem.* **202**(2), 316–330 (1992).

40. L. Yan, C. T. Rueden, J. G. White, and K. W. Eliceiri, "Applications of combined spectral lifetime microscopy for biology," *BioTechniques* **41**(3), 249, 251, 253 passim (2006).
41. E. Y. Lin, J. G. Jones, P. Li, L. Zhu, K. D. Whitney, W. J. Muller, and J. W. Pollard, "Progression to malignancy in the polyoma middle T oncoprotein mouse breast cancer model provides a reliable model for human diseases," *Am. J. Pathol.* **163**(5), 2113–2126 (2003).
42. D. L. Wokosin, J. M. Squirrell, K. E. Eliceiri, and J. G. White, "An optical workstation with concurrent, independent multiphoton imaging and experimental laser microbeam capabilities," *Rev. Sci. Instrum.* **74**(1), 193–201 (2003).
43. K. W. Eliceiri, personal communication (2006).
44. M. D. Abramoff, P. J. Magelhaes, and S. J. Ram, "Image processing with ImageJ," *Biophotonics Int.* **11**(7), 36–42 (2004).
45. C. Rueden, K. W. Eliceiri, and J. G. White, "VisBio: a computational tool for visualization of multidimensional biological image data," *Traffic (Oxford, U. K.)* **5**(6), 411–417 (2004).
46. L. Ronnov-Jessen, O. W. Petersen, V. E. Koteliansky, and M. J. Bissell, "The origin of the myofibroblasts in breast cancer. Recapitulation of tumor environment in culture unravels diversity and implicates converted fibroblasts and recruited smooth muscle cells," *J. Clin. Invest.* **95**(2), 859–873 (1995).
47. T. D. Tlsty and P. W. Hein, "Know thy neighbor: stromal cells can contribute oncogenic signals," *Curr. Opin. Genet. Dev.* **11**(1), 54–59 (2001).
48. B. Elenbaas, L. Spirio, F. Koerner, M. D. Fleming, D. B. Zimonjic, J. L. Donaher, N. C. Popescu, W. C. Hahn, and R. A. Weinberg, "Human breast cancer cells generated by oncogenic transformation of primary mammary epithelial cells," *Genes Dev.* **15**(1), 50–65 (2001).
49. N. Sato, N. Maehara, and M. Goggins, "Gene expression profiling of tumor-stromal interactions between pancreatic cancer cells and stromal fibroblasts," *Cancer Res.* **64**(19), 6950–6956 (2004).
50. I. G. Goldberg, C. Allan, J. M. Burel, D. Creager, A. Falconi, H. Hochheiser, J. Johnston, J. Mellen, P. K. Sorger, and J. R. Swedlow, "The open microscopy environment (OME) data model and XML file: open tools for informatics and quantitative analysis in biological imaging," *Genome Biol.* **6**(5), R47 (2005).